



HAL
open science

Polymer-Polymer interfaces: from a better control and understanding of molecular mechanisms to materials engineering

Guillaume Miquelard-Garnier

► **To cite this version:**

Guillaume Miquelard-Garnier. Polymer-Polymer interfaces: from a better control and understanding of molecular mechanisms to materials engineering . Matériaux. UPMC - Paris 6 Sorbonne Universités, 2017. tel-01599374

HAL Id: tel-01599374

<https://hal.science/tel-01599374>

Submitted on 2 Oct 2017

HAL is a multi-disciplinary open access archive for the deposit and dissemination of scientific research documents, whether they are published or not. The documents may come from teaching and research institutions in France or abroad, or from public or private research centers.

L'archive ouverte pluridisciplinaire **HAL**, est destinée au dépôt et à la diffusion de documents scientifiques de niveau recherche, publiés ou non, émanant des établissements d'enseignement et de recherche français ou étrangers, des laboratoires publics ou privés.

Université Paris VI

Spécialité Chimie

Mémoire d'Habilitation à Diriger des Recherches

présenté par

Guillaume Miquelard-Garnier

Maître de Conférences au Conservatoire National des Arts et Métiers
Laboratoire PIMM – UMR 8006 ENSAM – CNRS - CNAM
Équipe « Polymères et Composites »

Polymer-Polymer interfaces:

**from a better control and understanding of molecular mechanisms to
materials engineering**

soutenu le 27 septembre 2017

Composition du jury

Prof. C. Derail
Dr. F. Touchard
Prof. K. Dalnoki-Veress
Prof. J-F. Gérard
Prof. D. Hourdet
Prof. G. Régnier
Prof. Y. Grohens
Dr. I. Ilioupoulos

Président
Rapporteur
Rapporteur
Rapporteur
Examineur
Examineur
Examineur
Examineur

Table of content

Introduction		p. 3
	References	p. 8
Chapter 1		p. 9
	References	p. 33
Chapter 2		p. 37
	References	p. 53
Chapter 3		p. 56
	References	p. 76
Chapter 4		p. 79
	References	p. 96
Chapter 5		p. 100
	References	p. 109
Resume		p. 111

Introduction

In this manuscript, I will present part of the research work I have conducted or been involved in over the past 9 years (including my 2.5 years as a post-doctorate associate and my 6.5 years as Maître de Conférences). This experimental work addresses topics that may seem loosely related, from instabilities in a thermoplastic process (nanolayer coextrusion) to reinforced thermoplastic nanocomposites or surface chemistry and patterning in elastomers, but that all resolve around questions on polymer interfaces. Though a large part of this work has an “engineering” or “applied towards materials” focus, it also deals in some aspects with more fundamental questions about confined polymers or polymer interfaces.

Presentation and general context

I will start by briefly describing my career up to this point. My detailed Curriculum Vitae can be found at the end of the manuscript (p.111). To summarize, I have been trained in physical chemistry and have specialized in polymer science. I started my scientific career by studying very soft materials (hydrogels) before moving on to elastomers, and am now working mainly with thermoplastics. My main interests have always been to finely tune and characterize the macromolecular structure to achieve specific properties for the materials. In other words, I am interested in the structure-properties relationships of polymers in general.

I graduated from the ESPCI (Ecole Supérieure de Physique et de Chimie Industrielles de Paris) along with a MSc « Matière Condensée : Chimie et Organisation » from the University of Pierre and Marie Curie (Paris VI) in 2004.

I obtained a PhD in Polymer Science in 2007 for a work on the mechanical and rheological properties of hydrophobically modified hydrogels. This work was done under the supervision of Costantino Creton (DR CNRS) and Dominique Hourdet (Prof. UPMC) in the Simm lab (Soft Matter Sciences and Engineering Physico - Chemistry of Polymers and Dispersed Media). The idea was to design hydrogels with both chemical and physical crosslinks. This was achieved by modifying poly(acrylic acid) (PAA), introducing both dangling double bonds and dodecyl groups. Double bonds were then crosslinked using dithiols, while dodecyl groups self-assembled into hydrophobic micelles during gelation. We showed that the elastic modulus was governed by the chemical crosslinks while the loss modulus was dramatically influenced by the hydrophobic micelles.¹ We then studied the mechanical properties of these hydrogels, mainly in compression. These polyelectrolytes hydrogels displayed large hysteresis even without hydrophobic modifications, which was attributed to strain-induced clustering.² We finally characterized the dissipation mechanisms induced by the hydrophobic groups (hysteresis) and their influence on the fracture of the hydrogels.³

I then spent two years working in Prof. Alfred J. Crosby's group at the University of Massachusetts (Polymer Science and Engineering Department). My research topic was on mechanical instabilities in thin polymeric films and elastomeric surfaces, and potential biophysical applications of these phenomena.⁴ I will go back in more details to this topic of research later on in the manuscript, especially on how mechanics of the contact-line can allow pattern control.⁵

Finally, I worked for 6 months with Prof. Liliane Léger and Dr. Frédéric Restagno, in collaboration with Essilor, on the diffusion of photochromic molecules in gels for optical applications.

In September 2010, I joined le Cnam (Conservatoire National des Arts et Métiers) as a Maître de Conférences (French equivalent to Assistant Professor) in what could be labelled as the Materials Science department (“Chaire des Matériaux Industriels”).

Le Cnam is an historical (established in 1794) French institute initially dedicated to teaching for working adults, which has recently expanded also to more traditional teaching. Due to its specificities, the research activities have become scarce in many departments at the turn of the century. Moreover, in the French de-industrialization context, Polymer Science, Metallic Materials Science, Ceramic Science (which were initially separate departments) lost over the last two decades both students and professors and had to be merged together to keep on going.

As a consequence, when I arrived, the research in polymer science within the department was only pursued by one Maître de Conférences, Cyrille Sollogoub, recruited in 2007, and one Ingénieur de Recherches, Alain Guinault. Cyrille Sollogoub had a good theoretical knowledge of the processing tools and especially all the fluid mechanics and rheological questions related to them. Alain Guinault had an experimental expertise in many polymer processing technologies. They were helped by a technician, Anne Grandmontagne, recruited in 2009. The group also had one ATER (short term contract lecturer). The small group was working with limited means on the control of blend morphologies through polymer processing, especially for gas barrier applications.

Soon after his arrival, Cyrille Sollogoub, helped by Alain Guinault, initiated a new research activity also in relation with the control of blend morphologies, by setting up an innovative processing tool, multilayer coextrusion (or nanolayer coextrusion if this scale is reached), about which a large part of the work that will be described in the manuscript deals with. In 2010, this tool was in place but not totally mastered, especially in terms of control of the morphologies at the nanoscale.

At the same time, the French agency in charge of evaluating the research departments (AERES, now HCERES) stated in 2009 that the CNAM Materials Science had a subcritical size in the actual research context, and suggested to join forces with the newly created PIMM lab (Process and Engineering in Mechanics and Materials) located in the ENSAM (Ecole Nationale Supérieure des Arts et Métiers) engineering school. This lab, which has a strong focus on materials processing, had been recently created by merging three other labs.

We joined the PIMM in between 2011 and 2012, bringing some of our equipment, while other remained in le Cnam, since our teaching activities are still located there. In 2012, a new Maître de Conférences was recruited, with an expertise in polymer chemistry, Matthieu Gervais.

The small Cnam group was integrated in a bigger research team called “ArPe” (Architecture, Propriétés et Procédés des Polymères) in 2013, which was later on (2015) merged with the “Tempo” team (Vieillessement et Durabilité des Polymères) to create a bigger research group focused on Polymer Science in general and simply called “Polymères et Composites”. In 2016, the group is constituted of 15 Professors, 6 research staff (engineers and technicians), around 25 PhD students and 4 ATER and postdocs.

Before detailing my research activities, let me say a brief word on teaching, which at least in the French system is supposed to represent 50% of my workload. The amount of teaching has been fixed at 128 hours of lecture per year (or 192 hours of practical work or tutorials). I have been actually doing a combination of lectures,

practical work and tutorials, plus other activities (mentoring, juries...) for an average of 230 hours a year. I mainly teach Polymer Science, from basics to specific properties, with a focus on the relationships between the chemical structure and the macroscopic properties (which is also the global idea behind my research, see below). Roughly one third of my teaching is related to ongoing education, i.e. given to working adults (hence from 6 to 9 pm during the week, and on Saturdays) which was the core of le Cnam activities till 15 years ago. Another third is given to students in mechanical or material engineering (apprenticeship). The last part of my teaching load consists in short courses to industrials (e.g. Saint-Gobain, Renault, PSA, Arkema...).

Research activities

As it was said earlier, the multilayer coextrusion process has been the central point of many studies of the group over the past few years. Though the process will be discussed in more details in chapters 1 and 2, let us here summarize briefly some of the key points.

Multilayer coextrusion is an innovative continuous process for polymeric materials, which has been invented almost 40 years ago^{6, 7} but is still by many points (which will be discussed later on), at the early stage of development. Derived from “classical” coextrusion, it consists in forcing the polymer flows, by successive slicing and recombining, to create materials composed of thousands of alternating layers of different polymers. While maintaining the same final thickness of the resulting material than in classical coextrusion (typically films or sheets with thicknesses around 100 μm – 1 mm), it enables the development of new materials where both phases are confined under the form of continuous layers with nanometric thicknesses (hence nanolayer coextrusion can also be used as a name). Due to confinement effects and/or multiplication of the interfaces, these structures may lead to new materials properties. This process has shown high potential for industrial applications: it was patented first by Dow¹ and used to produce iridescent films⁸. Since it is quite simply derived from a classical industrial tool (coextrusion), it could easily be adopted by industrials. It has then been widely studied by the group of Eric Baer in Case Western Reserve University, where many properties have been discussed (see for example this review⁹), such as confined crystallization effects which result in films with improved gas barrier properties.¹⁰

However, it is still only studied and used by less than 10 academic labs over the world, and has not been widely expanded in the industry either. The main reason is probably that it needs to be used very properly and precisely, with dedicated tools and staff, to produce well controlled materials. Another reason is that both the ability to obtain continuous nanolayers through this process is still poorly understood (e.g. for some polymer couples, a minimal critical thickness, dependent of the couple studied, is observed, under which the layers break which will affect the properties of the material¹¹). Even for couples where these thicknesses can be achieved, there might not be any synergistic effect achieved from the confinement and/or the interfaces.¹² Due to this lack of global understanding and predictive ability, studies are still often conducted through a “trial and error” approach which is not the most efficient.

Putting this in perspective, two approaches can be traditionally considered when dealing with structure-properties relationship in polymeric materials or more specifically when one tries to gain control of the materials structure at the smallest scale possible (“nanostructured materials”¹³) to achieve specific properties.

Indeed, polymeric materials display many internal “architectural” levels with hierarchical scaling: monomeric unit ($\sim \text{\AA}$), persistence length or entanglements ($\sim \text{nm}$), macromolecule or radius of gyration ($\sim 10 \text{ nm}$), crystalline morphologies (from 10 nm to $100 \mu\text{m}$), domain sizes in polymers blends (also from 10 nm to $100 \mu\text{m}$) etc. The materials ultimate macroscopic properties will depend on what happens at all those levels.

The first route, the “bottom-up” approach, has probably been the most common in the polymer community, especially since the huge amount of studies dealing with self-assembly of block copolymers since the 80’s.¹⁴ The idea is to go to materials via specifically designed individual macromolecules (with for example, desired tacticity, specific functionalities or chain ends, low dispersity...) that will, due to their chemical structure, interact together to organize (self-assembly, supramolecular assembly...) at a larger scale.

The second route is the “top-down” approach, when the processing route is designed specifically to achieve a certain organization of the macromolecules at some scale, whether micro or nano. This traditional approach in nanolithography can be expanded to other subfields dealing with polymeric materials. The traditional approach with polymer processing is that the resulting structure (usually at the microscale) is induced by the process and its governing parameters (flows, shears, stresses). However, new processing routes are being developed (sometimes named “structuring” processing¹⁵), where a better control or tunability of these parameters allows a better control at smaller scales and higher versatility or tailoring of the multiscale structure.

These approaches were usually conducted by different communities (polymer chemists and physical chemists for the first one, materials scientists and engineers for the second one), but an actual tendency is the merging of these communities and of these approaches: chemists have to show that new macromolecules have an interest as “real” materials with applications, while engineers have to get a better understanding of the specific properties (and the chemical structures specificities) of the polymers to be able to design innovative materials.

It was in this context that I was recruited in le Cnam’s research group, later on joined by Matthieu Gervais: while logically, the initial work was conducted with a top down approach by colleagues with a fluid physics and engineering background, it seemed obvious that research related to this innovative process could benefit from knowledges in chemistry and physical chemistry of polymers. The small team now covers a wide range of knowledge in polymer science and competences at different scales. Part of our work in common consists in achieving a better understanding of the multilayer coextrusion process, both at a “fundamental” and more applied level. The research group strongly believes in the idea that multilayer coextrusion has a tremendous potential, not only to develop materials with enhanced properties but also to obtain model systems for studying more fundamental physical problems concerning polymers under confinement (such as T_g change in amorphous polymers, or confined crystallization).

More generally, my research interests lie in the study, understanding, and applications of polymer-polymer interfaces. These interfaces play a big role in the properties of blends, especially when the size of the phases becomes comparable to the size of the interphase (the small interfacial region where monomeric units intimately mix), such as with materials prepared via multilayer coextrusion. It also plays a big (and complex) role in fundamental physical phenomena such as adhesion or wetting. Controlling several aspects of polymer surfaces (surface chemistry, texturation, mechanical properties) to tune the interfacial properties has been my topic of research during my postdoc at University of Massachusetts, which I have been pursuing later on, in collaboration with Christophe Poulard, Frédéric Restagno, and Liliane Léger.

Outline of the manuscript

In the first chapter, I will recall some basic fundamental aspects about polymer-polymer interfaces, especially related to the concept of surface tension. As stated above, most of the work that will be discussed here could be labeled as polymer engineering. Nonetheless, an interest in macromolecular mechanisms has always been at the core of the research I conducted. Since some of these mechanisms only have an effect at the sub-micron or nanoscale, they are mostly neglected by the processing community whom usually deals with phenomena at larger scales. In consequence, parts of the first chapter may seem almost too “basic” for soft matter physicists, but it might be of interest for readers having more of a background in polymer science and engineering.

In chapter 1, I will mainly focus on two more specific cases where surface and interfacial tension play a role.

The first will be the case of thermoplastic polymer blends. After some fundamental principles of thermodynamics, I will specifically discuss the concept of interaction parameter. Then I will discuss the potential interests of phases’ miniaturization and the different ways of achieving it, before focusing on the multilayer coextrusion process itself.

The second case will be dedicated to adhesion and wetting of elastomeric surfaces. In particular I will discuss how the properties of the surface will impact the interfacial interactions, whether with a liquid or another (polymeric) surface.

The manuscript will then be divided in two parts.

The first one will focus on the multilayer (or nanolayer) coextrusion process and will be divided in two chapters. Chapter 2 will deal with fundamental questions concerning the process, especially how we can understand and predict the concept of critical thickness for a nanolayered film of a given polymer couple. This chapter is mainly based on the PhD work of Adrien Bironeau I co-supervised, and the MSc internship work of Yakun Zhu I supervised. Chapter 3 will present some more applied work using this tool, in the fields of nanocomposites and block copolymers. It will be based on some of the work I did during my first years as a Maître de Conférences, and on part of the PhD work of Xiguang Li. It will also deal with the post-doctorate work of Sébastien Roland and the ongoing PhD work of Sebastian Montana.

The second part will present some results on elastomeric interfaces: how can we use mechanical instabilities at the surface or at the interface, and how can we modify “softly” the surface chemistry to obtain smart or model surfaces (chapter 4)? This work will be based on my post-doctorate work and on the post-doctorate work of Mohamed Dirany under my supervision.

Chapter 5 will present briefly my research project for the next years, or at least what my main research topic would be assuming I have the (financial) opportunity to.¹⁶ The aim is to follow up on the concept of critical thickness in nanolayer coextrusion and to extend the bridge between nanoscale polymer processing and the physics of liquids or soft solids at the interfaces and under confinement.

Note that for clarity reasons and since chapters are relatively independent of each other, I chose to have a separate reference section for each chapter.

References

1. Miquelard-Garnier, G.; Demoures, S.; Creton, C.; Hourdet, D., Synthesis and rheological behavior of new hydrophobically modified hydrogels with tunable properties. *Macromolecules* **2006**, *39*, (23), 8128-8139.
2. Miquelard-Garnier, G.; Creton, C.; Hourdet, D., Strain induced clustering in polyelectrolyte hydrogels. *Soft Matter* **2008**, *4*, (5), 1011-1023.
3. Miquelard-Garnier, G.; Hourdet, D.; Creton, C., Large strain behaviour of nanostructured polyelectrolyte hydrogels. *Polymer* **2009**, *50*, (2), 481-490.
4. Miquelard-Garnier, G.; Zimmerlin, J. A.; Sikora, C. B.; Wadsworth, P.; Crosby, A., Polymer microlenses for quantifying cell sheet mechanics. *Soft Matter* **2010**, *6*, (2), 398-403.
5. Miquelard-Garnier, G.; Croll, A. B.; Davis, C. S.; Crosby, A. J., Contact-line mechanics for pattern control. *Soft Matter* **2010**, *6*, (22), 5789-5794.
6. Schrenk, W. J. Method for multilayer coextrusion. **1973**, US Patent.
7. Schrenk, W. J.; Bradley, N. L.; Alfrey, T.; Maack, H., Interfacial flow instability in multilayer coextrusion. *Polymer Engineering & Science* **1978**, *18*, (8), 620-623.
8. <http://www.ptonline.com/articles/microlayer-films-new-uses-for-hundreds-of-layers>
9. Ponting, M.; Hiltner, A.; Baer, E., Polymer nanostructures by forced assembly: Process, structure, and properties. *Macromolecular Symposia* **2010**, *294*, (1), 19-32.
10. Wang, H. P.; Keum, J. K.; Hiltner, A.; Baer, E.; Freeman, B.; Rozanski, A.; Galeski, A., Confined Crystallization of Polyethylene Oxide in Nanolayer Assemblies. *Science* **2009**, *323*, (5915), 757-760.
11. Lin, Y.; Hiltner, A.; Baer, E., A new method for achieving nanoscale reinforcement of biaxially oriented polypropylene film. *Polymer* **2010**, *51*, (18), 4218-4224.
12. Mackey, M.; Flandin, L.; Hiltner, A.; Baer, E., Confined crystallization of PVDF and a PVDF-TFE copolymer in nanolayered films. *Journal of Polymer Science Part B: Polymer Physics* **2011**, *49*, (24), 1750-1761.
13. Whitesides, G. M.; Kriebel, J. K.; Mayers, B. T., Self-Assembly and Nanostructured Materials. In *Nanoscale Assembly: Chemical Techniques*, Huck, W. T. S., Ed. Springer US: Boston, MA, **2005**; pp 217-239.
14. Hawker, C. J.; Russell, T. P., Block Copolymer Lithography: Merging "Bottom-Up" with "Top-Down" Processes. *MRS Bulletin* **2005**, *30*, (12), 952-966.
15. Wang, K.; Chen, F.; Li, Z.; Fu, Q., Control of the hierarchical structure of polymer articles via 'structuring' processing. *Progress in Polymer Science* **2016**, *39*, (5), 891-920.
16. We scientists have to be pragmatic: nowadays what we ultimately work on depends on what funding we do obtain. I will end by an optimistic note, stating that some fundings being already secure, exciting work with talented collaborators lies ahead. Other more punctual projects (mainly industrially oriented) will not be presented, to keep the manuscript relatively short.

Chapter 1

Polymer-polymer interfaces: some theoretical background.

Most of the materials, whether nature or human made, or even life as we know it, consist in intimately and hierarchically structured phases, and the interfaces between these different phases often play a tremendous role in the resulting macroscopic (for example, optical or mechanical) properties of the materials.^{1,2}

Indeed, not many human made materials have been relying on a “pure” component: one can think of the early ages with bronze or cement. Nowadays, developing or synthesizing “new” “pure” components or processing tools for such components appears complicated and too costly for many applications. A cheaper and simpler (in theory) solution consists in blending, mixing or combining in some way existing molecules, seeking to produce materials with “synergistic” (i.e. ideally with better properties than predicted through simple mixing rules) effects over the pure components. Here, the interfaces within the material will be of fundamental importance to achieve (or not) such feats. The smaller the phases, the bigger the role of the interfaces.¹

This role is due to differences between bulk and interfacial properties, which have been long known for many materials. The composition of liquids or the crystalline structure of solids may differ close to the surface. The material will “recover” its bulk properties over a typical distance depending on molecular parameters. In polymeric materials, such distances might be greater than for other types of materials, due to the large sizes of the macromolecules.

In systems composed of atoms or small molecules, the typical length scale is governed by the (enthalpic) interaction forces between these atoms or molecules. This length scale corresponds to the typical distance over which the perturbation induced by the interface extends. For polymers, another length scale appears in addition to the one described previously, due to the covalent bonds between atoms within a macromolecule or polymer chain: this length scale is then, basically, the macromolecule size (usually described as an end-to-end distance or radius of gyration and on the order of 10 nm). This size, linked to the connectivity of the chain, is controlled by entropy: thermodynamic equilibrium will determine the most favorable conformation of the polymer chain (maximum entropy or minimum free energy).¹

Polymer-polymer interfaces play a dominant role, among others, in various aspects of my research: for example, in processes such as coextrusion, or in materials properties, such as adhesion or toughness of polymer blends and composites.^{3,4}

In the following, I will start by briefly describing the relations between intermolecular forces and surface or interfacial tension for polymers. Then I will deal with the thermodynamics of polymer blends and will discuss specifically the experimental determination of the Flory-Huggins interaction parameter, before describing an innovative process which produces polymeric materials composed of thousands of nanolayered phases. Finally I will go back to surface tension and discuss its effect (along with other surfaces characteristics) on adhesion and wetting, more specifically for elastomeric surfaces.

1.1. Surface energy, surface tension, and interfacial tension

1.1.1. Surface energy, surface tension

Surface energy quantifies the disruption of intermolecular bonds that occur when a surface is created.⁵ The simplest molecular picture of the surface energy is stating that molecules at the surface lack half of their neighbors compared to those in the bulk. Cohesive interactions are in consequence missing for the molecules at the surface (see Figure 1, in the case of a liquid: in that case, surface tension is a more appropriate term).

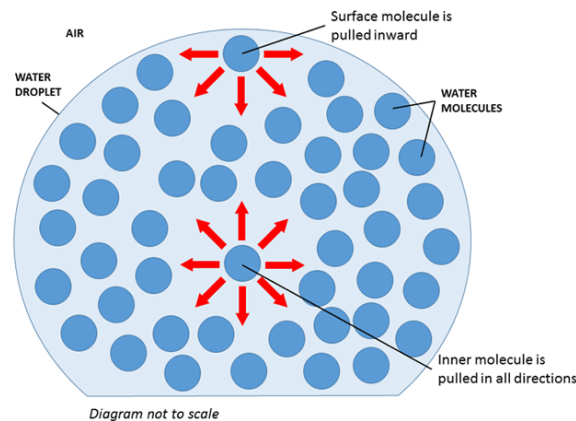


Figure 1: schematic of the simple molecular model to explain surface energy / surface tension.⁶

The surface energy may be defined as the excess energy at the surface of a material compared to the bulk, or the work required to build an area of a particular surface.

Surface tension and surface energy refer to the same dimensional quantity (though debates still exist concerning the accuracy of this statement⁷): the surface tension can be imagined as the force one has to apply to “cut” this surface by one unit length. Its dimensions are those of a force per unit length (N/m). It can also be viewed as the energy one has to bring to increase the surface area by one unit, with dimensions of energy per unit surface (J/m^2).

Even though the liquid state is disordered, it is still a condensed one: the attractive interactions between molecules are stronger than the thermal agitation $k_B T$ (where T is the temperature and k_B the Boltzmann constant). In consequence, the surfaces of fluids present some striking properties that resemble those of a solid: a very light object will float on the surface of pure water, fluids can adopt specific shapes despite the fact that they flow... This is due to surface tension: one can think of the liquid surface as a stretched, taut, membrane that opposes its deformation.^{1,8}

Cutting a body will disrupt its bonds, and therefore consumes energy. If the cutting is done reversibly, the energy consumed by the process will be equal to the surface energies of the two new surfaces created. The unit surface energy of a material would therefore be half of its energy of cohesion; in practice, dynamic processes such as passivation or adsorption will often reduce the surface energy compared to this “cleaved bond” model.

Some typical values for surface energy are listed in Table 1 below. Most polymers lie in the 20-40 mJ/m² range.

Material	Surface energy / tension (mJ/m ²) (20 °C) ^{1, 9, 10}
Glass	310
Gypsum	370
Copper	1650
Water	72.8
Ethanol	22.4
Mercury	487
Acetone	23.8
n-octane	21.6
Poly(ethylene terephthalate)	44.6
poly(methyl methacrylate)	41.1
polystyrene	39.4
polyethylene	36.8
poly(dimethyl siloxane)	20.4
polypropylene (atactic)	29.4

Table 1: typical values for surface energies of solids and surface tensions of liquids.

1.1.2. Intermolecular forces

Surface tension is due to the molecular state at surfaces and interfaces, but it is a macroscopic concept. Let us now determine surface tension from molecular interactions between two surfaces, specifically long-range (typically up to 100 nm) van der Waals forces.

Consider two identical planar surfaces (whether liquid or solid) separated by vacuum and at a distance h from each other (see Figure 2). The pairwise summation of energies between all the atoms of these surfaces leads, in the case of van der Waals forces (having the form $-C/r^6$, C being a constant expressed in J.m⁶ and r the distance between the two molecules), to equation 1:

$$F(h) = -\frac{A}{12\pi h^2} \quad (\text{Eq. 1})$$

with A the Hamaker constant defined by Hamaker¹¹ as $A = \pi^2 C \rho_1 \rho_2$ with ρ the number density of atoms (m⁻³) and subscripts 1 and 2 referring to the general case of two different bodies. A usually lies in the range of 10⁻¹⁹-10⁻²⁰ J. In this symmetric case A is positive which means surfaces will attract each other. In the general case of two surfaces of different nature separated by a third medium, it can be either positive or negative. When A is negative there is repulsion between the surfaces.

Let us now include the energy within one of the surface expressed as $F_1 = -\text{constant} + \frac{A}{12\pi h_i^2}$. The constant here is the bulk cohesive energy and the second term is the van der Waals attractive energy the molecules at the surface are subjected to from the bulk (meaning that in the case of a liquid, it will tend to minimize its surface area). h_i is the typical molecular length of the system (this molecular length plays a role in phenomena such as spinodal dewetting of thin films, see section 2.6.3.).

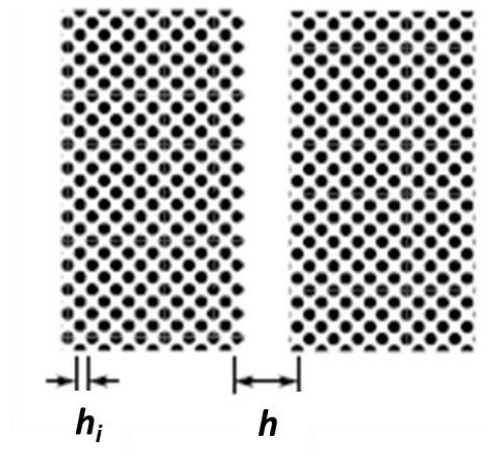


Figure 2: two identical surfaces with molecular length h_i at a distance h from each other (from ¹²).

If we consider only the surface terms and estimate the total energy, we then have for two planar surfaces at a distance h from each other: $F_{total}(h) = -\frac{A}{12\pi h_i^2} \left(1 - \frac{h_i^2}{h^2}\right)$. When the two surfaces are in contact ($h=h_i$), $F_{total} = 0$ (note that Equation 1 is valid for $h > h_i$). When the two surfaces are isolated ($h \rightarrow \infty$), the energy of the system is simply 2γ , γ being the surface tension of the considered surface.¹²

We can then express surface tension as a function of van der Waals interactions (Equation 2):

$$\gamma = \frac{A}{24\pi h_i^2} \tag{Eq. 2}$$

As we will see in section 2.6.4., the surface energy is also half the thermodynamic work of adhesion (i.e. half the energy needed to separate two flat surfaces from contact to infinity).

With $A \sim 10^{-19}$ J, a molecular size $\lesssim 1$ nm, one obtain $\gamma \sim 10$ mJ/m². In the case of hydrogen bonds, the cohesion energy is higher which explains why water has a strong surface energy for a liquid ($\gamma \approx 72$ mJ/m²).

1.1.3. Interfacial tension

An important notion in polymer science, and especially in the field of polymer blends that will be widely studied in the following of this manuscript, is the notion of interfacial tension, i.e. the surface energy between two immiscible liquids A and B . The interfacial tension is usually noted γ_{AB} . Because surface tensions of polymer melts all lie within the same range, the interfacial tension between immiscible polymers is usually quite small (few mJ/m²) and complicated to measure (see for example two reviews ^{13, 14}). This will be discussed in more details later on in the manuscript. Nonetheless, this is an important parameter in the field of polymer blends, because, along with the viscosities of the polymers and forces applied during the process chosen to prepare the blend, it will control its morphology, i.e. the size and shape of the dispersed phase within the matrix.¹⁵

Before giving some details about blend morphology in relation with polymer processing, I will briefly recall some fundamental aspects of thermodynamics of polymer blends and raise some questions about uncertainties in measurements of physical parameters used in the models.

1.2. Thermodynamics of polymer blends

(most of this section is based on a review article I recently wrote, which was published in European Polymer Journal and co-authored by Sébastien Roland¹⁶)

The free energy of mixing of a polymer blend of two polymers A and B involves an entropic term which favors the mixing, and an energetic term, which can either promote or oppose the mixing. In the Flory-Huggins theory framework (mean-field description based on a lattice model which neglects the chain connectivity and where each cell of the lattice is fully occupied by a monomeric unit of A or B, and with a mixing at constant volume), this energy of mixing can be expressed as a function of the pairwise (or segment-segment) interaction energies.
17-19

$$\overline{\Delta F_{mixing}} = \overline{\Delta U_{mixing}} - T \overline{\Delta S_{mixing}} = k_B T \left(\frac{\Phi}{N_A} \ln \Phi + \frac{1-\Phi}{N_B} \ln(1-\Phi) + \chi \Phi(1-\Phi) \right) \quad (\text{Eq. 3})$$

Where $\overline{\Delta F_{mixing}}$ is the free energy of mixing per lattice site, $\overline{\Delta U_{mixing}}$ and $\overline{\Delta S_{mixing}}$ are the energy of mixing and the entropy of mixing respectively.

In Equation 3, we have:

$$\overline{\Delta S_{mixing}} = -k_B \left(\frac{\Phi}{N_A} \ln \Phi + \frac{1-\Phi}{N_B} \ln(1-\Phi) \right) \quad (\text{Eq. 4})$$

With $\Phi_A = \Phi$ the volume fraction of the polymer A and $\Phi_B = 1 - \Phi$ the volume fraction of the polymer B, N_A and N_B the numbers of lattice sites occupied by molecules of A and B, respectively (i.e. roughly the number of Kuhn monomers within a polymer chain, the volume of an individual lattice being taken equal to the volume of one Kuhn monomer and supposing the volume of Kuhn monomers are equals for the two polymers). The entropic term, which always favors the mixing, is usually very small in the case of polymer blends, since N_A and N_B are large.

And

$$\overline{\Delta U_{mixing}} = k_B T \chi \Phi(1-\Phi) \quad (\text{Eq. 5})$$

χ being the Flory-Huggins interaction parameter, defined to characterize the difference of interaction energies in the blend.

χ can be expressed as a function of the three pairwise interactions energies between adjacent lattice sites in the system, i.e. u_{AA} , u_{BB} , and u_{AB} and the coordination number of the lattice, z :

$$\chi = \frac{z}{2} \frac{(2u_{AB} - u_{AA} - u_{BB})}{k_B T} \quad (\text{Eq. 6})$$

This parameter is dimensionless and is the difference between the interactions in the A-B blend and the ones in the pure components in $k_B T$ units.

In consequence, the free energy of mixing of two polymers is mainly governed by the energy of mixing (as stated earlier, because of the degree of polymerization of polymers, the entropic term in the free energy is usually very small).

As a first approximation, polymers are miscible with each other at given temperature and composition (i.e. the domain sizes of their mixture will be comparable to the dimension of the monomers) only when χ is negative.² Note that even for such blends (for example polystyrene/poly(vinyl methyl ether)), χ will only be negative for certain temperatures: below (lower critical solution temperature – LCST – systems) or above (upper critical solution temperature – UCST – systems) a certain temperature, or in a range of temperatures (systems displaying both LCST and UCST).

However, most polymers are immiscible with each other, and in these cases χ is positive. Jones and Randal² distinguish between immiscible polymers displaying very similar polymer pairs (for example polymers differing by isotopic substitution) and having χ on the order or below 10^{-4} and the vast majority of blends, when no close similarity or specific interactions between the polymers lead to χ values in the 10^{-3} - 10^{-1} range.

For a given blend, the Flory-Huggins parameter depends on the temperature, but also, though this is not apparent in the Flory-Huggins theory, on other parameters such as the volume fraction of the polymers, their degree of polymerization and even their dispersity, tacticity or pressure. To better take into account all these factors and capture experimental measurements which often display an important temperature-independent contribution, an empirical relation for the Flory interaction parameter is often used:

$$\chi(T) \cong A + B/T \quad (\text{Eq. 7})$$

with A the temperature-independent additive constant (often called, somewhat disturbingly, entropic) and B the temperature-dependent constant (often called enthalpic) and expressed in Kelvin (K).

In consequence two polymers can be miscible over a certain composition range, for certain molar masses (usually low molar masses), or under certain conditions of flows or pressure. These systems are usually called partially miscible. A more indistinct notion often used, especially in the field of polymer engineering, is the notion of “compatibility” for immiscible blends with a diffuse interphase due to some level of interactions between the phases (and, in consequence, potentially interesting performances as a material).²⁰

The interphase (the small – usually nanometric in thickness – region at the interface where polymers are actually blended to each other) in a blend of immiscible polymers (i.e. when $\chi > 0$) is linked to the Flory interaction parameter as showed by the theoretical work of Helfand and coworkers on unsymmetric polymer-polymer interfaces.²¹ A simple scaling argument omitting all prefactors is that the enthalpic cost for m monomers of A penetrating in the B melt is $m\chi k_B T$. This cost is on the order of the thermal energy $k_B T$ so $m \sim 1/\chi$. The size of the interphase w is then $w \sim bm^{1/2} \sim b/\chi^{1/2}$ with b the Kuhn length of the polymer, assuming a random coil conformation for the polymer chains.²² A more refined calculation of the segment density based on Gaussian random walk statistics by Helfand (see an illustration of the density profile in Figure 3) leads for the interphase of an A-B blend to:

$$w = 2 \left(\frac{1}{12\chi\sqrt{\rho_{0,A}\rho_{0,B}}} (\rho_{0,A}b_A^2 + \rho_{0,B}b_B^2) \right)^{1/2} \quad (\text{Eq. 8})$$

where ρ_0 is the density of the pure polymer (typically 10^{-2} times Avogadro's number monomer units/cm³) and b_A and b_B the Kuhn length of polymer A and B, respectively.

Assuming the density of the pure polymers are equals, this can be simplified in Equation 8bis:

$$w \approx 2 \left(\frac{1}{12\chi} (b_A^2 + b_B^2) \right)^{1/2} \quad (\text{Eq. 8bis})$$

And if the Kuhn monomers of the two species are similar, Equation 8bis can be simplified in Equation 8ter, which is usually chosen for the analyses (and which is fairly close to the equation obtained via scaling arguments). This simplified equation can be found in Helfand's first paper on the theory of the interface between immiscible polymers.²³

$$w \approx \frac{2b}{\sqrt{6\chi}} \quad (\text{Eq. 8ter})$$

For a given Kuhn monomer length, the lower the Flory interaction parameter (i.e. the more compatible the polymers), the larger the interphase.

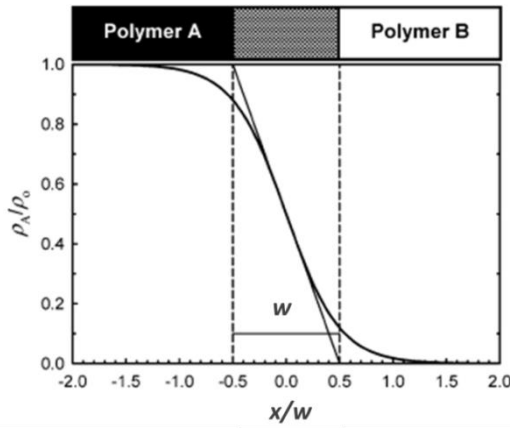


Figure 3: segment density (concentration) profile of the interphase between two immiscible polymers A and B as a function of the distance x from the center of the interphase.²⁴

The impact of the molar masses of both polymers on the size of the interphase has been studied by Broseta.²⁵ If the molar masses are reasonably close and assuming the two polymers have the same Kuhn length b , one can write:

$$w \approx \frac{2b}{\sqrt{6\chi}} \left(1 + \frac{\ln 2}{\chi} \left(\frac{1}{N_A} + \frac{1}{N_B} \right) \right) \quad (\text{Eq. 9})$$

N_A and N_B being the number of Kuhn monomers of polymers A and B, respectively.

In the same work by Helfand,²¹ interfacial tension was also related to the Flory interaction parameter via Equation 10:

$$\gamma = \frac{kT}{b^2} \left(\frac{\chi}{6} \right)^{1/2} \quad (\text{Eq. 10})$$

Here, the lower the value of the Flory interaction parameter, the smaller the interfacial tension (with $\gamma = 0$ meaning polymers are miscible).

Similarly to Broseta's work for the interphase, Tang and Freed²⁶ developed a model to take into account the role of the molar masses in the interfacial tension for symmetric blends (N_A and $N_B = N$) (Equation 10bis):

$$\gamma = \frac{kT}{b^2} \left(\frac{\chi}{6} \right)^{1/2} \left(1 - \frac{1.8}{\chi N} - \frac{0.4}{(\chi N)^2} \right)^{3/2} \quad (\text{Eq. 10bis})$$

In an "engineering" context, being able to measure or calculate accurately the Flory interaction parameter between polymers is then of great importance. For example, block copolymers (BCP) with high Flory interaction parameters have been synthesized over the past few years to challenge the photolithography limit reached in the nanoelectronics industry.^{27, 28} To further decrease the size of the domain periodicity below 10 nm, low molar mass (represented by the degree of polymerization N) block copolymer can advantageously be used since they offer self-assembled features at these scales. However, the incompatibility of the blocks (as quantified by χ) must be chosen high enough so that the degree of segregation (χN) of the blocks is above the segregation limit, meaning that the block copolymer is still nanophase separated. χ is then a crucial measurement to characterize the ability of the block copolymer to produce smaller periodic domains. Another example which will be discussed in more details below consists in the development of nanoblends or in other words polymer blends with nanophases which can display unusual properties (sometimes as simple as transparency).²⁹ Usually, to achieve these morphologies, new processing methods have been developed, such as reactive blending or multilayer coextrusion.^{30, 31} When the compatibility is increased (low positive values of χ), the typical size of the dispersed phase can be decreased, the surface-to-volume ratio increased along with the intermolecular interactions at the interface. Polymers can also display physical properties (glass transition temperature, storage and loss moduli, ability to crystallize...) that differ significantly from those of the bulk when confined at nanometric scales (i.e. sizes comparable to their radius of gyration).^{32, 33}

As stated above, the Flory-Huggins theory is based on a mean-field approximation of a lattice model. In consequence, it neglects (or ignores) several aspects of real blends that can play a role in miscibility, such as blend compressibility, blend composition, chain rigidity, and also differences in monomer chemical structures, shapes, sizes and bonds.^{34, 35} It should be noted that several alternate, more refined theories, have been developed over the years in an attempt to describe more accurately the behavior of polymer solutions or blends, by taking into account part of these parameters, especially compressibility.³⁶⁻³⁹ However, their complexity has made them generally difficult to use in practice and they will not be discussed in details here.

Indeed, due to its relative simplicity (both theoretical and, to a certain extent, experimental), comparing values of χ for different polymer couples is still often used to discuss their relative compatibilities (or more often incompatibilities) when blended or to evaluate phase separation in block copolymers. As a consequence, a measure of this parameter, for a given blend, should provide useful information. However, this measure remains subject to uncertainties, whether due to the experimental technique itself, the experimental

conditions or to the physical and chemical details of the blend composition. The goal of this review was to show that, for these reasons, comparisons of blends using values of the Flory interaction parameter listed in the literature should be handled with care, and conclusions made with caution.

Tambasco⁴⁰ already showed that for partially miscible blends, similar values of χ may give rise to very different behaviors in terms of phase separation while polymer blends with similar chemical species and critical behavior can display very different values for χ .

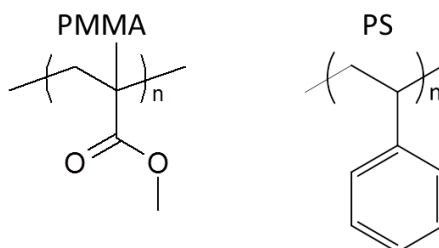


Figure 4: chemical structures for PMMA and PS.

Here, we showed differences in experimental values obtained using different experimental techniques and different polymer samples (molecular weights, dispersity, functionalization such as deuteration...) for a given simple polymer pair, polystyrene (PS) and poly(methyl methacrylate) (PMMA) (structures given in Figure 4).

A deeper analysis of the experimental techniques to measure χ can be found in reference ¹⁶. The experimental values that can be found in the literature are summarized in Table 2.

To summarize, it appears that, even for a “simple” system such as PS/PMMA analyzed with the same experimental technique (say, small-angle scattering) and the same theoretical analysis with the same fitting parameter (for example, here, $b \approx 7 \text{ \AA}$ as chosen by Russell, Callaghan and others), one can get access to experimental values for $\chi_{PS/PMMA}$ showing almost a factor of 2 at a given temperature (for example, from 0.028 to 0.054 at 180 °C with scattering measurements, with a mean value of 0.038 and a standard deviation of 0.009), depending on the nature of the system studied (block or blend, deuterated or not) and its characteristics (molar masses, volume fraction of the blend/block).

The situation is even worse (some results may differ by more than a factor of 5) if different experimental techniques are compared, even if one does not consider “anomalous” results such as negative χ values (for PS/PMMA).

We should state that large differences on the PS and PMMA monomers length are also observed in the literature. If the “real” monomer length is about 2.5 Å for every vinyl monomer, the Kuhn length is usually also obtained from scattering measurements. If Russell reports a value of 6.8 Å for PS, extracted from values of radius of gyration measured by Ballard⁴¹ and 7.3 Å for PMMA measured by SAXS by Kirste⁴² (in an article in German), $b = 18 \text{ \AA}$ for PS and in the range 15-17 Å for PMMA can be obtained using the work of Fetters.^{43, 44} We can then reestimate χ values for some of the studies presented in Table 3 below.

$\chi_{PS/PMMA}$ Measured	T=25 °C	120 °C	162 °C	180 °C	200 °C	250 °C	A	B
Turbidity ⁴⁶	0.014							
Turbidity ⁴⁶	0.011							
Light scattering ⁴⁷	0.025 (30 °C)							
SANS (dPS-b-PMMA) ⁴⁸	0.041	0.0383	0.0373	0.037	0.0362	0.0355	0.028	3.9
SANS (PS-b-dPMMA) ⁴⁹	0.0399	0.0373	0.0365	0.0362	0.0359	0.0353	0.0292	3.19
SANS (dPS-b-dPMMA) ⁴⁹	0.0358	0.0332	0.0325	0.0322	0.0319	0.0312	0.0251	3.2
Estimated from critical molecular weight method (PS/PMMA blend) ^{49, 50 a}	0.0317	0.0291	0.0284	0.0281	0.0278	0.0271	0.021	3.2
SAXS (PS/PMMA) ⁵¹	0.0645	0.0574	0.0552	0.0544	0.0536	0.0518	0.035	8.8
SAXS (PS/PMMA) ⁵²	0.0432	0.0395	0.0385	0.038	0.0376	0.0367	0.0282	4.46
Critical molecular weight method (Flory-Huggins) ⁵⁰					0.028			
Critical molecular weight method (Sanchez-Lacombe) ⁵⁰					0.034			
SANS (from diffusion coefficients) ⁵³		0.0061						
Confocal Raman microscopy (from diffusion coefficients) ⁵⁴		(130 °C) - 0.0316 (FT) or - 0.0131 (ST)	(150 °C) - 0.0338 (FT) or - 0.0152 (ST)					
Interfacial measurements (Wu ⁵⁵) and Helfand's equation ^{23, 56}		0.177	0.0733	0.0462	0.025	0.0012		
Interfacial measurements (Carriere ⁵⁷) and Helfand's equation ^{23, 56}		0.204	0.0892	0.0585	0.0338	0.0034		

^a Obtained by Russell from measurements obtained using different methods and listed in Callaghan's article.

Table 2. Summary of all experimental data for $\chi_{PS/PMMA}$.

Callaghan's analysis can also be reevaluated, since they took 100 cm³/mol for the molar volume of the PS/PMMA blend. However, a more precise estimate of the mean molar volume may be obtained from van Krevelen.⁴⁵ For PS and PMMA, the mean value ($\sqrt{v_A \times v_B}$) is 92.1 cm³/mol (with $v_{PMMA} = 86.5$ cm³/mol; $v_{PS} = 98$ cm³/mol). So depending on the theoretical model chosen for the analysis (Flory or Sanchez-Lacombe) and the value of the fixed physical parameter (here, the molar volume), χ obtained from this single set of experimental measurements can vary from 0.026 to 0.034.

Reestimated values for $\chi_{PS/PMMA}$ using the previously discussed experimental results are then summarized in Table 3 (as a reminder, relevant data from Table 2 used in these comparisons are repeated in Table 3). This shows that the uncertainty concerning fundamental molecular parameters such as the Kuhn monomer length will greatly impact the "measured" value of χ .

We will not discuss here the values for χ that can be obtained using the solubility parameters, which appear even more unreliable in the case of polymer blends.¹⁶

$\chi_{PS/PMMA}$ Measured	120 °C	162 °C	180 °C	200 °C
SANS (dPS-b-PMMA) ⁴⁹	0.0383	0.0373	0.037	0.0362
Critical molecular weight method (Flory-Huggins) ⁵⁰ with $v_0 = 100$ cm ³ /mol				0.028
Critical molecular weight method (Sanchez-Lacombe) ⁵⁰ with $v_0 = 100$ cm ³ /mol				0.034
Reestimated				
Recalculated from ⁴⁹ with Equation 9 and $b \approx 17$ Å (Fetters) ⁵²	0.149	0.146	0.145	0.141
Flory-Huggins with $v_0 = 92.1$ cm ³ /mol (from van Krevelen) ⁴⁵				0.026
Sanchez-Lacombe with $v_0 = 92.1$ cm ³ /mol (from van Krevelen) ⁴⁵				0.031
Recalculated from Fernandez ⁵³ with Equation 9 and Kirste values for b ⁴²	0.103			
Recalculated from Fernandez ⁵³ with Equation 9 and Fetters values ⁵²	0.526			

Table 3: Comparison of experimental and recalculated data for $\chi_{PS/PMMA}$.

To conclude, though χ is often used as a unique parameter, coming from a relatively simple theoretical model, it should be more considered, as Douglas and Bosse put it,⁵⁸ like a "phenomenological model" where all the complex physical and chemical phenomena occurring are hidden in the interaction parameter, which induces many experimental uncertainties when measuring this parameter, and even more when comparing different blends with each other by using this parameter or, for example, the interfacial tension.

1.3. Polymer blends morphologies

Coming back to more macroscopic considerations, the idea behind blending polymers is to achieve properties that cannot be obtained easily (or in a less economical way) with single homo or copolymers. Though some miscible blends have been commercialized (such as Noryl™, a blend of polyphenylene oxide– PPO- and PS) and usually display average properties compared to the two parent polymers (for PS and PPO, the idea is to bring down the cost versus pure PPO, facilitate its processing while obtaining a material with better thermal stability than PS), most of the blends used in the plastic industry come from immiscible polymers that undergo phase separation in the melt state. Though thermodynamic equilibrium should lead to two macroscopic domains for the two phases, separated by a single interface, this equilibrium is reached very slowly, allowing to achieve blends with more complex morphologies.¹ When some mixing energy is brought to the system before coming back to the solid state (usually during processing), different morphologies for the blend may be obtained (see Figure 5).

Product	Supplier	Components (matrix/disperse)	Morphology	Property
Dynamar	Dyneon	PE/PTFE	dilute drops	processibility (adds wall slip)
MB	Dow Corning	PP/PDMS	dilute drops	lubricity
Noryl GTX	GE	PA6/PPO/SB	drops (60%)	dimensional control (H ₂ O uptake)
Zytel ST	Dupont	PA6,6/EP	double emulsion	toughness
Selar	Dupont	PE/PA6,6	lamellar	diffusion barrier
Vectra	Hoechst	PET/LCP	fibers	thermal expansion
TSOP	Mitsubishi/Toyota	PP/PE/EP	cocontinuous	electrical conductivity
Stat-Rite	Goodrich	PP/PU	cocontinuous	electrical conductivity

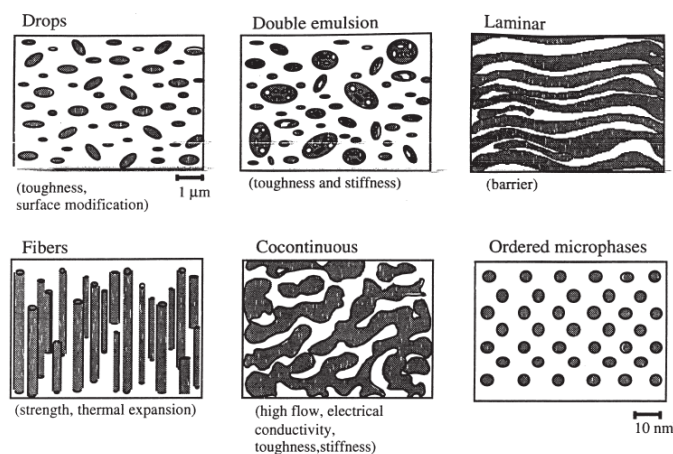


Figure 5: Examples of micro or nano-structured (commercial) blends in relation with macroscopic properties, from ⁵⁹.

The typical morphology in the case of a dispersed phase within a matrix is, because of the interfacial tension, nodular (droplets). The size but also the shape of the morphology can be controlled by materials parameters

(viscosity, interfacial tension, volume fraction of the blend) and processing parameters (type and level of mechanical sollicitation, time of processing, cooling rate...) and micro (or nano) structures that are not thermodynamically stable can be achieved.

The final morphology will, along with the specific interactions between the blend components, have an effect on the macroscopic properties.⁵⁹

To achieve in a controllable way such microstructures via industrially scalable processes (based on melt processing) remains an experimental challenge, especially when control at the nanoscale is targeted.

1.4. Melt blending

We will focus here on coextrusion though other melt blending processing tools have been developed (in particular internal mixers). During coextrusion, high shear stresses are exerted on the melting polymers (initially under pellet or powder form). Disperse phases develop from sheets to fibers to drops during the process. Drops may later on coalesce (see Figure 6⁶⁰).

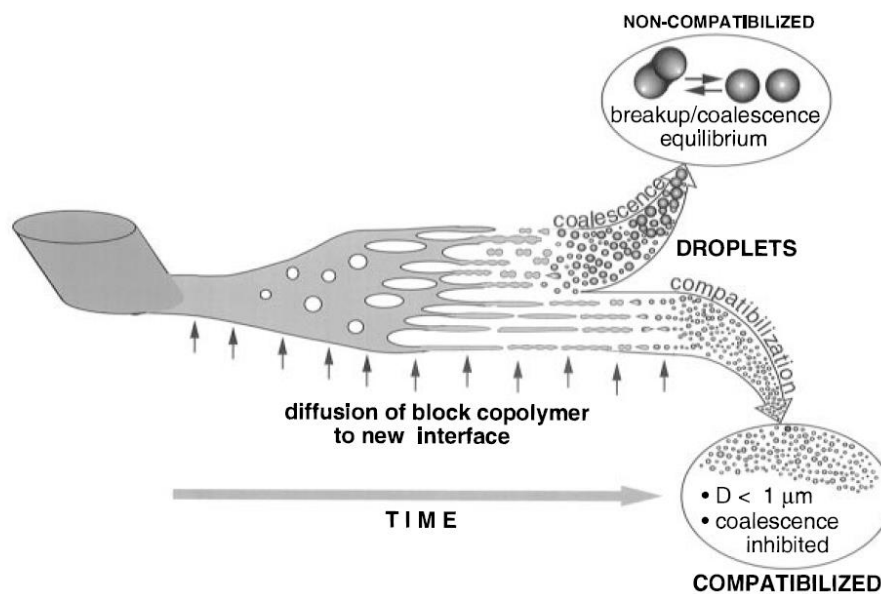


Figure 6: Morphology development during melt blending. Layers of pellets constituting the dispersed phase peel off during extrusion, then stretch into sheets, break into fibers and then droplets. These droplets will coalesce, which can be prevented by the addition of block copolymer locating at the interface (taken from⁶⁰).

The typical size of the drops (D) can be estimated can be estimated by making equal a typical velocity in the process $D\dot{\gamma}$ to the capillary speed η_m/Γ :

$$D = \Gamma/\eta_m\dot{\gamma} \quad (\text{Eq. 11})$$

here, Γ is used to design the interfacial tension instead of the classical γ used before in the manuscript, to avoid confusion with $\dot{\gamma}$ the shear rate (η_m being the viscosity of the matrix). With Γ on the order of 1 mN/m, $\eta_m \sim 1000$ Pa.s and $\dot{\gamma} \sim 10$ s⁻¹, the typical size of the drops is $D \sim 0.1$ μm .

This is usually smaller than what is typically observed in classical blends because it does not take into account the subsequent coalescence which occurs even at small concentrations of the dispersed phase (> 1 %). Typical sizes are on the 1-10 μm range, unless copolymers are added, which lower the interfacial tension (i.e. reduces the equilibrium size) and prevent coalescence by stabilizing the interface. In such cases submicronic droplets can be achieved.

Because drops are actually the last morphology to develop, the basic principle to obtain other ones such as those presented in figure 5 is to control the processing tool and be able to use it to stop the morphologies development at different stages. These morphologies, such as the lamellar one, are transitory states. Some processing and materials parameters, for example in extrusion, may favor the development of the lamellar state: high processing speed, a dispersed phase more fluid than the matrix, lower interfacial tension...

1.5. Nanolayer Coextrusion

For several materials applications, notably barrier properties, lamellar morphology is often sought, but difficult to control. An easier path is then to coextrude polymers to obtain materials constituted of stacked continuous layers. The idea is here to melt simultaneously two polymers using two extruders connected together. This process is classically used to design barrier films, with a brittle but barrier layer in the middle (for example EVOH) capped by two flexible layers (for example PE). A tie-layer is often added to improve adhesion between the two polymers (using a grafted copolymer such as PE-g-EVOH). This classic technique leading to 3 or 5 layers materials can only achieve micronic thicknesses for the layers.

However, as has been stated earlier, multiplying interfaces and inducing confinement effects at smaller submicronic or nanometric scale (similar to a “nacre-like” structure) may in some cases lead to much improved macroscopic properties, such as impact resistance as in the case of nacre. In consequence, new processing tools are being developed to achieve this control at the nanoscale.

One of these tools is derived from classical coextrusion, and can be named multilayer coextrusion (or nanolayer coextrusion depending on the scale reached). Instead of a few micronic layers, this processing tool allows fabricating materials made of thousands of continuous layers of alternating polymers, with each layer having nanometric thicknesses. A very complete overview of all the possible variations of this process has been made by C. Sollogoub in his “Habilitation à Diriger les Recherches” (in French).⁶¹ Here we will present in detail only the version developed in the laboratory and some of the main results from the literature. The multilayer coextrusion process has actually been developed industrially in the 60’s and 70’s, mainly by Tollar and later on Schrenk at Dow Chemicals.^{62, 63} The principle is based on the “baker’s transformation” (named because of its analogy with rolling and cutting dough) using static mixers added in series in the extrusion feedblock (see Figure 7). These static mixers may be called Interfacial Surface Generator (ISG) or Layer Multiplying Elements (LME).

However, most of the studies using this processing tool have been performed by Prof. Eric Baer at Case Western Reserve University since the early 90's.⁶⁵⁻⁶⁷ The early papers were mainly focused on the microstructure of the obtained materials and on the mechanical properties (fatigue, reinforcement). Roughly 10 years later, after several improvements to the process, nanoscale was reached and most of the studies shifted towards gas barrier and optical properties.⁶⁸⁻⁷⁰

One of the most striking results has been the demonstration that new crystalline morphologies can be obtained for several semi-crystalline polymers when confined in layers with thicknesses below 100 nm. For some polymers, such as poly(ethylene oxide) (PEO) or polycaprolactone (PCL), the lamellar morphology lead to a two orders of magnitude decrease of the oxygen permeability compared to the bulk value (i.e. to a spherulitic morphology). (see Figure 8 and for more details, for example references^{71,72} among others).

Another main result concerns the design of what was claimed to be a new material constituted only of interphase, by "forcing" amorphous immiscible polymers (polycarbonate (PC) and PMMA) into layers smaller than the typical dimension of the interphase w (see Equations 8 and 9).⁷³ The blurring of the AFM (Atomic Force Microscopy) images as layers were made thinner was correlated to a merging of the glass transition temperature (T_g) and an increase in permeability suggesting that a PC/PMMA "blend" could actually been obtained for targeted individual layers below 12 nm (see Figure 9). Indeed no individual layers have been observed by AFM and measured for $h_{nom} < 20$ nm. Blurring of the image was attributed to the presence of the interphase having a similar size than the layers which lowered the contrast.

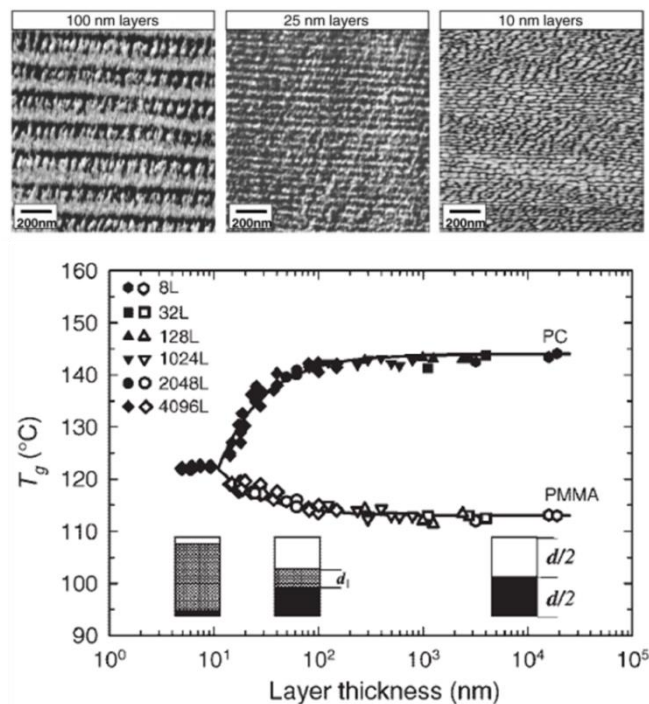


Figure 9: Interphase material obtained by forcing PC and PMMA into layers thinner than 10 nm.⁷³

A subsequent article confirmed this result using a permeability model and showed that layer breakups were observed for targeted thicknesses below 5 nm.⁷⁴ These breakups were also identified in other systems such as confined PEO discussed above, but their origin has never been discussed in details: it will be the subject of chapter 3 of this manuscript. The model linking permeability, interphase and Flory interaction parameter was extended to other glassy polymer pairs showing different degree of compatibility.^{24, 75} Nonetheless, it should be noted that in a more recent article dealing with films produced by the same group, layers having 12 nm nominal thicknesses are shown on AFM images presenting very good contrast, with no shifts in the measured T_g s.⁷⁶ Some other questions could also be raised concerning the model proposed. The interphase thickness was determined using solubility parameters, which, as stated above, is probably inaccurate for polymer blends.¹⁶ In consequence, the interphase for PC/PMMA estimated at 12 nm may in consequence be overestimated. Helfand's equation and literature data for PC/PMMA Flory interaction parameter leads to an interphase thickness around 5 nm.¹⁶ Still, if many open questions remain concerning these systems, they should be of great interest because they allow studying polymer interphases on "bulk-like" materials, i.e. while using conventional characterization techniques for polymeric materials.²⁴

Other properties (such as electric or dielectric properties)⁷⁷ have been studied. The capacity to produce gradient films,⁷⁸ nano-fibers⁷⁹ or foams⁸⁰ has also been demonstrated but will not be discussed in further details here. Note that these 20 years of research dedicated on multilayer films resulted in the launch of a company processing such films at industrial scales, [PolymerPlus™](#).

Let us now move back to surface and interfacial tension related phenomena, and briefly describe how wetting, adhesion on polymer surfaces and mechanical instabilities (buckling, wrinkling, folding) are affected by key parameters such as viscoelasticity, surface patterning and surface chemistry.

1.6. Surface and Interfacial tension related phenomena at polymer interfaces.

In this section we will briefly recall (more or less) basic notions on wetting or dewetting, adhesion (and to a lesser extend friction) that will be used or discussed later on in the manuscript. For more detailed descriptions, one can refer to many textbooks such as the already cited^{1, 8, 81}. Most of this section is based mainly on these books.

1.6.1. Wetting on a planar surface

When a liquid drop is deposited on a planar solid (or liquid) surface, it can either spreads completely or remain stuck in place. In that case, the drop adopts, at equilibrium, the shape of a spherical cap (if the drop volume is not too big) resting on the substrate with a contact angle θ_e (see Figure 10).⁸

This contact angle is determined by balancing the capillary forces acting on the triple contact line (at the interface between solid, liquid and gas) onto the solid plane. Per unit length, this gives the well-known Young's relation (established in 1805):

$$\gamma_{LV} \cos(\theta_e) + \gamma_{SL} = \gamma_{SV} \quad (\text{Eq. 12})$$

γ_{LV} and γ_{SV} being the surface tensions of the liquid and the solid respectively, and γ_{SL} the interfacial tension between the solid and the liquid.

Note that the contact angle can also be defined and determined using Neumann's triangle when a liquid drop is deposited on an immiscible fluid substrate which will deform upon deposition of the droplet.

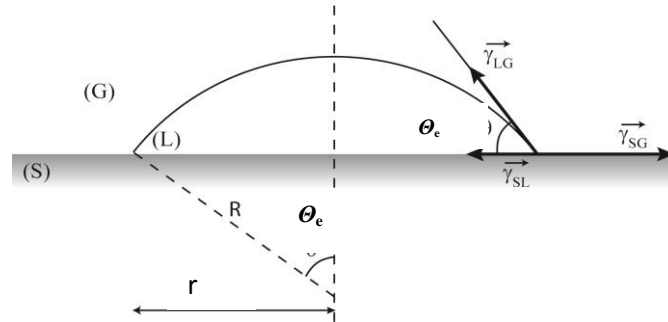


Figure 10: Liquid spherical cap resting on a solid substrate at equilibrium.

The spreading (or not) of the drop is characterized by the spreading parameter, defined as $S = \gamma_{SV} - (\gamma_{SL} + \gamma_{LV})$ (Eq. 13)

which compares the surface energy of the dry state and of the completely wet state.

If $S \geq 0$, the liquid spreads and totally wets the surface ($\theta_e = 0$). The resulting film has a (nanometric) thickness which depends on the competition between capillary and molecular (van der Waals forces). We will go back to this later on when discussing dewetting of thin films.

If the spreading parameter is negative, then the liquid partially wets the surface and adopts the spherical shape with an equilibrium contact angle θ_e between 0 and 180°.

Note that if the drop volume is too big, gravity cannot be neglected and the drop loses its spherical cap shape.

In that case, it will flatten to adopt a maximum (critical) height h_c linked to the capillary length $l_c = \sqrt{\gamma_{LV}/\rho g}$ (the capillary length is the characteristic depth within a liquid of density ρ submitted to gravity at which Laplace pressure balances hydrostatic pressure). The capillary length is usually millimetric. For typical sizes much smaller than this length, gravity is negligible and capillary effects dominate. In the contrary, one has to take gravity into account and the force equilibrium writes itself:

$$\frac{1}{2} \rho g h^2 + \gamma_{SV} - (\gamma_{SL} + \gamma_{LV}) = 0 \quad (\text{Eq. 14})$$

Using Young's relation (Eq. 11), this leads to

$$h_c = 2l_c \sin\left(\frac{\theta_e}{2}\right) \quad (\text{Eq.15})$$

1.6.2. Wetting on real surfaces

However, the unicity of the equilibrium contact angle as predicted by Young is an idealized case assuming a perfectly clean, planar, undeformable solid substrate. In real cases with chemical and physical defects on the surface, or when viscoelasticity of the substrate has to be considered, wetting may become much more complicated and the contact angle not unique, due to phenomena such as the pinning of the contact line on the substrate. One then defines an advancing contact angle (the maximum contact angle an inflating drop reaches before the contact line moves) and a receding contact angle (the minimum contact angle before the contact line of a deflating drop moves). The difference between these two angles defines the contact angle hysteresis, which characterizes the role of all defects of the substrate and interactions between the liquid and the substrate.

Even when the hysteresis is small, defects such as surface roughness or chemical heterogeneities can greatly modify the equilibrium contact angle compared to the value obtained through the simple Young's relation. Two cases of roughness have been modeled by Cassie⁸² and Wenzel.⁸³

Wenzel's relation which applies to rough substrates is given by Equation 16:

$$\cos(\theta^*) = r \cos(\theta_e) \quad (\text{Eq. 16})$$

where θ^* is the equilibrium contact angle on a rough substrate defined by a roughness coefficient r with $r > 1$ ($r = 1$ for the smooth substrate). If Young's contact angle is smaller than 90° (hydrophilic solid if the liquid considered is water), then roughness will further decrease the contact angle. In the opposite case (hydrophobic solid), roughness will increase the contact angle. The hypothesis here is that the drop wets all the substrate underneath despite the roughness. The Wenzel state is then usually valid for very large drops when compared to the typical dimensions of the roughness and for low aspect ratio of the substrate features.

When chemical heterogeneities are considered, Cassie-Baxter model usually applies. Here, the substrate is made of two species 1 and 2 with fractional surface areas f_1 and f_2 and having Young's contact angle θ_1 and θ_2 . Then

$$\cos \theta^* = f_1 \cos \theta_1 + f_2 \cos \theta_2 \quad (\text{Eq. 17})$$

If one of the "species" is air (which then means that, contrary to Wenzel model, air "bubbles" are trapped underneath the drop in between substrate features, also known as fakir state), the equation reduces to $\cos \theta^* = f_1(\cos \theta_1 + 1) - 1$. Cassie-Baxter model describes what is called the "lotus effect" (superhydrophobicity of the lotus leaf due to trapped air bubbles within the nanometric roughness of the leaf).⁸⁴ The transition from a Wenzel state to a Cassie state should happen for drops that become smaller than l^2/e if l and e are the typical amplitude and wavelength of the features.⁸⁵

1.6.3. Dewetting of thin films

The reverse phenomenon, dewetting, consists in the spontaneous withdrawal of a liquid film from a hostile surface, i.e. when the spreading parameter is negative (for $S > 0$, a film is always stable). In such a situation, putting a large amount of liquid over a solid surface will lead to dry patches and wet zones of thickness h_c . Dewetting of a film can occur via two mechanisms which, in theory, depend mainly on the film thickness. One is the nucleation and growth of dry zones (metastable state) occurring for thicker films. The other, termed spinodal dewetting, is the spontaneous amplification of capillary waves (unstable state) and occur for thinner

films. These two mechanisms have been described theoretically, along with the dynamics of dewetting, by Brochard-Wyart⁸⁵ more than 20 years ago.

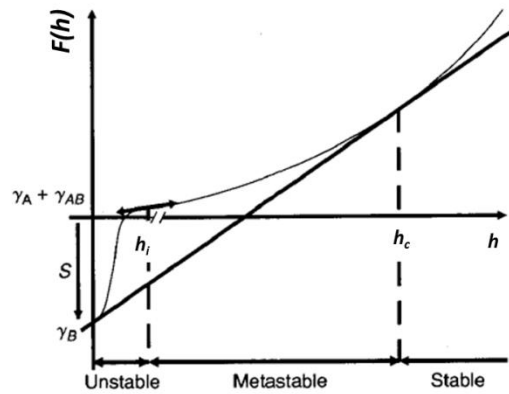


Figure 11: Spinodal and nucleation and growth dewetting regimes described by the variation of the free energy F of the film as a function of its thickness h .^{8, 86}

Assuming the spreading parameter is negative, a film will dewet if capillary forces overcome gravity, i.e. for thicknesses below h_c as defined in equation 15 ($h_c \sim 100 \mu\text{m}$). Below such thicknesses, the film is metastable. When the thickness is such that intermolecular forces become comparable to capillary forces, $h_i \sim \left(\frac{A_H}{6\pi\gamma_{LV}}\right)^{1/2} \sim 1 - 10 \text{ nm}$, the film becomes unstable (see Figure 11). Note that in this case, the molecular length defined by Brochard⁸⁶ differs from a factor 4 compared to the one introduced by Israelachvili¹² (see Equation 2, section 2.1.2.).

It is noteworthy that even in the thickness regime where van der Waals forces cannot be neglected, nucleation and growth may still occur, since it may have faster kinetics and impurities leading to nucleation are hard to avoid in real systems. Reiter⁸⁷ first evidenced experimentally spinodal dewetting of PS thin films on silicon substrates. It has then been studied in the case of thin films on top of liquid substrates, mostly with immiscible polymers such as PS and PMMA.⁸⁸⁻⁹²

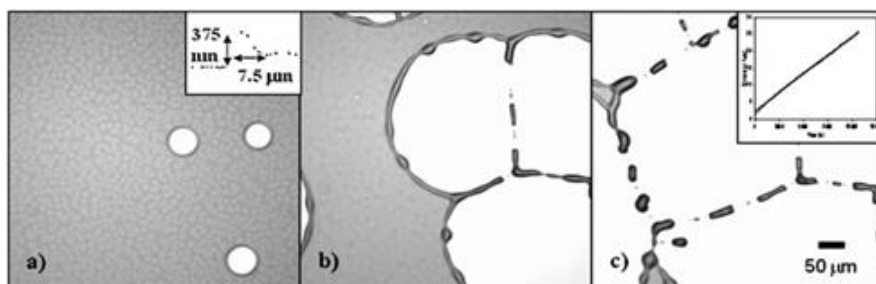


Figure 12: Dewetting of a PCL thin film on a ODS substrate as a function of time.⁹³

Dewetting can be decomposed in four stages as a function of time: first, holes formation. As the hole is formed, the excess of matter locates at a rim around the hole. Second, holes growth. Third, coalescence of the rims into cylindrical shapes that later on break into droplets (see Figure 12⁹³).

Several regimes which will influence the dynamics of dewetting can be expected and have been observed experimentally⁸⁸⁻⁹¹, mainly due to the viscosity ratio and size ratio between the film rim and substrate thickness, and the surface and interfacial tensions of the two polymers at the chosen temperature. It should be noted, as stated in reference⁸⁸, that the dynamics of dewetting is not affected by the original mechanism of hole formation. Let us now discuss briefly the different scenarios for the dewetting of a thin liquid film on top of an immiscible polymeric substrate (this is adapted from reference⁹⁴).

Liquid-liquid dewetting

If $\eta_{substrate} < \eta_{film} / \theta_e$, we are in the liquid-liquid dewetting case. In this case, the viscous dissipation is dominated by the contribution of the substrate. If the substrate is very thick, the size of the holes grows linearly with time, i.e. the dewetting velocity is constant.

This changes when the thickness of the substrate becomes comparable to the size of the rim (usually on the order of 1 μm). The dewetting velocity then becomes time dependent, following the equation predicted by Brochard-Wyart⁸⁶ (Equation 18):

$$v = \frac{2}{3} \left(\frac{\gamma^2 h_{substrate}^2 \theta_e}{\eta_{substrate}^2 h_{film}} \right)^{1/3} t^{-1/3} \quad (\text{Eq. 18})$$

where $h_{substrate}$ and h_{film} are the thicknesses of the substrate and the film respectively, and $\eta_{substrate}$ the viscosity of the substrate.

Liquid-solid dewetting

However, if $\eta_{substrate} > \eta_{film} / \theta_e$, then the dewetting is those of a liquid on a "solid"-like substrate (even though the substrate is actually in a molten state).

In that case, the regime is viscous and the growth of the hole is controlled by the competition of capillary forces and viscous flow of the film. The radius of the growing hole is predicted to grow linearly with time^{86, 88} with a speed following Equation 19:

$$v = \frac{1}{12 \ln \sqrt{2}} \frac{\gamma_{film}}{\eta_{film}} \theta_e^3 \quad (\text{Eq. 19})$$

1.6.4. Work of adhesion, adhesion between glassy or rubbery polymeric interfaces

Let us conclude by a few words on adhesion of polymer interfaces. If we consider an interface between two surfaces of polymers A and B (with surface tensions γ_A and γ_B), characterized by an interfacial tension γ_{AB} , the reversible thermodynamic work of adhesion writes $W_{AB} = \gamma_A + \gamma_B - \gamma_{AB}$. This is the reversible free energy change one has to provide to go from one interface to two separated surfaces. If A is a liquid and B a solid, one can use the Young's equation to obtain Young-Dupré's equation for the work of adhesion (Equation 20):

$$W_{AB} = \gamma_A (1 + \cos \theta_e) \quad (\text{Eq. 20})$$

For polymeric surfaces, this thermodynamic work of adhesion is of the order of the surface energies, *i.e.* ~ 0.1 - 0.01 J/m^2 . However, the work of adhesion has been measured (through the fracture energy) at much higher values for polymer interfaces (up to 1000 J/m^2 for high molecular weight glassy polymers). The fact that interfacial fracture occurs far from thermodynamic reversibility, along with dissipative mechanisms (interphase, entanglements at the interface...) explain the toughness of these interfaces.¹

Glassy interfaces

As showed by Mikos and Peppas, brittle fracture in glassy polymers is correlated to entanglements.⁹⁵ The variation of the work of fracture per unit area G_F (*i.e.* the work of adhesion or fracture energy) as a function of the molar mass has been described using Equation 21:

$$G_F(M) = G_{F\infty} \left(1 - \frac{2M_e}{M}\right) \quad (\text{Eq. 21})$$

where $G_{F\infty}$ is the extrapolated fracture energy at infinite molar mass which can be estimated from molecular parameters⁹⁵ and M_e the molar mass between entanglements.

For symmetric interfaces, say PMMA, $G_{F\infty}$ is on the order of 150 J/m^2 and the molar mass between entanglements close to 10000 g/mol . For samples with molar masses on the order of M_e , the work of fracture is less than 10 J/m^2 . The predicted thermodynamic work of adhesion, in that case, is $W_{PMMA} = 2 \gamma_{PMMA} \approx 0.08 \text{ J/m}^2$ and should be experimentally valid if PMMA were an ideal brittle solid, which confirms the presence of dissipative mechanisms occurring the fracture of glassy polymers. Similar results have been reported for PS.¹ The link between fracture energy and entanglements is due to the fact that energy dissipation occurs through crazing, a mechanism linked to the presence of entanglements in polymeric materials.

The fracture energy at the interface between two glassy polymers will also depend on entanglements. In the case of two identical polymers annealed above glass transition temperature (auto-adhesion or welding), the fracture energy can be lower than expected because the maximum degree of entanglements at the interface has not been reached (kinetics reason). As discussed above, for immiscible polymers, the interphase or interfacial region where the two polymers actually mix is usually fairly small, which limits the degree of entanglements achievable.

The fracture energy for PS/PMMA interfaces has been measured by Brown close to 10 J/m^2 .^{96, 97} This value is way lower than the fracture energy for entangled PS or PMMA, and similar to the value for unentangled systems.

This can be explained by looking at the size of the interphase for PS/PMMA. It has been measured in Russell's group close to 54 \AA at $170 \text{ }^\circ\text{C}$.⁹⁸ On the other hand, the molar mass between entanglements for both PS and PMMA can be estimated⁴³ on the order of 70 \AA for both polymers. One can then assume that the interphase region is mostly unentangled, giving poor interfacial adhesion between PS and PMMA.

This correlation between interphase, entanglements, and fracture energy between immiscible polymer interfaces has been confirmed by the work of Creton and Brown⁹⁹ on PS/poly(2-vinylpyridine) PVP which is less compatible with PS than PMMA. Hence, the fracture energy is 1.5 J/m^2 while the interphase is smaller than 20 \AA .¹⁰⁰

Brown developed a model (which we will not describe in further details here) in which he showed that for an interface fracturing through formation of crazes, the fracture energy is proportional to the number of effectively entangled chains crossing the interface.¹⁰¹

These results showing the weaknesses of polymer interfaces explain why many immiscible blends have poor intrinsic mechanical properties. They also allow to understand why the addition of diblock (or other types of) copolymers which will segregate at the interfaces and facilitate stress transfers between the phases. Creton⁹⁹ for example showed that the addition of well-chosen copolymers can improve the fracture toughness of PS-PVP interfaces by almost three decades.

Rubbery interfaces

Similarly to what occurs for glassy polymers, adhesion between rubbery interfaces (polymer melts or elastomers) is usually much higher than the thermodynamic work of adhesion. In that case, dissipative mechanisms are usually due to viscoelastic phenomena rather than craze formation.¹ To determine the elastic response, Johnson, Kendall and Roberts have developed an experimental technique (known simply as the JKR probe test).¹⁰² It consists in measuring the work of adhesion between a spherical elastomeric probe and a glass slide (or, on later versions, a flat elastomeric substrate). The radius of contact a , displacement δ and force applied P (in some cases the displacement is imposed, not the force) are monitored (see Figure 13). In case of a non-adhesive contact between elastic solids (Hertzian contact), we have (Equation 22):

$$a^3 = \frac{3}{4} \frac{1-\nu^2}{\pi E} RP \quad (\text{Eq. 22})$$

where ν is the Poisson's ratio and E the Young's modulus of the elastomer, and R the radius of the probe.

In case of an adhesive contact, the radius of contact a is bigger than the Hertzian prediction, and has been described by Johnson et al.¹⁰² in Equation 23:

$$a^3 = \frac{3}{4} \frac{1-\nu^2}{\pi E} R (P + 3G_0\pi R + (6G_0\pi RP + (3G_0\pi R)^2)^{\frac{1}{2}}) \quad (\text{Eq. 23})$$

G_0 being the limiting value of the fracture energy at zero rate of crack growth, or adhesion energy (or at non-zero rate if dissipative mechanisms remain localized at the fracture tip).

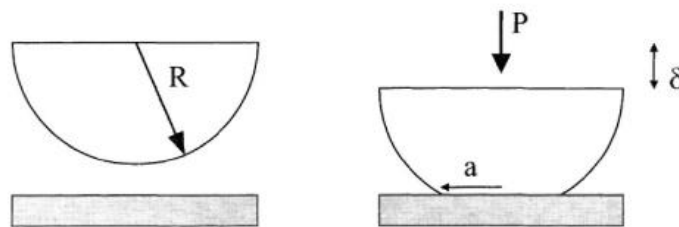


Figure 13: principle of the JKR probe test (from ¹).

In case of a PDMS probe on a silicon wafer grafted with PDMS brushes, Deruelle et al.¹⁰³ have shown that the adhesion energy was in that case fairly close to the thermodynamic work of adhesion, i.e. $2\gamma_{PDMS}$ when the two surfaces approach each other. The hysteresis often captured in a JKR test may then be related to interfacial phenomena (viscoelastic effects such as dangling chains crossing the interfaces, chemical reactions at the interfaces)... Several more refined models have been proposed, which will not be discussed here but have been the topic a review by E. Barthel.¹⁰⁴ The effect of surface roughness has also been the core of many studies since the early work of Fuller and Tabor¹⁰⁵, and has regained interest over the last 10 years with the help of various lithography techniques to design well-controlled patterned elastomeric surfaces (see for example^{106, 107} among many other studies since). Generally it is observed that adhesion is enhanced on rough substrates. However, coupled effects of these various parameters, mainly viscoelasticity, chemical interactions and roughness on adhesion have still to be understood in details.

1.7. References

1. Jones, R. A. L.; Randal, W. R., *Polymers at Surfaces and Interfaces*. Cambridge University Press: **1999**.
2. Barner-Kowollik, C.; Goldmann, A. S.; Schacher, F. H., Polymer Interfaces: Synthetic Strategies Enabling Functionality, Adaptivity, and Spatial Control. *Macromolecules* **2016**, *49*, (14), 5001-5016.
3. de Gennes, P. G., CHAPTER 3 - Mechanical Properties of Polymer Interfaces A2 - Sanchez, Isaac C. In *Physics of Polymer Surfaces and Interfaces*, Butterworth-Heinemann: Boston, **1992**; pp 55-71.
4. Sanchez, I. C., Preface. In *Physics of Polymer Surfaces and Interfaces*, Butterworth-Heinemann: Boston, **1992**; pp ix-x.
5. https://en.wikipedia.org/wiki/Surface_energy
6. Finio, B. (2015, June 26). Measuring Surface Tension of Water with a Penny. Retrieved September 1, 2016 from http://www.sciencebuddies.org/science-fair-projects/project_ideas/Chem_p021.shtml
7. Andreotti, B.; Baumchen, O.; Boulogne, F.; Daniels, K. E.; Dufresne, E. R.; Perrin, H.; Salez, T.; Snoeijer, J. H.; Style, R. W., Solid capillarity: when and how does surface tension deform soft solids? *Soft Matter* **2016**, *12*, (12), 2993-2996.
8. De Gennes, P. G.; Brochard-Wyart, F.; Quéré, D., *Capillarity and Wetting Phenomena*. Springer-Verlag: New York, **2004**.
9. https://en.wikipedia.org/wiki/Surface_energy
10. https://en.wikipedia.org/wiki/Surface_tension
11. Hamaker, H. C., The London van der Waals attraction between spherical particles. *Physica* **1937**, *4*, (10), 1058-1072.
12. Israelachvili, J. N., Chapter 13 - Van der Waals Forces between Particles and Surfaces. In *Intermolecular and Surface Forces (Third Edition)*, Academic Press: San Diego, pp 253-289, **2011**.
13. Demarquette, N. R., Evaluation of experimental techniques for determining interfacial tension between molten polymers. *International Materials Reviews* **2003**, *48*, (4), 247-269.
14. Xing, P.; Bousmina, M.; Rodrigue, D.; Kamal, M. R., Critical Experimental Comparison between Five Techniques for the Determination of Interfacial Tension in Polymer Blends: A Model System of Polystyrene/Polyamide-6. *Macromolecules* **2000**, *33*, (21), 8020-8034.
15. Wu, S., Formation of dispersed phase in incompatible polymer blends: Interfacial and rheological effects. *Polymer Engineering & Science* **1987**, *27*, (5), 335-343.
16. Miquelard-Garnier, G.; Roland, S. b., Beware of the Flory parameter to characterize polymer-polymer interactions: A critical reexamination of the experimental literature. *European Polymer Journal* **2016**, *84*, 111-124.
17. Flory, P. J., Thermodynamics of High Polymer Solutions. *The Journal of Chemical Physics* **1942**, *10*, (1), 51-61.
18. Huggins, M. L., Theory of Solutions of High Polymers1. *Journal of the American Chemical Society* **1942**, *64*, (7), 1712-1719.
19. Rubinstein, M.; Colby, R. H., *Polymer physics*. Oxford University Press: Oxford, **2003**; p 440.
20. Utracki, L. A., *Polymer Blends Handbook*. Springer Netherlands: **2003**.
21. Helfand, E.; Sapse, A. M., Theory of unsymmetric polymer-polymer interfaces. *The Journal of Chemical Physics* **1975**, *62*, (4), 1327-1331.
22. Saulnier, F. Dynamic processes at polymeric interfaces. Université Pierre et Marie Curie - Paris VI, **2003**.
23. Helfand, E.; Tagami, Y., Theory of the interface between immiscible polymers. *Journal of Polymer Science Part B: Polymer Letters* **1971**, *9*, (10), 741-746.
24. Liu, R. Y. F.; Bernal-Lara, T. E.; Hiltner, A.; Baer, E., Interphase materials by forced assembly of glassy polymers. *Macromolecules* **2004**, *37*, (18), 6972-6979.
25. Broseta, D.; Fredrickson, G. H.; Helfand, E.; Leibler, L., Molecular weight and polydispersity effects at polymer-polymer interfaces. *Macromolecules* **1990**, *23*, (1), 132-139.
26. Tang, H.; Freed, K. F., Interfacial studies of incompressible binary blends. *The Journal of Chemical Physics* **1991**, *94*, (9), 6307-6322.
27. Bates, C. M.; Maher, M. J.; Janes, D. W.; Ellison, C. J.; Willson, C. G., Block Copolymer Lithography. *Macromolecules* **2013**, *47*, (1), 2-12.
28. Sinturel, C.; Bates, F. S.; Hillmyer, M. A., High χ -Low N Block Polymers: How Far Can We Go? *ACS Macro Letters* **2015**, *4*, (9), 1044-1050.

29. Thomas, S.; Shanks, R.; Chandrasekharakurup, S., Preface. In *Nanostructured Polymer Blends*, William Andrew Publishing: Oxford, **2013**; pp xv-xvi.
30. Hu, G. H.; Cartier, H.; Plummer, C., Reactive extrusion: Toward nanoblends. *Macromolecules* **1999**, *32*, (14), 4713-4718.
31. Ponting, M.; Hiltner, A.; Baer, E., Polymer nanostructures by forced assembly: Process, structure, and properties. *Macromolecular Symposia* **2010**, *294*, (1), 19-32.
32. Alcoutlabi, M.; McKenna, G. B., Effects of confinement on material behaviour at the nanometre size scale. *Journal of Physics-Condensed Matter* **2005**, *17*, (15), R461-R524.
33. Luengo, G.; Schmitt, F.-J.; Hill, R.; Israelachvili, J., Thin Film Rheology and Tribology of Confined Polymer Melts: Contrasts with Bulk Properties. *Macromolecules* **1997**, *30*, (8), 2482-2494.
34. Dudowicz, J.; Freed, K. F., Effect of monomer structure and compressibility on the properties of multicomponent polymer blends and solutions: 1. Lattice cluster theory of compressible systems. *Macromolecules* **1991**, *24*, (18), 5076-5095.
35. Dudowicz, J.; Freed, M. S.; Freed, K. F., Effect of monomer structure and compressibility on the properties of multicomponent polymer blends and solutions. 2. Application to binary blends. *Macromolecules* **1991**, *24*, (18), 5096-5111.
36. Bates, F. S.; Fredrickson, G. H., Conformational Asymmetry and Polymer-Polymer Thermodynamics. *Macromolecules* **1994**, *27*, (4), 1065-1067.
37. Dickman, R.; Hall, C. K., Equation of state for chain molecules: Continuous space analog of Flory theory. *The Journal of Chemical Physics* **1986**, *85*, (7), 4108-4115.
38. Freed, K. F.; Dudowicz, J., Lattice Cluster Theory for Pedestrians: The Incompressible Limit and the Miscibility of Polyolefin Blends. *Macromolecules* **1998**, *31*, (19), 6681-6690.
39. Sanchez, I. C.; Lacombe, R. H., An elementary equation of state for polymer liquids. *Journal of Polymer Science: Polymer Letters Edition* **1977**, *15*, (2), 71-75.
40. Tambasco, M.; Lipson, J. E. G.; Higgins, J. S., Blend Miscibility and the Flory-Huggins Interaction Parameter: A Critical Examination. *Macromolecules* **2006**, *39*, (14), 4860-4868.
41. Ballard, D. G. H.; Wignall, G. D.; Schelten, J., Measurement of molecular dimensions of polystyrene chains in the bulk polymer by low angle neutron diffraction. *European Polymer Journal* **1973**, *9*, (9), 965-969.
42. Kirste, V. R. G., Neue vorstellungen über statistische fadenknäuel. *Die Makromolekulare Chemie* **1967**, *101*, (1), 91-103.
43. Fetters, L. J.; Lohse, D. J.; Richter, D.; Witten, T. A.; Zirkel, A., Connection between Polymer Molecular Weight, Density, Chain Dimensions, and Melt Viscoelastic Properties. *Macromolecules* **1994**, *27*, (17), 4639-4647.
44. Mark, J. E., *Physical Properties of Polymers Handbook*. Springer: **2006**.
45. Van Krevelen, D. W.; Te Nijenhuis, K., Chapter 8 - Interfacial Energy Properties. In *Properties of Polymers (Fourth Edition)*, Elsevier: Amsterdam, **2009**; pp 229-244.
46. Stockmayer, W. H.; Stanley, H. E., Light Scattering Measurement of Interactions between Unlike Polymers. *The Journal of Chemical Physics* **1950**, *18*, (1), 153-154.
47. Fukuda, T.; Nagata, M.; Inagaki, H., Light scattering from ternary solutions. 1. Dilute solutions of polystyrene and poly(methyl methacrylate). *Macromolecules* **1984**, *17*, (4), 548-553.
48. Russell, T. P.; Hjelm, R. P.; Seeger, P. A., Temperature dependence of the interaction parameter of polystyrene and poly(methyl methacrylate). *Macromolecules* **1990**, *23*, (3), 890-893.
49. Russell, T. P., Changes in polystyrene and poly(methyl methacrylate) interactions with isotopic substitution. *Macromolecules* **1993**, *26*, (21), 5819-5819.
50. Callaghan, T. A.; Paul, D. R., Interaction energies for blends of poly(methyl methacrylate), polystyrene, and poly(α -methylstyrene) by the critical molecular weight method. *Macromolecules* **1993**, *26*, (10), 2439-2450.
51. Stühn, B., The relation between the microphase separation transition and the glass transition in diblock copolymers. *Journal of Polymer Science Part B: Polymer Physics* **1992**, *30*, (9), 1013-1019.
52. Zhao, Y.; Sivaniah, E.; Hashimoto, T., SAXS Analysis of the Order-Disorder Transition and the Interaction Parameter of Polystyrene-block-poly(methyl methacrylate). *Macromolecules* **2008**, *41*, (24), 9948-9951.
53. Fernandez, M. L.; Higgins, J. S.; Penfold, J.; Ward, R. C.; Shackleton, C.; Walsh, D. J., Neutron reflection investigation of the interface between an immiscible polymer pair. *Polymer* **1988**, *29*, (11), 1923-1928.
54. Hu, C.; Chen, X.; Chen, J.; Zhang, W.; Zhang, M. Q., Observation of mutual diffusion of macromolecules in PS/PMMA binary films by confocal Raman microscopy. *Soft Matter* **8**, (17), 4780-4787.

55. Wu, S., Surface and interfacial tensions of polymer melts. II. Poly(methyl methacrylate), poly(n-butyl methacrylate), and polystyrene. *The Journal of Physical Chemistry* **1970**, 74, (3), 632-638.
56. Helfand, E.; Tagami, Y., Theory of the Interface between Immiscible Polymers. II. *The Journal of Chemical Physics* **1972**, 56, (7), 3592-3601.
57. Carriere, J. C.; Biresaw, G.; Sammler, L. R., Temperature dependence of the interfacial tension of PS/PMMA, PS/PE, and PMMA/PE blends. *Rheologica Acta* **2000**, 39, (5), 476-482.
58. Bosse, A. W.; Douglas, J. F., The osmotic virial formulation of the free energy of polymer mixing. *The Journal of Chemical Physics* **2015**, 143, (10), 104903.
59. Macosko, C. W., Morphology development and control in immiscible polymer blends. *Macromolecular Symposia* **2000**, 149, (1), 171-184.
60. Macosko, C. W.; Guégan, P.; Khandpur, A. K.; Nakayama, A.; Marechal, P.; Inoue, T., Compatibilizers for Melt Blending: Premade Block Copolymers. *Macromolecules* **1996**, 29, (17), 5590-5598.
61. Sollogoub, C. Structuration de systèmes polymères multiphasés en vue de matériaux à propriétés spécifiques et améliorées. UPMC, Paris, **2015**.
62. Schrenk, W., Method for multilayer coextrusion. In Google Patents: **1973**.
63. Tollar, J. E., Interfacial surface generator. In Google Patents: **1966**.
64. Alfrey, T.; Gurnee, E. F.; Schrenk, W. J., Physical optics of iridescent multilayered plastic films. *Polymer Engineering & Science* **1969**, 9, (6), 400-404.
65. Ma, M.; Im, J.; Hiltner, A.; Baer, E., Fatigue crack propagation in microlayer composites of polycarbonate and poly(styrene-acrylonitrile). *Journal of Applied Polymer Science* **1990**, 40, (5-6), 669-684.
66. Ma, M.; Vijayan, K.; Hiltner, A.; Baer, E.; Im, J., Thickness effects in microlayer composites of polycarbonate and poly(styrene-acrylonitrile). *Journal of Materials Science* **1990**, 25, (4), 2039-2046.
67. Pan, S. J.; Im, J.; Hill, M. J.; Keller, A.; Hiltner, A.; Baer, E., Structure of ultrathin polyethylene layers in multilayer films. *Journal of Polymer Science Part B: Polymer Physics* **1990**, 28, (7), 1105-1119.
68. Jin, Y.; Rogunova, M.; Hiltner, A.; Baer, E.; Nowacki, R.; Galeski, A.; Piorkowska, E., Structure of polypropylene crystallized in confined nanolayers. *Journal of Polymer Science Part B-Polymer Physics* **2004**, 42, (18), 3380-3396.
69. Bernal-Lara, T. E.; Liu, R. Y. F.; Hiltner, A.; Baer, E., Structure and thermal stability of polyethylene nanolayers. *Polymer* **2005**, 46, (9), 3043-3055.
70. Hu, Y. S.; Prattipati, V.; Mehta, S.; Schiraldi, D. A.; Hiltner, A.; Baer, E., Improving gas barrier of PET by blending with aromatic polyamides. *Polymer* **2005**, 46, (8), 2685-2698.
71. Carr, J. M.; Langhe, D. S.; Ponting, M. T.; Hiltner, A.; Baer, E., Confined crystallization in polymer nanolayered films: A review. *Journal of Materials Research* **2012**, 27, (10), 1326-1350.
72. Wang, H. P.; Keum, J. K.; Hiltner, A.; Baer, E.; Freeman, B.; Rozanski, A.; Galeski, A., Confined Crystallization of Polyethylene Oxide in Nanolayer Assemblies. *Science* **2009**, 323, (5915), 757-760.
73. Liu, R. Y. F.; Jin, Y.; Hiltner, A.; Baer, E., Probing Nanoscale Polymer Interactions by Forced-Assembly. *Macromolecular Rapid Communications* **2003**, 24, (16), 943-948.
74. Liu, R. Y. F.; Ranade, A. P.; Wang, H. P.; Bernal-Lara, T. E.; Hiltner, A.; Baer, E., Forced assembly of polymer nanolayers thinner than the interphase. *Macromolecules* **2005**, 38, (26), 10721-10727.
75. Liu, R. Y. F.; Bernal-Lara, T. E.; Hiltner, A.; Baer, E., Polymer interphase materials by forced assembly. *Macromolecules* **2005**, 38, (11), 4819-4827.
76. Arabeche, K.; Delbreilh, L.; Saiter, J. M.; Michler, G. H.; Adhikari, R.; Baer, E., Fragility and molecular mobility in micro-and nano-layered PC/PMMA films. *Polymer* **2014**, 55, (6), 1546-1551.
77. Mackey, M.; Flandin, L.; Hiltner, A.; Baer, E., Confined crystallization of PVDF and a PVDF-TFE copolymer in nanolayered films. *Journal of Polymer Science Part B: Polymer Physics* **2011**, 49, (24), 1750-1761.
78. Ponting, M.; Burt, T. M.; Korley, L. T. J.; Andrews, J.; Hiltner, A.; Baer, E., Gradient Multilayer Films by Forced Assembly Coextrusion. *Industrial & Engineering Chemistry Research* **2010**, 49, (23), 12111-12118.
79. Wang, J.; Langhe, D.; Ponting, M.; Wnek, G. E.; Korley, L. T. J.; Baer, E., Manufacturing of polymer continuous nanofibers using a novel co-extrusion and multiplication technique. *Polymer* **2014**, 55, (2), 673-685.
80. Rahman, M. A.; Wang, J.; Zhang, C.; Olah, A.; Baer, E., Novel micro-/nano- porous cellular membranes by forced assembly co-extrusion technology. *European Polymer Journal* **2016**, 83, 99-113.
81. Israelachvili, J. N., 17 - Adhesion and Wetting Phenomena. In *Intermolecular and Surface Forces (Third Edition)*, Academic Press: San Diego, **2011**, pp 415-467.
82. Cassie, A. B. D.; Baxter, S., Wettability of porous surfaces. *Transactions of the Faraday Society* **1944**, 40, (0), 546-551.
83. Wenzel, R. N., resistance of solid surfaces to wetting by water, *Industrial & Engineering Chemistry* **1936**, 28, (8), 988-994.

84. Quéré, D., Wetting and Roughness. *Annual Review of Materials Research* **2008**, 38, (1), 71-99.
85. Reyssat, M.; Yeomans, J. M.; Quéré, D., Impalement of fakir drops. *EPL (Europhysics Letters)* **2008**, 81, (2), 26006.
86. Wyart, F. B.; Martin, P.; Redon, C., Liquid-Liquid Dewetting. *Langmuir* **1993**, 9, (12), 3682-3690.
87. Reiter, G., Dewetting of thin Polymer Films. *Physical Review Letters* **1992**, 68, (1), 75-78.
88. Krausch, G., Dewetting at the interface between two immiscible polymers. *Journal of Physics-Condensed Matter* **1997**, 9, (37), 7741-7752.
89. Qu, S.; Clarke, C. J.; Liu, Y.; Rafailovich, M. H.; Sokolov, J.; Phelan, K. C.; Krausch, G., Dewetting dynamics at a polymer-polymer interface. *Macromolecules* **1997**, 30, (12), 3640-3645.
90. Wang, C.; Krausch, G.; Geoghegan, M., Dewetting at a polymer-polymer interface: Film thickness dependence. *Langmuir* **2001**, 17, (20), 6269-6274.
91. Lambooy, P.; Phelan, K. C.; Haugg, O.; Krausch, G., Dewetting at the Liquid-Liquid Interface. *Physical Review Letters* **1996**, 76, (7), 1110-1113.
92. de Silva, J. P.; Geoghegan, M.; Higgins, A. M.; Krausch, G.; David, M. O.; Reiter, G., Switching layer stability in a polymer bilayer by thickness variation. *Physical Review Letters* **2007**, 98, (26), 4.
93. Okerberg, B. C.; Berry, B. C.; Garvey, T. R.; Douglas, J. F.; Karim, A.; Soles, C. L., Competition between crystallization and dewetting fronts in thin polymer films. *Soft Matter* **2009**, 5, (3), 562-567.
94. Zhu, Y.; Bironeau, A.; Restagno, F.; Sollogoub, C.; Miquelard-Garnier, G., Kinetics of thin polymer film rupture: model experiments for a better understanding of layer breakups in the multilayer coextrusion process. *Polymer* **2016**, 90, 156-164.
95. Antonios, G. M.; Nikolaos, A. P., Polymer chain entanglements and brittle fracture. *The Journal of Chemical Physics* **1988**, 88, (2), 1337-1342.
96. Brown, H. R., Effect of a diblock copolymer on the adhesion between incompatible polymers. *Macromolecules* **1989**, 22, (6), 2859-2860.
97. Brown, H. R.; Char, K.; Deline, V. R.; Green, P. F., Effects of a diblock copolymer on adhesion between immiscible polymers. 1. Polystyrene (PS)-PMMA copolymer between PS and PMMA. *Macromolecules* **1993**, 26, (16), 4155-4163.
98. Anastasiadis, S. H.; Russell, T. P.; Satija, S. K.; Majkrzak, C. F., Neutron reflectivity studies of the surface-induced ordering of diblock copolymer films. *Physical Review Letters* **1989**, 62, (16), 1852-1855.
99. Creton, C.; Kramer, E. J.; Hui, C. Y.; Brown, H. R., Failure mechanisms of polymer interfaces reinforced with block copolymers. *Macromolecules* **1992**, 25, (12), 3075-3088.
100. Dai, K. H.; Norton, L. J.; Kramer, E. J., Equilibrium Segment Density Distribution of a Diblock Copolymer Segregated to the Polymer/Polymer Interface. *Macromolecules* **1994**, 27, (7), 1949-1956.
101. Brown, H. R., A molecular interpretation of the toughness of glassy polymers. *Macromolecules* **1991**, 24, (10), 2752-2756.
102. Johnson, K. L.; Kendall, K.; Roberts, A. D., Surface Energy and the Contact of Elastic Solids. *Proceedings of the Royal Society of London. A. Mathematical and Physical Sciences* **1971**, 324, (1558), 301-313.
103. Deruelle, M.; Leger, L.; Tirrell, M., Adhesion at the Solid-Elastomer Interface: Influence of the Interfacial Chains. *Macromolecules* **1995**, 28, (22), 7419-7428.
104. Barthel, E., Adhesive elastic contacts: JKR and more. *Journal of Physics D: Applied Physics* **2008**, 41, (16), 163001.
105. Fuller, K. N. G.; Tabor, D., The Effect of Surface Roughness on the Adhesion of Elastic Solids. *Proceedings of the Royal Society of London. A. Mathematical and Physical Sciences* **1975**, 345, (1642), 327-342.
106. Crosby, A. J.; Hageman, M.; Duncan, A., Controlling Polymer Adhesion with "Pancakes". *Langmuir* **2005**, 21, (25), 11738-11743.
107. Lamblet, M.; Verneuil, E.; Vilmin, T.; Buguin, A.; Silberzan, P.; Léger, L., Adhesion Enhancement through Micropatterning at Polydimethylsiloxane-Acrylic Adhesive Interfaces. *Langmuir* **2007**, 23, (13), 6966-6974.

Chapter 2

Towards an understanding of layer breakup phenomenon in nanolayer coextrusion: existence of a critical thickness in nanolayered films

(the first part of this chapter is mainly based on an article recently submitted to Macromolecules, reference ³¹ in the following, while the second part is based on an article published in Polymer, reference ⁵⁴ in the following. The whole chapter is based on results obtained during Adrien Bironeau's PhD work, reference ²⁹, which he defended in December 2016)

2.1. Aim of the study

As was discussed briefly in the previous chapter, nanostructured polymeric materials have shown unique properties arising from the combination of multi-scale assembly, geometrical confinement and interfacial effects.¹ The aim of current research activities is thus to develop new strategies to design such nanostructured materials with controlled architecture. In particular, nanolayered (or nanolaminated) structures have received significant attention due to their outstanding mechanical properties observed in natural biological systems like nacre.² To fabricate polymer-polymer nanolayered films, different strategies have been reported. A first one, based on a bottom-up approach, consists in non-covalent association of ultra-thin polymer films using molecular self-assembly as a fabrication tool.³ However, those techniques suffer mainly from low productivity. Another strategy, that could be assimilated to a top-down approach, consists in using industrial processes, slightly modified or optimized in order to better control the structure down to the nano-scale.⁴ One of those structuring processes is the nanolayer coextrusion process which we introduced along with its numerous potentialities in the previous chapter.

However, in some studies it has been observed that below a certain layer thickness for a given polymer pair, the layers tend to lose their integrity, *i.e.* break spontaneously during the process. This breakup phenomenon was observed with different polymer pairs and the layer-continuity limit appeared to be somewhat system-dependent: for example, 5-nm thick continuous layers were obtained for polycarbonate (PC) and poly(methyl methacrylate) (PMMA),⁵ but nothing thinner than 25 nm has been reported for polypropylene (PP) and polystyrene (PS).⁶ Worse, only layers thicker than 500 nm could be achieved for PP and PC.⁷

It is clear that the destruction of the nanolayered structure can have severe consequences and strongly limits the potentiality of this innovative process. In particular, it may alter the final properties, as observed by Lin et al.⁸ who have shown a barrier-property loss for polypropylene (PP) / polyethylene oxide (PEO) nanolayer films attributed to layer breakup, occurring when the PEO layer thickness was reduced below 25 nm. It seems therefore of prime importance to better understand the mechanisms governing these layer breakup in order to achieve a well-controlled route towards the design of new nanolayered polymeric materials with enhanced properties. Still, a comprehensive study of the conditions of apparition of these layer breakups at the nanoscale, as well as the physical mechanisms governing them, is lacking in the literature.

Nevertheless, some studies dealing with interfacial distortions or instabilities in coextrusion or the rupture of polymer thin films may shed new light on the nanolayer breakup phenomenon. It may be indeed the consequence of interfacial distortions (viscous encapsulation or secondary flows), mainly encountered when

rheologically mismatched polymers are coextruded^{9, 10} as observed in classical coextrusion. To get rid of these distortions, viscosity and elasticity matching has been a basic rule in coextrusion for a long time.¹¹ Similarly, instabilities initiated by a small perturbation at the interfaces of coextruded polymers that may be eventually amplified along the flow in the die,¹²⁻¹⁴ can also induce layer ruptures - especially when the layer thickness is small. If the origin of the initial perturbation is scarcely discussed in the literature, the parameters governing the amplification of the instability have been identified: elastic and viscosity jumps at interfaces.¹⁵⁻¹⁷

Film ruptures quite similar to those obtained in nanolayer coextrusion have been observed by Macosko's group,¹⁸⁻²⁰ when looking at the morphological development of polymer blends in industrial processes: during the initial stage, softened pellets are stretched and thin polymer sheets are created, that break up through hole formation ("sheeting mechanism"). Still, no precise mechanism is proposed for those film breakups and, in some cases, "Rayleigh instabilities" are erroneously invoked despite their fundamentally different – axisymmetric – origin.²¹

Finally, as was summarized in chapter 1, many studies deal with the dewetting of polymer thin films deposited on solid or immiscible polymer substrates (i.e. when the spreading parameter is negative) in "static" conditions (no shear or elongational flows applied).²²⁻²⁴ It can be observed for example on thin PS films deposited on PMMA and heated well above the glass-transition temperature T_g .²⁵ As we recall from chapter 1, at a molecular level, for films presenting very low thicknesses (< 100 nm), different dewetting routes have been proposed depending on whether the initiation is extrinsic or intrinsic. In the first mechanism, termed nucleation, the presence of nuclei, such as dust particles or surface heterogeneities, triggers topographical defects that will grow into holes. In the second route, called spinodal dewetting by analogy with spinodal decomposition of binary mixtures,^{24, 26} the mechanism has been proposed by Vrij²⁷ and Sheludko.²⁸ thermal fluctuations destabilize the interface and the perturbation can be amplified, if this reduces the system's free energy, leading to the film rupture. Essentially, two ingredients of common – van der Waals – origin are present in this free energy: capillarity, which tends to smoothen and stabilize the interface, and disjoining interactions, acting on distances up to about 100 nm, and which are, depending on the system (nature of the polymer and its environment) either stabilizing or destabilizing.

As a consequence, the aim of the present study is twofold: first, to track the layer breakups when reducing the individual layer thickness in the nanolayer coextrusion process and to determine whether, for a given polymer pair, a critical layer thickness, i.e. a thickness below which layers break, can be defined; secondly, to examine and discuss possible mechanisms of layer breakup. The effects of process and material parameters on layer continuity are thus investigated. In the second part of this chapter, we will present first attempts at developing model experiments to confirm the results and hypotheses of the first part.

2.2. Nanolayered coextruded films: production and characterization

To avoid crystallization effects and interfacial diffusion, an immiscible glassy polymer pair, PMMA and PS, has been chosen. PMMA/PS nanolayered films are produced using a multilayer coextrusion process. PMMA was supplied by Altuglas International (Arkema) and is commercially available as Altuglas VM100 (Mass average molar mass $M_w = 139 \text{ kg}\cdot\text{mol}^{-1}$, dispersity $D_M = 2.1$, density at 25 °C = 1.18 g/cm³, density at 200 °C = 1.08 g/cm³). PS, commercially available as Crystal 1340, was provided by Total Petrochemical ($M_w = 245 \text{ kg}\cdot\text{mol}^{-1}$, $D_M = 2.2$, density at 25°C = 1.05 g/cm³, density at 200 °C = 0.96 g/cm³). The two polymers have been selected to

have a viscosity ratio ($\eta_{\text{PMMA}} / \eta_{\text{PS}}$) close to one (measured between 0.6 and 0.8) at the extrusion temperature (225 °C) and in the shear-rate range of the coextrusion process, typically between 1 and 10 s⁻¹. These two materials showed an elasticity ratio ($G'_{\text{PMMA}} / G'_{\text{PS}}$) between 0.2 and 0.5, i.e. also relatively close to 1. Uniaxial extension tests showed that both polymers have a similar behavior under elongation, typical of linear polymers. More experimental details can be found in the PhD thesis of Adrien Bironeau.²⁹

The multilayer coextrusion is composed of two 20-mm single-screw extruders, two melt-gear pumps, a three-layer (A-B-A) coextrusion feedblock, a layer-multiplying element (LME) assembly, an exit flat die and a thermally regulated chill roll. A schematic illustration is shown in Figure 1. The temperature of feed-block and LME is set to 225 °C. Gear pumps enable a control over the relative composition ratio of the two melt streams that are combined in the A-B-A feedblock. From the feedblock, the initial three-layer flow through a sequence of LME. A series of N elements leads to a film composed of $2^{N+1} + 1$ alternating layers, as shown in Figure 1. Here, 10 to 13 LME are used, giving films containing 2049, 4097, 8193 and 16385 layers, respectively. Finally, after passing through the last layer-multiplying element, the melt goes through a flat die, 150 mm wide and 2 mm thick. The exit die temperature is fixed to 200°C. At the die exit, the layered samples were stretched and quenched, using a water-cooled chill roll at a temperature of 95°C, and collected at different drawing speeds. In some cases, two sacrificial polyethylene (PE) skin layers were laminated at the die exit on both sides of the multilayer film, allowing for a reduction of the total film thickness without stretching.

Starting from an A-B-A initial configuration, the expected individual layer thickness of polymer B which will be named nominal thickness (h_{nom}) in the manuscript, can be calculated using:

$$h_{\text{nomB}} = h_{\text{film}} \frac{\Phi_{\text{B}}}{n_{\text{B}}} \quad (\text{Eq. 1})$$

with h_{film} the total film thickness, Φ_{B} the volume fraction of polymer B in the film (determined via the weight compositions and densities at extrusion temperature), $n_{\text{B}} = 2^N$ the number of B layers. The equation works similarly for polymer A (with Φ_{A} and $n_{\text{A}} = 2^N + 1$).

Looking at Equation (1), it appears that different ways are possible in order to decrease the individual layer thickness: increase the number of LME (which will increase the number of layers without changing the total film thickness), or decrease the total film thickness or relative composition. The draw ratio (Dr) is defined as the roll take-off speed divided by the mean flow speed at the exit die. Hence, increasing Dr and/or adding a skin layer (removed prior to characterization) reduces the total film thickness, i.e. decreases the nominal thickness at given number of layers and composition (Dr being inversely proportional to the total thickness of the films). Volume composition is adjusted through the gear-pumps speed. The weight compositions (wt%) of the multilayered PMMA/PS films studied are: 95/5, 90/10, 50/50, 10/90 and 5/95.

The total film thickness ranges from 3000 to 80 μm and the nominal PS and PMMA layer thicknesses were varied from 936 nm down to 2 nm and from 822 nm down to 2 nm, respectively.

Atomic force microscopy (AFM) is used to determine the layer thicknesses, as well as the integrity and uniformity of the films. Experimental details concerning the preparation of the samples can be found in reference x. AFM images are taken in the extrusion direction (see Figure 2). The layer thicknesses are measured from the AFM phase images that most clearly revealed the layered structure with sharp interfaces. On the obtained images, PS and PMMA appear in brown and gold color, respectively. For all the samples in the study, more than 200 layers were measured.

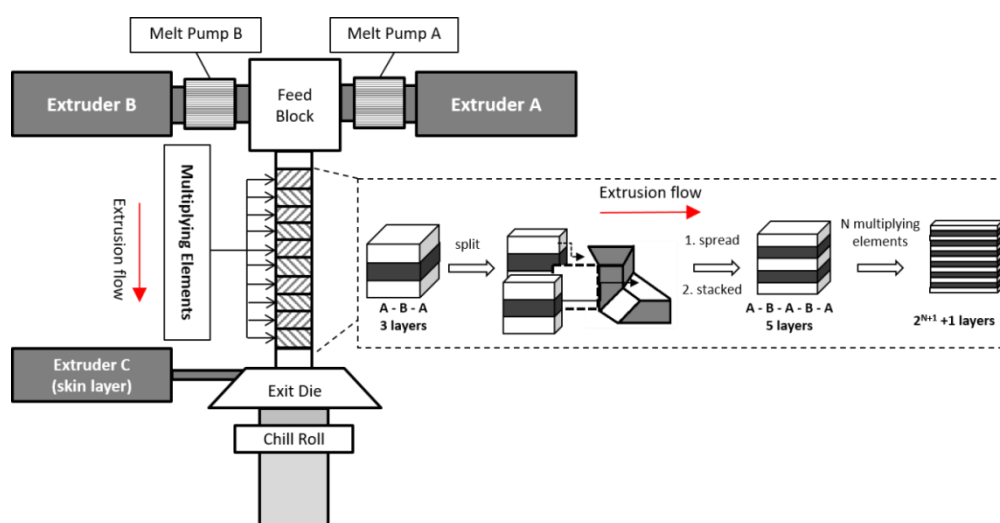


Figure 1: Principle of the multiplication of layers by the multilayer coextrusion process.

The layer thicknesses are measured using the AFM phase images and the image analysis software Gwyddion (see experimental details in references x and y). Based on all the measured thicknesses, it was possible to obtain statistical information which is then used to compare different experimental conditions. The quantities of interest are: the mean thickness (h_{mean}) and the thickness distribution (both determined only from the continuous layers) and the percentage of broken layers. The latter is defined as the number of observed broken layers divided by the total number of observed layers.

As layer thickness is expected to be in the range of tens of nanometers, *i.e.* a few pixels in terms of AFM imaging, it is critical to analyze all possible sources of error. These sources of error were studied extensively in a recent article³⁰ which determined the relative uncertainty ϵ_{rel} of the thickness measurement due to sampling for each film, varying between 5% and 30%.

2.3. Existence of a critical thickness for PS/PMMA nanolayered films

As showed in Equation 1, different processing routes are possible in order to achieve a desired final thickness. Figure 2a shows the effects of Dr and composition (weight ratio) on the thickness of the continuous PS layers, keeping the number of layers constant. Conversely, Figure 2b illustrates the effects of Dr and the number of LME keeping the composition constant. As expected, a decrease in layer thickness is observed when decreasing the total film thickness, increasing the number of LME or decreasing the fraction of PS. Figure 2 also shows that for layer thicknesses over 20 nm, the experimentally measured value matches almost perfectly the targeted (nominal) one. However, whatever the processing conditions, the measured thicknesses deviate strongly from the nominal ones, for layer thicknesses below 20 nm. Moreover, no (mean) experimental value below 12 nm is measured, which suggests the existence of a fundamental lower bound for the achievable PS layer thickness obtained via nanolayer coextrusion of PS/PMMA. Same trends were observed for PMMA layers (data not shown, see reference³¹).

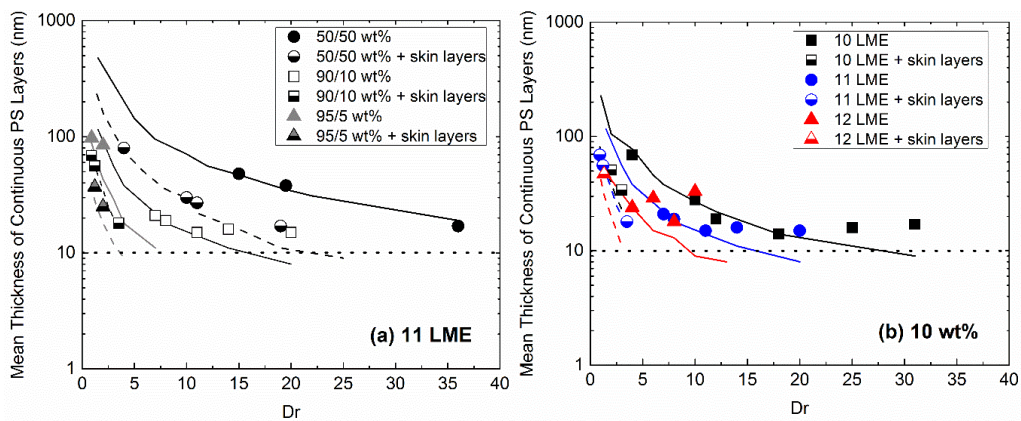


Figure 2: Mean thickness of continuous PS layers as a function of draw ratio: (a) with 11 LME and at different compositions; (b) with different numbers of LME and at fixed composition (10 wt%). Lines (solid and dashed) correspond to the nominal thickness for the associated conditions, while symbols are measured mean values. Dashed lines indicate the presence of skin layers. The horizontal dotted line indicates a mean thickness of 10 nm. For clarity reasons, the standard deviations are not represented.

In addition, the percentage of broken PS layers for different Dr is measured and represented in Figure 3a. As stated above, different processing routes can be chosen to reach thicknesses in the 10-nm range: high stretching at the exit die, or high number of LME that may be coupled with a low proportion of the confined polymer and/or the addition of two skin layers. It appears that, regardless of the composition and the number of LME, the layers become more and more discontinuous as Dr is increased, i.e. as the film thickness decreases. This result could account for a possible tendency of layers to breakup because of stretching. However, some conditions (high number of LME and/or low volume fraction of one of the polymers) lead to a high percentage (> 50%) of broken layers at low or moderate Dr (grey area in Figure 3a). As a consequence the film stretching induced by the chill roll is not the only step responsible for the layer breakup.

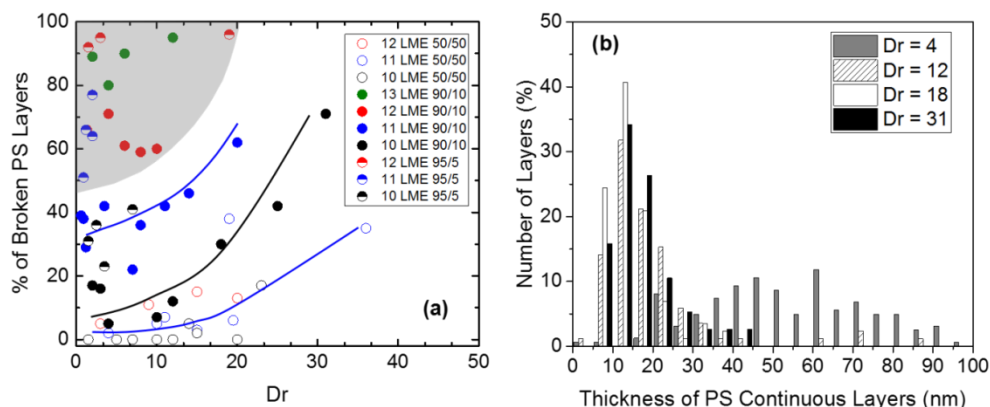


Figure 3: (a) Percentage of broken PS layers as a function of draw ratio for different numbers of LME and compositions; the color lines are guides to the eye; the grey area indicates a high percentage of broken layers at low draw ratio (b) Distribution of PS layer thickness for different draw ratios for a sample containing 10 wt% of PS, and with 10 LME (corresponding to the black circles in Figure 4a).

To study more closely the link between the amount of broken layers and the mean thickness, the statistical thickness distribution was built for different Dr. Figure 3b displays this statistical distribution for 10 wt% of PS using 10 LME with Dr ranging from 4 to 31. As already pointed out in Figure 3 for the mean thickness, we observe that the distribution shifts to lower thicknesses when increasing the draw ratio, while the distributions are narrower. As Dr increases from 4 to 18, the mean thickness decreases from 69 nm to 14 nm while the standard deviation decreases from 50 nm to 6 nm (i.e. the coefficient of variation decreases from 0.73 to 0.45). We observe as well that the distribution loses its symmetry and becomes truncated at low thickness values. However, at high Dr (Dr =31), the mean thicknesses and standard deviation start to increase again (17 nm and 8 nm respectively). This is correlated to an increase in the percentage of broken layers (see Figure 3a).

Combining all the collected data, two master curves can be plotted as a function of the nominal thickness: the mean experimental thickness (Figure 4a), and the percentage of broken layers (Figure 4b). We chose not to plot the mean thickness when the associated percentage of broken layers is higher than 80%. These master curves allow representing the results for all the processing routes and reveal three distinct regions. In the first one, for nominal layer thicknesses superior to 40 nm, continuous layers are robustly obtained throughout the film (percentage of broken layers lower than 10 %) following different processing routes and a good match between nominal and measured layer thicknesses is achieved. In the second one, for nominal layer thicknesses between 10 and 40 nm, all the processing routes are not equivalent and a deviation between the experimental layer thicknesses and the nominal values may occur. Simultaneously, the percentage of broken layers increases. Still, for some optimized processing conditions, the deviations from nominal values remain small and might even be negligible as well as the percentage of broken layers. However, in the third region, for nominal layer thicknesses lower than 10 nm, deviations from the nominal values become significant, the measured value being systematically higher than the nominal one, independently of the processing conditions. These deviations are associated with an important percentage of broken layers, higher than 60 % for nominal thicknesses below 10 nm.

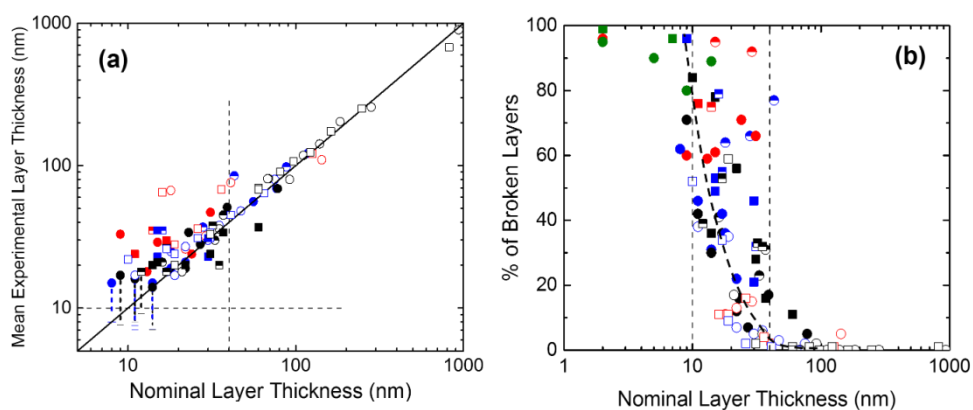


Figure 4: (a) Mean experimental layer thickness, and (b) percentage of broken layers, as a function of nominal layer thickness, for all processing conditions: PS (circles), PMMA (squares), 13 LME (green), 12 LME (red), 11 LME (blue), 10 LME (black), 50/50 wt% (empty), 90/10 wt% (full), 95/5 wt% (half). The thin solid line in Figure 5a is the 1-1 expectation (i.e. $h_{nom} = h_{mean}$), while the thick dashed line in Figure 5b is only a guide to the eye. The regions are delimited by horizontal and vertical thin dashed lines at 10 and 40 nm. The thinnest individual layers measured are indicated through the vertical dotted bars.

Those results confirm once again the existence of a fundamental critical layer thickness below which the layers break up. Specifically, the thinnest layers observed have a thickness of 7 nm (see minimal values plotted in Figure 4a). Looking at a whole sample, no mean thickness lower than 12 nm could be achieved. It is then reasonable to define a critical thickness h_c at around 10 nm for the PS/PMMA system, this critical thickness is obtained independently of the confined polymer, PS or PMMA.

2.4. Critical thickness and possible mechanisms for the layer breakup

A first basic idea would be that an intrinsic critical thickness should be related to the size of the macromolecules. Indeed, using Kuhn length values from Fetters,³² one can estimate for the PS used in this study, an average end-to-end radius $R_{PS} \approx 33$ nm, and $R_{PMMA} \approx 23$ nm for PMMA. This is in both cases similar (though slightly bigger) to the observed critical thickness ($h_c \sim 10$ nm). However, this is assuming a random coil conformation, which is certainly not the case for stretched films ($Dr > 1$) because of the simultaneous drawing and non-uniform cooling of the films at the end of the extruders, leading to different elongated states for the chains among the layers (more elongated near the surface, more relaxed at the center). It should also be noted that stable PS nanolayers much thinner than the radius of gyration can be relatively easily obtained using other techniques, such as spin-coating, even with higher molecular weights.

Let us then discuss in further details the possible mechanisms mentioned in the introduction for the layer breakup in the nanolayer coextrusion process. Instabilities occurring during classical coextrusion (i.e. at the micron scale) have been, as summarized above, widely studied in the literature. In the present study, in order to avoid viscoelastic interfacial distortions or instabilities, rheologically matched PS and PMMA have been chosen. This rheological matching ensures stable flow and flat (at the microscopic scale) interfaces even for submicronic layers, as it was observed in this study: nearly 0 % of broken layers can be achieved for mean layer thicknesses as low as 30 nm with well-chosen experimental conditions (see Figure 4b). This suggests that these mechanisms cannot alone justify what happens for thicknesses below these values.

We then go back to the mechanism responsible for the spinodal dewetting of ultra-thin (< 100 nm) polymer films. In the nanolayered coextruded films, disjoining forces that act on distances up to 100 nm cannot be neglected. When considering two layers of a given polymer (for example PMMA) surrounding a thin layer of another polymer (for example PS), the disjoining forces are attractive and can destabilize the two interfaces.

Following Sheludko,²⁸ the critical condition for the film rupture can be derived by balancing two opposite forces: the stabilizing capillary force and the destabilizing disjoining force. The disjoining pressure due to the intermolecular forces (see chapter 1) is given by³³:

$$\pi_{vdW} = \frac{-A_H}{6\pi h^3} \quad (\text{Eq. 2})$$

where A_H is the Hamaker constant.

The capillary force can be described through the local Laplace pressure developed in the concavity of the disturbed interface:

$$P_c \sim \gamma h'' \sim \frac{\gamma a}{\lambda^2} \quad (\text{Eq. 3})$$

where γ is the interfacial tension, h the thickness of the film, a the amplitude of the instability and λ its characteristic wavelength; and where the prime denotes the spatial derivative along one orthogonal direction to the film.

Balancing Equations (2) and (3), and assuming the rupture to occur when $a \sim h_c/2$, we obtain:

$$h_c \sim \left(\frac{A_H \lambda^2}{3\pi\gamma} \right)^{1/4} \quad (\text{Eq. 4})$$

The characteristic wavelength λ remains an undetermined parameter, but can be chosen as the thickness of the film, as a first estimate. In this case, Equation (4) becomes:

$$h_c \sim \left(\frac{A_H}{3\pi\gamma} \right)^{1/2} \quad (\text{Eq. 5})$$

A refined approach is to use for λ the wavelength of the thermal fluctuations, which can be approximated by $(kT/\gamma)^{1/2}$.³⁴ This leads to:

$$h_c \sim \left(\frac{A_H kT}{3\pi\gamma^2} \right)^{1/4} \quad (\text{Eq. 5 bis})$$

In such a mechanism, the layer breakup occurs spontaneously, without any energy barrier. However, it may take a long time, depending on layer thickness: the thicker the films, the weaker the driving force and the longer the breaking time. When the critical thickness is reached, a characteristic rupture time of the film can be derived by balancing the viscous stress and the disjoining pressure:

$$\tau \sim \frac{\eta}{\pi v d W} = \frac{6\pi\eta h_c^3}{A_H} \quad (\text{Eq. 6})$$

To estimate a critical thickness for our PS/PMMA system from Equation (5), we have to evaluate the Hamaker constant, which is not an easy task, especially in stratified systems where many mutual interactions may have to be considered. Nevertheless, some values can be found in the literature for PS/PMMA bilayer systems deposited on a solid substrate: they cover a few orders of magnitude, between 10^{-18} and 10^{-21} J, depending on the method used and the environment.^{35, 36} Considering the value proposed by de Silva et al. for a PS/PMMA/PS trilayer system,³⁶ $A_H \text{ PS/PMMA/PS} = 2.10^{-18}$ J (which should be the same value for a PMMA/PS/PMMA system based on Lifshitz theory³³), we obtain $h_c \sim 14$ nm using Equation (5), and $h_c \sim 6$ nm using Equation (5 bis), which are in good agreement with our experimental findings (Figure 5). If lower values of the Hamaker constant are considered, the critical thickness reaches smaller values, down to ~ 2 nm. For our experimental estimate, $h_c \sim 10$ nm, the characteristic rupture time calculated from Equation (6) is less than 1 s, which is much less than the processing time (the total mean residence time being around 1 minute). Those estimated critical values confirm that a layer breakup due to interfacial fluctuations amplified by disjoining forces is a realistic scenario in order to explain the experimental results.

Figure 4 shows as well that depending on the processing routes, when the nominal thickness is comprised between 10 and 40 nm, the layer breakup can considerably increase. First, this can be explained by the fact that, when the thickness distribution is large, some layers will reach the critical thickness and consequently break even if the mean thickness is higher than the critical thickness. Secondly, the 10-40 nm thickness range

can be considered as a transition region from a capillary-dominated regime to a disjoining-dominated one. Finally, we note that due to the expected presence of impurities in such a semi-industrial process, it is probable that nucleated dewetting occurs at higher thicknesses than the spinodal critical one.

2.5. Comparison with literature data

The breakup phenomenon in nanolayer coextrusion was also observed with different polymer pairs and appears at different critical thicknesses, as indicated in Table 1. It is important to note that in these previous works no systematic study has been performed in order to ensure that the critical thickness values were independent of the processing conditions. Nevertheless, it is possible to consider such values as critical thicknesses for the considered pairs. Except for PP/PC (the critical thickness value of which may be the result of far-from-optimized processing conditions), all polymer pairs studied lead to similar critical thicknesses, in between 5 and 25 nm.

In our proposed scenario for rupture, the critical thickness is set by the Hamaker constant and the interfacial tension. As stated by Israelachvili,³³ the Hamaker constants of most condensed systems have similar values, and for most polymeric systems should lie in the range 10^{-21} - 10^{-18} J. Moreover, the values of this constant are not easily found in the literature and can cover the same range for a given pair, as discussed previously for the PS/PMMA system. Similar conclusions can be drawn about most polymer-polymer interfacial tensions: for any given polymer pair, the interfacial tension should lie in the 0.5-5 mJ/m² range.³⁷

Polymer pair	Confined polymer	Minimal layer thickness (nm)	Interaction parameter	Interfacial tension (mJ/m ²)	Interfacial toughness (J/m ²)
PS / PMMA	PS	7	0.036 at 225 °C ³⁸	0.55 ³⁹ ; 0,56 ⁴⁰ at 225 °C	45 ⁴¹ (multilayer); 12 ⁴² ; 4-12 ⁴³ (multilayer)
	PMMA	10			
PP / PC	PP	500 ⁷	-	-	-
PC / PMMA	PC	12 ⁴⁴	0.039 at 250 °C ⁴⁵ ; 0.017 ⁴⁶	1.44 at 240 °C ⁴⁷	1000 ⁴⁸ (multilayer)
	PMMA	5 ⁵			
HDPE / PS	HDPE	10 ⁴⁹	-	4 ^a	10 ⁵⁰
PC / PET	PET	10 ⁵¹	-	-	21 ⁵⁰
PP / PEO	PEO	25 ⁸	-	-	-
PP / PS	PP	25 ⁶	-	1.4 - 4 at 215 °C ⁵²	0 ⁵⁰
	PS	25 ⁶			

^a: extrapolated with linear fit from ⁴⁰

Table 1: Molecular characteristics and critical layer thickness for polymer-polymer nanolayered coextruded films.

Thus, from Equations (6, 6bis) we conclude that the critical thickness should be similar for most polymer pairs and typically close to ~ 10 nm, in agreement with the literature results for amorphous polymeric systems summarized in Table 1. Interestingly, when semi-crystalline polymers are considered instead, the critical thickness appears to be slightly higher.⁸ This could reveal the side influence of other phenomena such as volumetric changes during crystallization upon cooling.

A final question is related to the compatibility of the polymer pair and the existence of an interphase which is not accounted for in the proposed mechanism. As discussed in chapter 1, one way to estimate the compatibility is through the (dimensionless) Flory-Huggins interaction parameter χ , which has been estimated or measured for several polymer pairs. χ is related to the size w of the interphase and to the interfacial tension, as recalled in chapter 1. Another quantity that encompasses the compatibility between immiscible polymers is the interfacial toughness. As can be seen from partial data that could be obtained in the literature for some polymer pairs (Table 1), no clear trend between these parameters and the critical thickness values can be deduced, which highlights the difficulty of defining a critical thickness when polymer pairs with diffuse interfaces are considered. Therefore, more work is needed in order to achieve a complete understanding of the role of compatibility on the interfacial instabilities occurring in nanolayered polymer flows.

2.6. Model experiments: presentation of the experimental set-up

To further test these hypotheses, simplified experiments on model systems containing a small number of layers have been proposed.

Bilayer systems (a thin PS film dewetting on a thicker PMMA layer, for example) have been extensively studied, as noted previously. However, a more representative experiment of what happens during the multilayer coextrusion would be the rupture of a polymer thin film within two thicker layers of another polymer, i.e. two polymer-polymer interfaces (instead of one polymer-polymer interface and one polymer-air interface). A first idealized experiment consists in studying the dewetting kinetics of such systems in “static” mode (no shear or elongation forces applied to the system), and compare it with the typical extrusion time. This trilayer system had not been studied in details, though one recent paper (mentioned earlier) dealt with the onset of the instabilities within a PS-PMMA-PS thin sandwich.³⁵ However, as mentioned by Brochard,²⁴ the kinetics itself should not be affected by the initial mechanism of hole formation (assuming the mechanism is similar to the one observed for a bilayer system). Actually, the closest experiments were those conducted by Reyssat and Quéré on the bursting of a water film within an oil bath, with the difference that in the polymer-polymer case viscosities are both very high and may also be of similar values.⁵³

In consequence, we developed an experimental setup allowing the rupture kinetics of trilayers systems (thin PS in between two thicker PMMA layers) to be followed. The setup was first validated by using it on bilayers systems. These results will not be detailed here and the reader can refer to⁵⁴. Briefly, the trilayer systems are put in a Mettler FP80 heating stage already set at the chosen temperature (180 °C, 200 °C or 225 °C) under an Olympus BH-2 optical microscope with a 10x magnification (or 20x magnification for the thinner films or the higher temperatures) (see figure 5). Note that with this setup, the instabilities are observed from the top, while the AFM observations on multilayer films are made in the extrusion direction. After the focus is made manually (which takes between 30 s and 1 mn), images are taken at regular times depending on the speed of the experiment (depending on the experimental conditions, from a few minutes to a few hours to have

coalescence of the holes into droplets) to observe the appearance of holes in the PS and their growth over time. Contrary to many experimental set-up used in the literature (references^{25, 55} for example) and since we were not interested in this first study in probing the shape of the rim, the setup chosen here enabled to follow in situ the dewetting, without quenching of the sample (which can lead to possible issues in the data analysis due for example to non-constant viscosity while heating and then quenching).

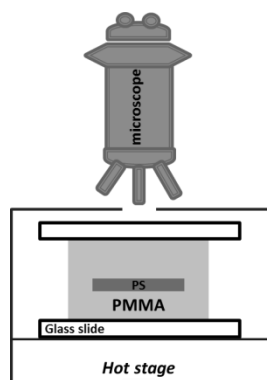


Figure 5: schematic of the experiment for a “trilayer” system.

To prepare the trilayer systems, the same PS and PMMA than presented in section 2.2. have been used. Another more viscous grade, PMMA V825T was also used in this study. The complex viscosity obtained at different temperatures on an Anton Paar rheometer with a frequency sweep test, are summarized in table 2 below.

	M_w (kg/mol)	PDI	T = 180 °C	T = 200 °C	T = 225 °C
			η_0 (Pa.s)	η_0 (Pa.s)	η_0 (Pa.s)
PS 1340	245	2.2	57000	11300	2540
PMMA VM100	139	2.1	72000	9800	1800
PMMA V825T	140	1.9	Not measured	56900	6300

Table 2: molar masses and rheological values for various temperatures of the polymers used in the study.

PMMA substrates were obtained via spin-coating (Spin 150 v-3 from SPS) of a PMMA solution in toluene (20 wt% for the VM100 and 15 wt% for the V825T) on a glass slide. The speed and acceleration were fixed to achieve a resulting thickness close to 3 μ m. The precise thickness was each time measured using a Veeco Profilometer (Dektak 150). Any possible impact of the roughness of the substrate on the dewetting was neglected in this study.⁵⁶ Complementary substrates with thicknesses close to 400 nm and 10 μ m were obtained by changing the solutions concentrations and spin-coating parameters. Thicker substrates (> 100 μ m)

were obtained using pellets put under a thermocompression press (Laboratory Press, Gibrite Instruments) set at 100 bar and 225 °C for 3 minutes.

PS thin films were prepared via spin-coating of PS solutions in toluene on a silicon wafer treated for 5 minutes in a UV-ozone chamber. By varying the concentration of PS in the toluene (from 1 to 4 wt%) and the speed of spin-coating (from 2000 to 3000 rpm) while keeping the acceleration constant (4000 r/s^2), three thicknesses were achieved and studied: 50 nm, 120 nm, and 260 nm. The exact thickness was for each sample controlled using an AFM (Veeco Nanoscope V) in tapping mode. In this first study, as such systems had not been dealt with in the literature, it seemed logical to start with thin films rather than ultra-thin films ($< 20 \text{ nm}$), so probably more in a case of nucleation and growth than spinodal dewetting discussed in the first part of this chapter.

After spin-coating, the films were cut in small pieces using a razor blade and then floated on a distilled water bath. No annealing was performed in the samples, similar to what was done in references ^{25, 55, 57}. The choice not to anneal the PS thin film (and neglecting the potential impact the kinetics of the instabilities growth) was based on the fact that after extrusion (especially the chill-roll step), polymer chains are also presumably strongly out of equilibrium in terms of conformation.

To prepare the bilayer systems, the PS film was then simply picked up on the PMMA substrate and let a few hours under open air to remove the remaining water. To prepare the trilayer systems, same procedure was applied. Then, another PMMA substrate on a glass slide was put on top of the bilayer and put at 150 °C for 2 minutes with a small force applied on top to ensure adhesion between the two PMMA without inducing significant flow of the polymers resulting in a change of thicknesses. At this temperature, it was verified that no dewetting of the PS occurs in this time scale (dewetting actually only occurs after more than 6 hours at 150 °C). Rather than a real trilayer system, this is actually more a PS thin film embedded in a PMMA matrix.

For each dewetting experiment, at least 5 images taken at different times were analyzed. On these images, the growth of at least 3 holes was followed. Holes were chosen so that there are no surrounding holes closer than typically the diameter of the hole: in consequence, the possible interactions between holes were neglected in the analysis. The final stage of the dewetting process (coalescence of the holes to form droplets) was not studied here. At least two samples were studied for each set of fixed parameters (namely temperature, PS and PMMA thicknesses). The inner diameter of the holes was then measured using the Olympus analysis software with a typical precision of $\pm 0.5 \mu\text{m}$.

2.7. First results: dewetting of thin PS films embedded in a PMMA matrix

The most famous case of film bursting is those of soap films suspended in air. In that case, a constant speed where capillary drive balances with inertia is expected and has been measured already almost 50 years ago.^{58, 59} More recent studies focused on free-standing polymer films where viscous effects are dominant.⁶⁰ For these systems, no rim at the edge of the holes can be observed, contrary to soap films, and the growth of a hole is exponential. When the film is made thinner or the temperature is lowered closer to T_g , elasticity becomes the dominant parameter and the growth is then linear.⁶¹ More relevant to our system is the case where a film bursts within a viscous environment.^{53, 62} In that case, the bursting proceeds also at a constant speed where capillary drive balances with viscous dissipation this time not in the film but inside the surrounding more

viscous phase. Then, the capillary force per unit length which draws the rim γ created is balanced with a viscous force. Treating the rim as a cylinder translating at a velocity v in a surrounding phase of viscosity η , the viscous force per unit length should scale as ηv .⁵³ This leads to a constant opening velocity v scaling as γ/η :

$$v \sim \gamma/\eta \quad (\text{Eq. 7})$$

and

$$R = vt \sim \gamma t / \eta \quad (\text{Eq. 8})$$

R being the radius of the hole considered.

In our case, the relevant parameters would then be the interfacial tension $\gamma_{PS/PMMA}$ and the viscosity of the substrate η_{PMMA} assuming the shearing due to the drawing of the rim occurs in the surrounding matrix.

Figure 6 displays the appearance and growth of holes within the PS film in the PMMA matrix as a function of time. The pictures of the holes suggest the existence of a rim (dark region at the edge of the hole). This is consistent with what is observed in reference⁵³ as opposed to what is reported for free standing films.^{60, 61}

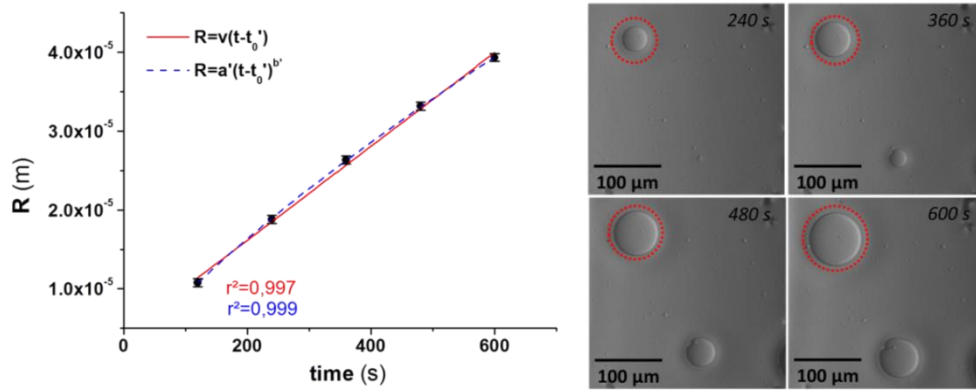


Figure 6: growth of a hole in a PS thin film (260 nm) surrounded by PMMA (thickness above and below $\sim 3 \mu\text{m}$) at 200 °C. On the left, evolution of the radius over time and fits using equation 7.

Concerning the hole growth, first, one can see that the best fit is obtained for an exponent between 0.8 and 0.9 (depending on the trilayers tested). Secondly it can be seen that the scenario described by equation 8 (much simpler than what happens for bilayers) fits well the data but that an “induction time” t_0 needs to be introduced (as was observed experimentally for bilayers,²⁵ but is not predicted by Brochard²⁴). However the value obtained from the fit for this induction time is, in some cases, negative (-70 s in the example in figure 6), which has no physical meaning. It could be explained by the existence of a transient regime where the hole, right after appearing, grows very fast for a few seconds before reaching a constant velocity. Unfortunately, our setup prevented us from capturing what happens during the initial stages of the bursting. When the first image is taken, around 45 s after the beginning of the experiment, holes were visible in the cases where t_0 is negative, which only allows us to say that t_0 , if it exists, is smaller than 45 s.

Several holes on different samples were monitored and different experimental conditions were studied. The main results are presented in figure 7 and 8.

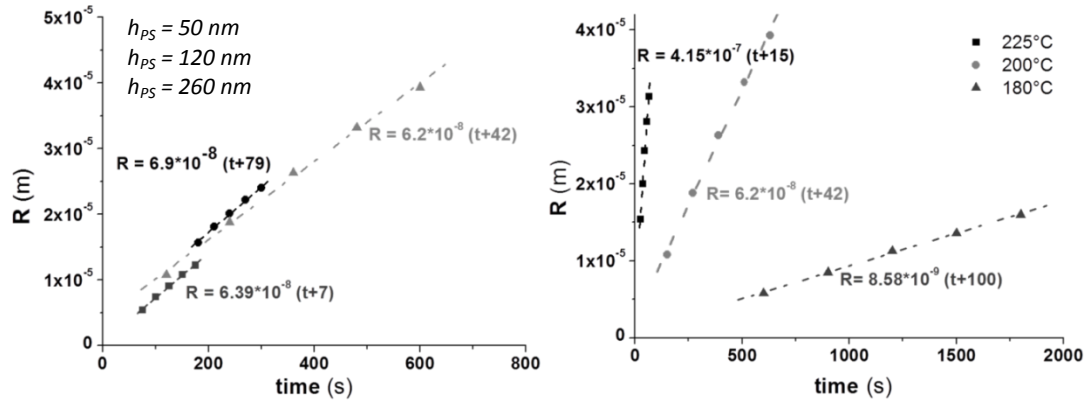


Figure 7: growth of a typical hole at 200 °C for PS films with various thicknesses, embedded in 2 PMMA VM100 layers (3 μm thick) (left). Growth of a typical hole for a 260 nm thick PS film embedded in 3 μm thick PMMA layers at various temperatures (right).

First, as predicted by the simple model adapted from Reyssat and Quéré,⁵³ the thickness of the PS film does not modify the bursting speed (see figure 7, left). The expected dependence on the temperature (i.e. on the viscosity of the surrounding matrix) is also observed (figure 7, right). Similar results were also obtained using PMMA V825T as a matrix, at 200 °C and 225 °C. Second, the experimental speed is extremely close to the theoretical speed calculated using the simple scaling in equations 7 and 8: a difference of less than 50% is observed on average, for all conditions studied.

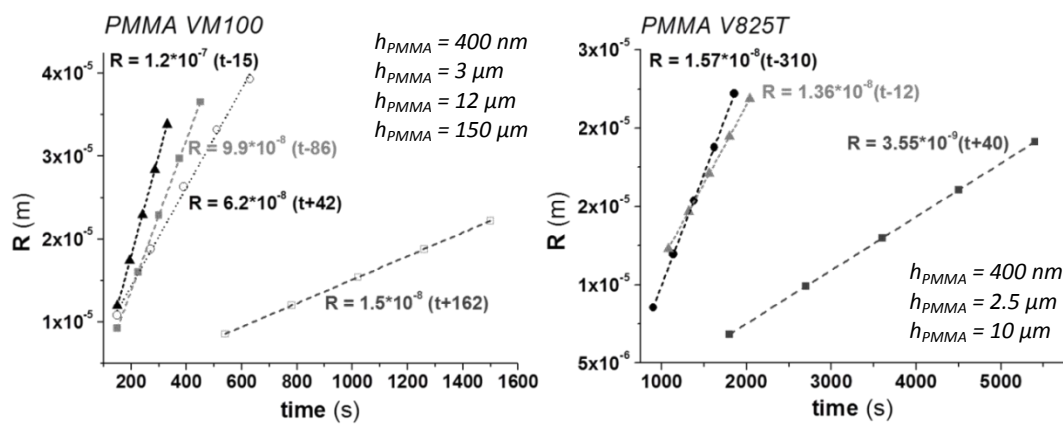


Figure 8: evolution of the bursting speed of a 270 nm PS film as a function of the PMMA surrounding layers thicknesses (left: PMMA VM100, right: PMMA V825T) at 200 °C.

Then, the effect of the thickness of PMMA on the bursting speed was studied for both PMMA (figure 10). Interestingly, a slower kinetics is observed for thin PMMA layers (400 nm) embedding a 270 nm PS film. For thicker PMMA layers, however, the bursting speed increases and seems to reach a constant value close to the theoretical one.

This thickness effect might be explained by the fact that the viscous dissipation within the PMMA occurs in a certain volume around the film (following, on first approximation, a Poiseuille flow), which means that this dissipation is slowed down with the thinner PMMA layers and the glass slides below and above (see figure 5). This critical thickness should depend on the viscosity, as is suggested by figure 8 (the volume of PMMA needed should decrease when the viscosity is increased). Negative induction times which are observed for the thinner PMMA layers, when the dynamics is slowed down, could also suggest that our simple model does not capture correctly these confinement effects.

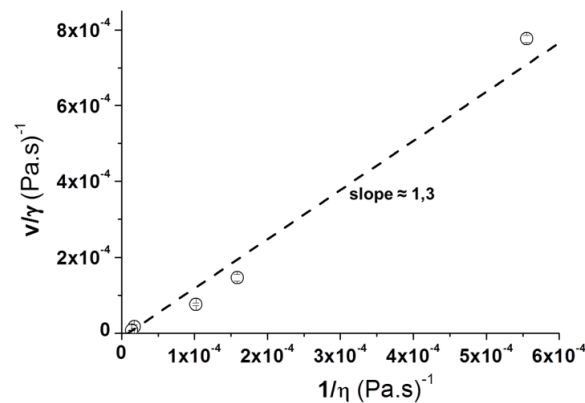


Figure 9: v/γ as a function of $1/\eta$ for all the conditions studied. Dashed line: linear fit of the experimental data.

Going back to the “unconfined matrix” conditions, we plotted for all the conditions studied for our buried PS film (within PMMA VM100 at 180, 200 and 225 °C and PMMA V825T at 200°C and 225°C), v/γ as a function of $1/\eta$ (see figure 9). A linear regression fits quite nicely the data for over two decades, as predicted by the simple model (eq. 7), with a slope close to 1.

To conclude, when comparing these results to multilayer coextrusion, we noticed that for PS/PMMA multilayer films, significant layer breakup was only observed when trying to obtain thicknesses below ~40 nm. However the characteristic time scales of the process at the same temperatures (i.e. the residence time in the feedblock containing the multiplying elements) is higher than 1 minute, as stated earlier. After 1 minute, our “model” systems all displayed, even the thicker ones ($h_{PS} \approx 260$ nm) significant breakups (many holes larger than 10 μ m in diameter) in the “static” conditions of the conducted experiments. Actually, at 225 °C which is the extrusion temperature, dewetting occurs almost instantaneously (within seconds) in the “model” experiment. Contrary to what is seen in multilayer coextrusion, our “model” system also displays no differences for the breakup of PS films of different thicknesses. This suggests that, rather counterintuitively, the elongation and shear forces induced by the flow in the multiplying elements during the extrusion actually act as stabilizing factors until a critical thickness is reached, where van der Waals forces become too strong and cause spontaneous break-up of the layers. A stabilization of van der Waals-driven rupture of thin films by shearing flows has already been

reported in the literature.^{63, 64} This stabilization may also be enabled by the lowering of the interfacial thermal-fluctuation amplitude under shear flow, as shown recently by Bickel et al.⁶⁵

2.8. Conclusion and future work

In this chapter, we showed that this study based on a process transferable to industry, has also raised fundamental questions on polymer thin film stability. Not only could the nanolayer process benefit from this field of research, but it may also be a powerful tool to reassess open questions concerning the physics of polymers under confinement. More details on ongoing or future research on this topic will be given in chapter 5.

In a few words, concerning nanolayer coextrusion: another amorphous polymer pair, PC/PMMA is being studied to confirm some of the intriguing results obtained by Baer and confirm the disjoining pressure hypothesis. Then, it appears important to study pairs presenting much higher attractive forces (for example hydrogen bonds) and to study in more details the effect of crystallization on the critical thickness.

Concerning the “static” model experiments, an ongoing study consists in analyzing more carefully the effect of interfacial tension on dewetting in the trilayers. To do that, block copolymers PS-b-PMMA are added to the systems to control (lower) the interfacial tension. In parallel, the idea is to monitor the interfacial tension as a function of parameters such as concentration of the copolymers, masses of the blocks..., via a drop relaxation method.

Secondly, we would like to focus more closely on the initial dewetting mechanism for the trilayers (spinodal or nucleation), by studying ultra-thin (from 10 to 50 nm) embedded films and especially look at the droplet morphology at the end of the dewetting.

The study of the dewetting of ultra-thin polymer multilayered films under shear also appears to be a necessary step towards a deeper understanding of layer breakup phenomenon in nanolayer coextrusion. First experiments using a rheo-optic experimental set-up allowing observing these instabilities in shear-controlled conditions have been conducted and will be detailed in chapter 5 (we will show that this is a complicated experiment and that some efforts on the design of the set-up have to be made). From a fundamental point of view, this topic of research is important since the effect of shear flow on the kinetics of dewetting of ultra-thin polymer flows has never been studied experimentally until now. This experimental study shall be coupled with a theoretical approach on hydrodynamics of ultra-thin viscous films by including disjunction pressure in Stokes equation. This theoretical approach will allow understanding the flow induced effect on the thermal fluctuations amplitude, on the kinetics of instabilities growth and on the stability of thin layers in the nanolayer coextrusion.

2.9. References

1. In *Hierachically Structured Materials*, MRS Symposium Proceedings, 1992; Aksay, I. A. B., E.; Sarikaya, M.; Tirrell, D.A., Ed. Cambridge University Press: **1992**.
2. Sun, J.; Bhushan, B., Hierarchical structure and mechanical properties of nacre: a review. *Rsc Advances* **2012**, 2, (20), 7617-7632.
3. Roberts, G., *Langmuir-Blodgett Films*. 1 ed.; Springer US: New-York, **1990**.
4. Wang, K.; Chen, F.; Li, Z.; Fu, Q., Control of the hierarchical structure of polymer articles via "structuring" processing. *Progress in Polymer Science* **2016**, 39, (5), 891-920.
5. Liu, R. Y. F.; Bernal-Lara, T. E.; Hiltner, A.; Baer, E., Polymer interphase materials by forced assembly. *Macromolecules* **2005**, 38, (11), 4819-4827.
6. Scholtyssek, S.; Adhikari, R.; Seydewitz, V.; Michler, G. H.; Baer, E.; Hiltner, A., Evaluation of Morphology and Deformation Micromechanisms in Multilayered PP/PS Films: An Electron Microscopy Study. *Macromolecular Symposia* **2010**, 294, (1), 33-44.
7. Ho, K. L., J.S.; Viriyabanthorn, C.; Sung, C.; Barry, C.M.F.; Mead, J.L, Interfacial Instabilities in Multilayer Extrusion. In *Nanotech 2004*, NSTI: **2004**; Vol. Technical Proceedings of the 2004 NSTI Nanotechnology Conference and Trade Show, Volume 3, pp 468-471.
8. Lin, Y.; Hiltner, A.; Baer, E., A new method for achieving nanoscale reinforcement of biaxially oriented polypropylene film. *Polymer* **2010**, 51, (18), 4218-4224.
9. Theory of Interface Distortion in Stratified Two-Phase Flow. *Transactions of the Society of Rheology* **1975**, 19, (3), 457-479.
10. Han, C. D., Introduction to Stratified Multiphase Flow in Polymer Processing. In *Multiphase Flow in Polymer Processing*, Academic Press: **1981**; pp 341-342.
11. Dooley, J.; Rudolph, L., Viscous and Elastic Effects in Polymer Coextrusion. *Journal of Plastic Film & Sheeting* **2003**, 19, (2), 111-122.
12. Wilson, G. M.; Khomami, B., An experimental investigation of interfacial instabilities in multilayer flow of viscoelastic fluids: Part I. Incompatible polymer systems. *Journal of Non-Newtonian Fluid Mechanics* **1992**, 45, (3), 355-384.
13. Wilson, G. M.; Khomami, B., An experimental investigation of interfacial instabilities in multilayer flow of viscoelastic fluids. Part II. Elastic and nonlinear effects in incompatible polymer systems. *Journal of Rheology* **1993**, 37, (2), 315-339.
14. Wilson, G. M.; Khomami, B., An experimental investigation of interfacial instabilities in multilayer flow of viscoelastic fluids. III. Compatible polymer systems. *Journal of Rheology* **1993**, 37, (2), 341-354.
15. Chen, K., Interfacial instability due to elastic stratification in concentric coextrusion of two viscoelastic fluids. *Journal of Non-Newtonian Fluid Mechanics* **1991**, 40, (2), 155-175.
16. Hinch, E. J.; Harris, O. J.; Rallison, J. M., The instability mechanism for two elastic liquids being co-extruded. *Journal of Non-Newtonian Fluid Mechanics* **1992**, 43, (2), 311-324.
17. Valette, R.; Laure, P.; Demay, Y.; Agassant, J. F., Convective linear stability analysis of two-layer coextrusion flow for molten polymers. *Journal of Non-Newtonian Fluid Mechanics* **2004**, 121, (1), 41-53.
18. Scott, C. E.; Macosko, C. W., Model experiments concerning morphology development during the initial stages of polymer blending. *Polymer Bulletin* **1991**, 26, (3), 341-348.
19. Sundararaj, U.; Dori, Y.; Macosko, C. W., Sheet formation in immiscible polymer blends: model experiments on initial blend morphology. *Polymer* **1995**, 36, (10), 1957-1968.
20. Sundararaj, U.; Macosko, C. W.; Rolando, R. J.; Chan, H. T., Morphology development in polymer blends. *Polymer Engineering & Science* **1992**, 32, (24), 1814-1823.
21. Elemans, P. H. M.; Bos, H. L.; Janssen, J. M. H.; Meijer, H. E. H., Transient phenomena in dispersive mixing. *Chemical Engineering Science* **1993**, 48, (2), 267-276.
22. Krausch, G., Dewetting at the interface between two immiscible polymers. *Journal of Physics-Condensed Matter* **1997**, 9, (37), 7741-7752.
23. Reiter, G., Dewetting of thin polymer films. *Physical Review Letters* **1992**, 68, (1), 75-78.
24. Wyart, F. B.; Martin, P.; Redon, C., Liquid-liquid dewetting. *Langmuir* **1993**, 9, (12), 3682-3690.
25. Qu, S.; Clarke, C. J.; Liu, Y.; Rafailovich, M. H.; Sokolov, J.; Phelan, K. C.; Krausch, G., Dewetting dynamics at a polymer-polymer interface. *Macromolecules* **1997**, 30, (12), 3640-3645.
26. Seemann, R.; Herminghaus, S.; Jacobs, K., Gaining control of pattern formation of dewetting liquid films. *Journal of Physics: Condensed Matter* **2001**, 13, (21), 4925.
27. Vrij, A., Possible mechanism for the spontaneous rupture of thin, free liquid films. *Discussions of the Faraday Society* **1966**, 42, (0), 23-33.

28. Sheludko, A., Thin liquid films. *Advances in Colloid and Interface Science* **1967**, 1, (4), 391-464.
29. Bironeau, A. Films multianocouches de polymères coextrudés. ENSAM, Paris, **2016**.
30. Bironeau, A.; Dirrenberger, J.; Sollogoub, C.; Miquelard-Garnier, G.; Roland, S., Evaluation of morphological representative sample sizes for nanolayered polymer blends. *Journal of Microscopy* **2016**, 264, (1), 48-58.
31. Bironeau, A.; Salez, T.; Miquelard-Garnier, G.; Sollogoub, C., Existence of a critical layer thickness in PS/PMMA nanolayered films. Submitted to *Macromolecules* In **2017**. arXiv:1703.09517
32. Fetters, L. J.; Lohse, D. J.; Richter, D.; Witten, T. A.; Zirkel, A., Connection between Polymer Molecular Weight, Density, Chain Dimensions, and Melt Viscoelastic Properties. *Macromolecules* **1994**, 27, (17), 4639-4647.
33. Israelachvili, J. N., Chapter 13 - Van der Waals Forces between Particles and Surfaces. In *Intermolecular and Surface Forces (Third Edition)*, Academic Press: San Diego, **2011**, pp 253-289.
34. Meijer, H. E. H.; Janssen, J. M. H.; Anderson, P. D., Mixing of Immiscible Liquids. In *Mixing and Compounding of Polymers*, Carl Hanser Verlag GmbH & Co. KG: **2009**; pp 41-182.
35. de Silva, J. P.; Cousin, F.; Wildes, A. R.; Geoghegan, M.; Sferrazza, M., Symmetric and asymmetric instability of buried polymer interfaces. *Physical Review E* **2012**, 86, (3), 4.
36. de Silva, J. P.; Geoghegan, M.; Higgins, A. M.; Krausch, G.; David, M. O.; Reiter, G., Switching layer stability in a polymer bilayer by thickness variation. *Physical Review Letters* **2007**, 98, (26), 4.
37. Miquelard-Garnier, G.; Roland, S. b., Beware of the Flory parameter to characterize polymer-polymer interactions: A critical reexamination of the experimental literature. *European Polymer Journal* **2016**, 84, 111-124.
38. Russell, T. P.; Hjelm, R. P.; Seeger, P. A., Temperature dependence of the interaction parameter of polystyrene and poly(methyl methacrylate). *Macromolecules* **1990**, 23, (3), 890-893.
39. Wu, S., Surface and interfacial tensions of polymer melts. II. Poly(methyl methacrylate), poly(n-butyl methacrylate), and polystyrene. *The Journal of Physical Chemistry* **1970**, 74, (3), 632-638.
40. Carriere, J. C.; Biresaw, G.; Sammler, L. R., Temperature dependence of the interfacial tension of PS/PMMA, PS/PE, and PMMA/PE blends. *Rheologica Acta* **2000**, 39, (5), 476-482.
41. Liu, R. Y. F.; Ranade, A. P.; Wang, H. P.; Bernal-Lara, T. E.; Hiltner, A.; Baer, E., Forced assembly of polymer nanolayers thinner than the interphase. *Macromolecules* **2005**, 38, (26), 10721-10727.
42. Brown, H. R., Effect of a diblock copolymer on the adhesion between incompatible polymers. *Macromolecules* **1989**, 22, (6), 2859-2860.
43. Zhang, J.; Lodge, T. P.; Macosko, C. W., Interfacial slip reduces polymer-polymer adhesion during coextrusion. *Journal of Rheology* **2006**, 50, (1), 41-57.
44. Arabeche, K.; Delbreilh, L.; Adhikari, R.; Michler, G. H.; Hiltner, A.; Baer, E.; Saiter, J.-M., Study of the cooperativity at the glass transition temperature in PC/PMMA multilayered films: Influence of thickness reduction from macro- to nanoscale. *Polymer* **2012**, 53, (6), 1355-1361.
45. Kim, W. N.; Burns, C. M., Blends of polycarbonate and poly(methyl methacrylate) and the determination of the polymer-polymer interaction parameter of the two polymers. *Macromolecules* **1987**, 20, (8), 1876-1882.
46. Callaghan, T. A.; Paul, D. R., Estimation of interaction energies by the critical molecular weight method: 1. Blends with polycarbonates. *Journal of Polymer Science Part B: Polymer Physics* **1994**, 32, (11), 1813-1845.
47. Carriere, C. J.; Cohen, A., Evaluation of the interfacial tension between high molecular weight polycarbonate and PMMA resins with the imbedded fiber retraction technique. *Journal of Rheology* **1991**, 35, (2), 205-212.
48. Kerns, J.; Hsieh, A.; Hiltner, A.; Baer, E., Comparison of irreversible deformation and yielding in microlayers of polycarbonate with poly(methylmethacrylate) and poly(styrene-co-acrylonitrile). *Journal of Applied Polymer Science* **2000**, 77, (7), 1545-1557.
49. Bernal-Lara, T. E.; Liu, R. Y. F.; Hiltner, A.; Baer, E., Structure and thermal stability of polyethylene nanolayers. *Polymer* **2005**, 46, (9), 3043-3055.
50. Cole, P. J.; Cook, R. F.; Macosko, C. W., Adhesion between Immiscible Polymers Correlated with Interfacial Entanglements. *Macromolecules* **2003**, 36, (8), 2808-2815.
51. Adhikari, R.; Seydewitz, V.; Löschner, K.; Michler, G. H.; Hiltner, A.; Baer, E., Structure and Properties of Multilayered PET/PC Composites. *Macromolecular Symposia* **2010**, 290, (1), 156-165.
52. Demarquette, N. R.; Kamal, M. R., Interfacial tension in polymer melts. I: An improved pendant drop apparatus. *Polymer Engineering & Science* **1994**, 34, (24), 1823-1833.
53. Reyssat, E.; Quere, D., Bursting of a fluid film in a viscous environment. *Europhysics Letters* **2006**, 76, (2), 236-242.

54. Zhu, Y.; Bironeau, A.; Restagno, F.; Sollogoub, C.; Miquelard-Garnier, G., Kinetics of thin polymer film rupture: model experiments for a better understanding of layer breakups in the multilayer coextrusion process. *Polymer* **2016**, *90*, 156-164.
55. Wang, C.; Krausch, G.; Geoghegan, M., Dewetting at a polymer-polymer interface: Film thickness dependence. *Langmuir* **2001**, *17*, (20), 6269-6274.
56. Xue, L. J.; Hu, B. H.; Han, Y. C., Effect of interfacial roughness on dewetting behavior of polystyrene/poly(methyl methacrylate) bilayer film. *Journal of Chemical Physics* **2008**, *129*, (21), 6.
57. Lambooy, P.; Phelan, K. C.; Haugg, O.; Krausch, G., Dewetting at the liquid-liquid interface. *Physical Review Letters* **1996**, *76*, (7), 1110-1113.
58. Frankel, S.; Mysels, K. J., Bursting of soap films. II. Theoretical considerations. *The Journal of Physical Chemistry* **1969**, *73*, (9), 3028-3038.
59. McEntee, W. R.; Mysels, K. J., Bursting of soap films. I. An experimental study. *The Journal of Physical Chemistry* **1969**, *73*, (9), 3018-3028.
60. Debrégeas, G.; Martin, P.; Brochard-Wyart, F., Viscous Bursting of Suspended Films. *Physical Review Letters* **1995**, *75*, (21), 3886-3889.
61. Xavier, J. H.; Pu, Y.; Li, C.; Rafailovich, M. H.; Sokolov, J., Transition of Linear to Exponential Hole Growth Modes in Thin Free-Standing Polymer Films. *Macromolecules* **2004**, *37*, (4), 1470-1475.
62. Eri, A.; Okumura, K., Bursting of a thin film in a confined geometry: Rimless and constant-velocity dewetting. *Physical Review E* **2014**, *82*, (3), 030601.
63. Kalpathy, S. K.; Francis, L. F.; Kumar, S., Shear-induced suppression of rupture in two-layer thin liquid films. *Journal of Colloid and Interface Science* **2010**, *348*, (1), 271-279.
64. Davis, M. J.; Gratton, M. B.; Davis, S. H., Suppressing van der Waals driven rupture through shear. *Journal of Fluid Mechanics* **2010**, *661*, 522-539.
65. Thiebaud, M.; Bickel, T., Nonequilibrium fluctuations of an interface under shear. *Physical Review E* **2010**, *81*, (3), 031602.

Chapter 3

Some applications of nanolayer coextrusion:

nanocomposites and forced self-assembly

(this chapter is mainly based on 3 articles and a patent co-written with various colleagues through 3 collaborations, see references ^{1, 2, 3, 4}. The section on nanocomposites presents part of the PhD thesis of Xiguang Li defended in January 2015. The part on self-assembly will present preliminary results from the PhD work of Juan-Sebastian Montana which will be defended in November 2017. Other studies concern the design of films presenting optimized barrier properties for various packaging applications but will not be detailed here since they are mostly lead by A. Guinault and C. Sollogoub. The reader may still refer to references ^{5, 6} for example, among others in the group).

As was stated in chapter 2, many fundamental questions concerning more generally the physics of confined viscoelastic liquids arise from nanolayer coextrusion. Answers to these questions could certainly improve the process and its potential industrial impact, but this process could also be a powerful tool to design model materials for studying such problems. However, we want to present here more applied studies where nanolayer coextrusion was used.

3.1. Nanocomposites

Polymer-based nanocomposites have received a huge amount of interest over the past ten years due to the unique combination of properties of nanofillers such as carbon nanotubes, graphene, nanoclays and others, mainly their large aspect ratio, low density, extremely high tensile moduli and strengths, toughness etc.⁷ In consequence, they have been for quite a long time considered as potentially ideal fillers in high performance polymer composites, with the idea that despite their usually high price, a very low fraction compared to classical fillers could lead to higher reinforcements.⁸

To achieve good final properties, especially mechanical, of the composite, one however does need to fulfill some requirements.⁹ Especially, a good dispersion/distribution of the nanofillers needs to be achieved: because of large surface areas of contact possibly creating physical entanglements and physical interactions such as Van der Waals forces, such fillers are often agglomerated. This can dramatically decrease the efficiency of the filler, because it can create local stress concentrations and diminish the effective aspect ratio. Moreover, compatibility between the polymer matrix and the nanofillers due to their chemical structures, play an important role in the final properties of the composites. In consequence, a complete picture of the relationship between the microstructure and the final properties of the material is still lacking (it appears for example that the “ideal” microstructure is not the same when electric properties or mechanical properties are wanted).

Several methods have been studied to prepare nanocomposites and thoroughly reviewed in the literature (see for example references ⁸⁻¹⁰).

Solution processing may be the most common method used at small scales to obtain such composites. The idea is simply to mix the nanofiller and the polymer in an appropriate solvent, and then to form a film by evaporating the solvent. It usually gives good results in terms of macroscopic properties (reinforcement) since it facilitates nanofiller de-aggregation and dispersion. Chemical processing can be achieved via in-situ polymerization or covalent functionalization of nanofillers. The idea is to graft polymer chains on the surface of the filler to enhance dispersion and form a strong interface between the polymer and the matrix.

However, melt processing is the only way to produce nanocomposites that is compatible with standard industrial processes (injection, extrusion, compression moulding), due to its speed, cost and relative simplicity. An alternative route, solid-state shear pulverization, where a twin-screw extruder is modified to maintain the polymer in its solid state during processing, appears promising but is still in its early stages.¹¹⁻¹³ In fact, this method actually has been less fundamentally studied than the others, and to this day gave the least interesting results, despite few exceptions.¹⁰ This is mainly due to the fact that one is dealing with relatively high viscosities that affect the ability to disperse efficiently nanofillers in the matrixes, especially if they do not have favorable interactions (which is often the case for nanofillers and polyolefines). One of the most common industrial techniques for melt mixing is extrusion, and especially twin-screw extrusion in the case of nanocomposites. However, only few articles (compared to the rest of the literature) use this method to create nanocomposites. Pötschke et al. (for example references¹⁴⁻¹⁷) have published a large amount of work over the past few years in order to study extensively the role of different parameters using a twin-screw extruder in obtaining good dispersion of carbon nanotubes (CNT) or other nanofillers within different polymer matrixes. In particular, these studies have pointed out the crucial importance of factors like matrix infiltration, master batch dilution technique, specific mechanical energy, screw configurations...

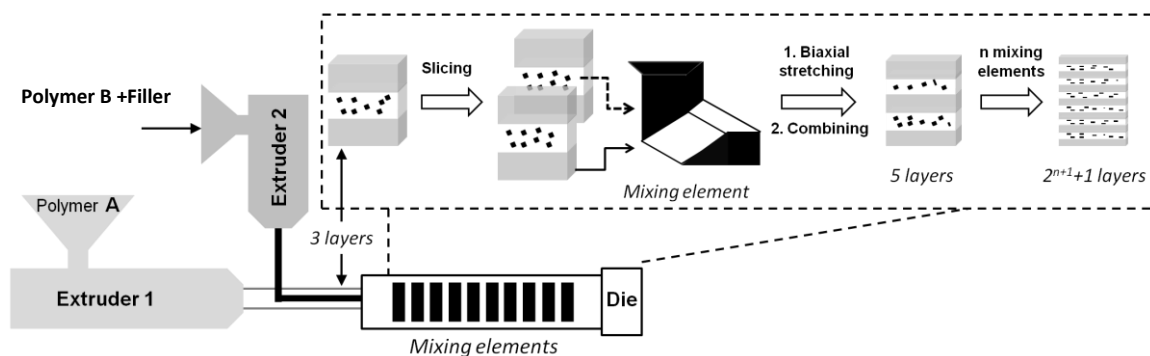


Figure 1: Schematic of the multilayer coextrusion process for production of multilayered polymer nanocomposites with alternating layers of unfilled polymer and polymer containing oriented graphene (polymer A and polymer B can be different or identical).

3.1.1 Carbon nanotubes – polypropylene nanolayered composites

In this work, we propose the use of a scalable industrial process, nanolayer coextrusion, to improve the dispersion and distribution of CNT in a polypropylene matrix to achieve interesting mechanical properties at low contents of CNT. In the context of this study, the idea is to use the nanolayer coextrusion more as a “mixing” tool: in this work we produce “layers” of the same polymer charged with CNT of roughly 10 nm, i.e. smaller than the typical size of the aggregates (see figure 1). Hence, the shear stress created by multilayer coextrusion should disperse the CNTs aggregates and simultaneously orientate and align them in the extrusion

direction and the confined structure should force breaking of the aggregates.^{3, 4} This idea has been scarcely studied to our knowledge: Jana et al. studied a similar mixing method (called “chaotic” mixing) to disperse oxidized carbon nanofibers in PMMA and thermoplastic polyurethane with promising results especially in the viscoelastic region.^{18, 19} Recently, Guo et al. studied the conductivity of polypropylene nanocomposites made using a quite similar device based on single extrusion and so-called laminating multiplying elements (LME)^{20, 21} but performed no mechanical measurements.

Polypropylene PPH5060 is a homopolymer polypropylene grade developed by Total Petrochemicals suitable for extrusion, and will be used as the matrix in the nanocomposites produced. The Melt Flow Index (MFI) is 6 g / 10 min (230 °C / 2.16 kg). Melt Flow Index is a standardized test related to the ease of flow of a polymer melt (i.e. viscosity) which is often used to quantify processability. Polypropylene grafted with maleic anhydride (PPgAM) was used in small quantity (between 0.5 and 7 wt%) to increase the compatibility between the matrix and the CNT. Noncommercial Orevac PPgAM similar to the CA100 (high content of maleic anhydride) was obtained via Arkema. Due to defects occurring during their fabrication, MWCNT present polar groups such as hydroxyl groups at their surface. It has already been shown that polymers grafted with anhydride maleic improves the interactions between matrix and CNT fillers because of the polarity of the anhydride groups. However, the exact mechanism and its consequences on the macroscopic properties are not yet fully understood since PPgAM will also affect the crystallization of the matrix.²² CNTs were obtained in masterbatch form from Nanocyl. Plasticyl PP2001 is a concentrate of MultiWall Carbon Nanotubes (MWCNT) dispersed at 20 wt% in a polypropylene matrix (PP2001, reference from Nanocyl) suitable for extrusion process. According to Nanocyl datasheets, their industrial grade MWCNT produced via catalytic carbon vapor deposition process (CVD) have a mean diameter of 9.5 nm, length about 1.5 μm and the carbon purity is 90% and 10% metal oxide impurities. All products were used as received (under pellet forms).

Before nanolayer coextrusion, formulations have been prepared using a twin screw extruder (Thermo Haake PTW 16-40D) at 240°C. The goal with twin-screw extrusion is here to dilute the CNT masterbatch from 20 wt% to a lower concentration (values from 0.2 to 5 wt% were tested in this study), since the masterbatch cannot be extruded as is using the multilayer co-extrusion process, due to its high viscosity. Following the work of Pötschke and coworkers,¹⁴⁻¹⁷ the effect of the specific mechanical energy (SME) defined by

$$SME = \frac{\tau N}{\dot{m}} \quad (\text{Eq. 1})$$

where τ is the torque of the screw, N the speed of the screw and \dot{m} the throughput, was studied. SME is given in kJ/kg and basically defines a “good mixing”: the faster and the longer, the better.

The formulations produced are cooled in a water bath at the end of the extruder, cut into pellets later using a mechanical grinder, and are later used in the lateral extruder during the multilayer co-extrusion. These formulations were made with CNT concentrations from 2 to 7.5 wt% with most of them at 5 wt%, which then allows producing via multilayer co-extrusion films with concentrations between 0.1 and 1 wt%.

In the nanolayer coextrusion step, PP has been extruded to form the outer skin layers and twin-screw formulations the core layer. In most cases, 10 static mixers have been used and the number of the total layers in the final sample after the mixing section should be 2049. In this study, two laboratory single screw extruders have been used: a 30 mm diameter (Mapre) for the main flow and a lateral 20 mm diameter (Scamex) for the minor flow. The end temperatures for both extruders were fixed at 240 °C. The throughput of each extruder was adjusted to produce samples with varying final amounts of CNT. The throughput was controlled by fixing

the screw speed. It is worth noting that, due to the capacities of each extruder and contrary to the setup described in the previous chapter, the typical weight ratio between the Mapre and the Scamex is between 95/5 and 80/20.

The importance of both diluting the masterbatch with a high SME and with a blend of PPgAM and PP before using the obtained formulation in the lateral extruder is clearly illustrated in figure 2. In particular, presence of PPgAM is necessary to get rid of very big aggregates (with areas $\sim 1000 \mu\text{m}^2$) using the multilayer coextrusion process even at low concentrations of CNT (below 1 wt%) and with 10 mixing elements. The impact of big aggregates on the mechanical properties of the nanocomposites can clearly be evidenced by simple uniaxial traction experiments. The presence of big aggregates in the composite leads to a complete loss of the elongation at break of the material, from more than 400% for all samples to as low as 1 or 2 % (i.e. before necking) with very large differences between samples. Working with a high SME also helps to prevent from the presence of thinner aggregates that could remain in the composite. Similar effects on the dispersion of CNT in PE matrixes were observed very recently by Pötschke et al.²³ using PEG as a compatibilizer.

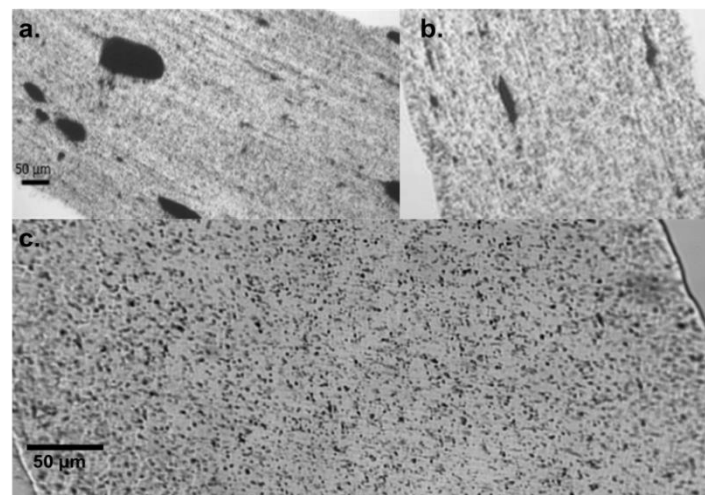


Figure 2: Comparison of the microstructure for different samples with 0.5 % CNT. a. With no PPgAM and medium SME. b. with 2.5 wt% final PPgAM and a medium SME used for the first dilution.(a and b: same scale bar) c. with 2.5 wt% final PPgAM and a high SME.

However, it is important to note that adding compatibilizer results in competitive mechanisms: too low concentrations do not impact the dispersion but too high concentrations result in the reorganization of layers during the multilayer process leading to reaggregation of CNT. It also acts as a plasticizer which affects the mechanical properties of the matrix as will be discussed below.

Concerning the SME, we observed as Pötschke et al.¹⁴⁻¹⁷ that increasing the SME favors the dispersion, or more precisely diminish the number of “big” aggregates (eg with diameters $> 5 \mu\text{m}$) in the polymer matrix (see figure 3b and 3c). This has been quantified more precisely in reference ⁴ using an image analysis. Interestingly, all samples made using high SME/any amount of PPgAM between 0.5 and 7 % displayed elongations at break higher than 400%, whereas it was not the case for any samples made at low or medium SME values.

These results suggest that an optimized formulation can be achieved: prepared at high SME (> 2500 kJ/kg for our twin-screw extruder), with concentrations below 0.5 wt% CNT in the film and a 5 to 1 ratio of PPgAM (for example 1 % of PPgAM for 0.2 wt% of CNT).

In the results presented in figure 3 (left), the lateral extruder was fed with a formulation made using 25 % masterbatch, 12.5 % PPgAM and 62.5 % PPH5060 with a SME around 5000 kJ/kg. The film was produced using a 90/10 weight ratio between the two extruders. It shows that both moduli (and yield strength) increase by more than 20 %, while the elongation at break remains higher than 300 % for the nanocomposite PP film (actually, no breaking was observed below 450 % - the limit of the apparatus- for all samples tested).

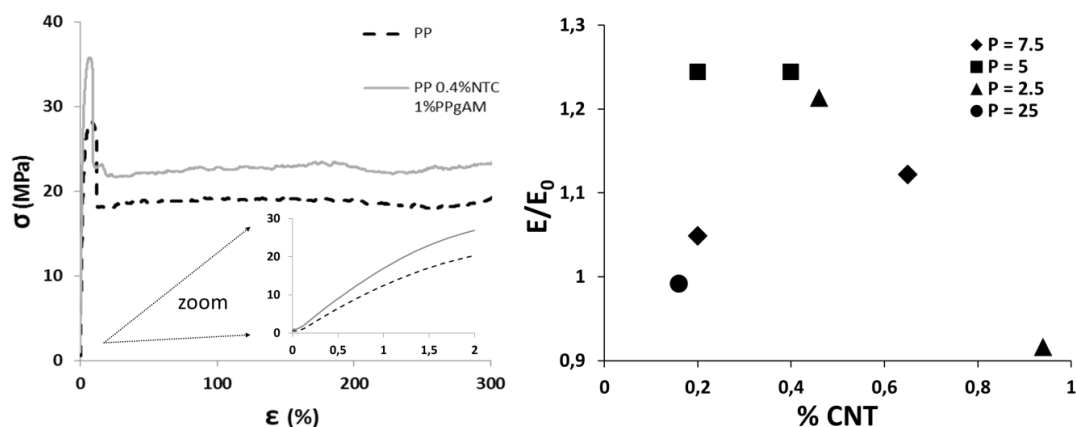


Figure 3: typical traction curves of reinforced PP versus neat PP (left). Comparison of the Young's modulus for samples with different P values (E_0 being the Young's modulus of neat PP) as a function of the CNT concentration. All samples were prepared at high SME and thus have elongation at break higher than 400% (right).

Figure 3 (right) shows that too little compatibilizer (P is defined as the ratio of the quantity of compatibilizer over the quantity of CNT, in wt%) does not lead to a good reinforcement, while too much leads to a competition between the capacity to disperse effectively more CNT and the lowering of the mechanical properties of the matrix. In this study, the optimum film was found to be with final concentrations of 0.2 % CNT and 1 % PPgAM, with 25 % increase in the modulus while the elongation at break was fully maintained. At the same ratio between CNT and PPgAM, same reinforcement was observed with 0.4 % CNT (hence 2 % of PPgAM), and similar values (> 20 %) were obtained using 0.4 % CNT and only 1 % of PPgAM. However, the reinforcement decreases drastically with CNT concentrations above 0.5 % with higher or lower amounts of PPgAM. This suggests this method may not be helpful to disperse high quantities of CNT (>0.5 wt%). However it gives remarkable results with very low amounts of CNT and can be useful in terms of cost effectiveness. In comparison, a sample prepared by dryblending all ingredients at the desired concentrations (0.2 wt% CNT, 1 wt% PPgAM, 98.8 wt% PP) in a single screw extruder leads to only 5 % increase in the Young's modulus while the elongation at break goes down to 70% with large standard deviations (breaking of samples occur between 1,6 % and 210 % deformation).

DMTA results showed that this reinforcement is maintained and even increased over the whole temperature range before melting. For example, at 80°C, this increase in the storage modulus can be as high as 60 %. This suggests a better ability for these materials to be used at high temperature.

DSC data revealed that the effect of CNT addition in PP matrix on T_m and X_c is rather marginal. These results seem to indicate that the incorporation of CNT in PP matrix does not affect significantly the crystallinity of PP, which is in agreement with other results reported in literature for this matrix.²⁴ It means in particular, that the improvement of the nanocomposite mechanical properties cannot be attributed to a significant change in the matrix crystallinity.

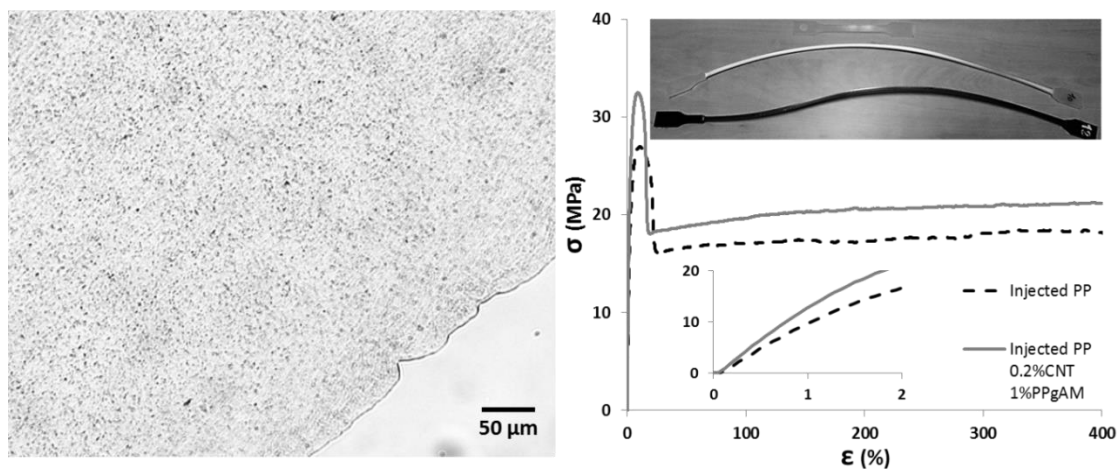


Figure 4: injection experiments. Typical microstructure observed by optical microscopy (left). Typical results obtained by traction measurements (right): elongation at break above 400% (top picture and main graph), significant increase in modulus (inset).

The final interesting result, especially in terms of industrial application, is the possibility to apply this method to make injected pellets. We used the nanolayer coextrusion with the same experimental conditions and the same formulations to produce strings (0.2 wt% CNT, 1 wt% PPgAM) instead of films, which were then pelletized. The resulting pellets were then injected (JSW J55ELII molding machine) at 240°C at 800 bar during 35 s, with 40 °C for the mold temperature in order to obtain normalized test specimens (dog bone shaped samples following the ENISO527-2 standard). For these samples, we showed that the average modulus as measured by uniaxial tensile test increased from 1.13 GPa for the PP to 1.45 GPa for the nanocomposite, a 28 % increase while the elongation at break remained higher than 400 % (see figure 3). Moreover, the dispersion was characterized as the best of the study (see figure 4). In consequence, no reaggregation of CNT occurs if a second processing step takes place and on the contrary, the injection step appears to improve further the dispersion.

The results obtained have been compared to simple estimates using the Halpin-Tsai model for short fiber reinforced composites.²⁵ According to this model based on force balance and empirical data, widely used for composites, the composite modulus can be estimated as follow:

$$E_{comp} = E_{PP} \frac{(1 + \xi \eta v_f)}{(1 - \eta v_f)} \quad (\text{Eq. 2})$$

$$\text{with} \quad \xi = 2 \left(\frac{l}{d} \right) \quad \text{and} \quad \eta = \frac{E_{CNT} - E_{PP}}{E_{CNT} + \xi E_{PP}}$$

where E_{PP} , E_{CNT} and E_{comp} are the Young's moduli for PP, CNT and the composite respectively, v_f the volume fraction of CNT in the composite, l and d the average length and diameter of the nanotube.

Using an estimated value of 500 GPa for the CNT modulus (multiwall nanotubes being "softer" than single wall nanotubes with moduli around 1 TPa), densities of 0.905 g/cm³ for the PP, 1.66g/cm³ for the CNT, average length of 1.5 μm and average diameter of 9.5 nm as given by the suppliers, one should expect a reinforcement (E_{comp}/E_{PP}) of about 20% according to the Halpin Tsai equation with a 0.2 wt% CNT nanocomposite (around 55% according to the simple mixing rule equation). Experimental results are very close to this estimate, which suggests that the interphase or polymer in the vicinity of the nanotubes with properties different to the bulk, plays an important role in the reinforcement as CNT are still far from being perfectly dispersed in the matrix (leading to a higher "real" size of the filler compared to the size of an individual CNT). It also remains a challenge to prepare nanocomposites leading to such results, coupled with a preserved elongation at break, at higher concentrations of CNT.

Similar results were obtained using polyamide (PA 6-6) as a matrix (unpublished results).

3.1.2. Graphene – PMMA nanolayered composites

Another study dealt with graphene nanocomposites. To date, most work on graphene polymer nanocomposites has focused on isotropic or random dispersion of the graphene in the polymer matrix, giving limited reinforcement.²⁶ However, if platelet-like fillers can be aligned in a plane of the polymer matrix, they provide the possibility of two-dimensional reinforcement in the plane of orientation.²⁷ Theoretically, if the requirements of both high volume fraction of filler and in-plane alignment of the platelets are met, the mimicking of nacre-like²⁸ structures might be achieved. Therefore, methods to create such structures, especially with a potentially industrially useful method, are desirable and important.

In the general case, graphene nanocomposites have been made in ways that emphasize good dispersion and have not examined heavily the possibility of creating oriented structures. For example, it has been reported²⁹ that dispersing graphene or graphene oxide into a polymer matrix at low loadings (< 1 wt%) can lead to good mechanical reinforcement for polymer nanocomposites, such as PMMA/graphene oxide 3 (33 % enhancement of Young's modulus at only 0.01 wt%). One reason that has been given for the apparent strong reinforcement is that, via a solution mixing method, graphene and graphene oxide are dispersed with a wrinkled topology in the host polymer matrix.²⁹ Some researchers think that this provides strong interfacial adhesion between graphene and the polymer chains with a consequent significant increase in the glass transition temperature (T_g) of the polymer matrix.²⁹ If this is the case, much of the high degree of reinforcement might be attributed to the changing thermoviscoelasticity of the polymer matrix due to the changing T_g ³⁰ rather than to a mechanical reinforcement *per se*. In addition to bench scale solution mixing, graphene nanoplatelets can also be dispersed into a polymer matrix via melt mixing, i.e. in most cases through extrusion, which is the most relevant tool for exploring potential industrial applications.^{26, 31} However, due to the high viscosities of polymer melts, melt extrusion usually falls short of providing effective dispersion of nanofillers and results in filler aggregation.³²

Recently it has been shown that this method can be improved by multiplying the number of extrusion steps: a concentrated solid mixture of filler in polymers (or “master batch”) is produced by melt mixing then further dilution one or more times with the same polymer to the desired concentration,³³ resulting in better composite mechanical properties.

To the best of our knowledge, the development of methods to create in-plane oriented graphene in a polymer matrix in order to realize two-dimensional reinforcement have not been undertaken either for bench scale solution mixing or for melt extrusion. Kim and Macosko reported the production of slightly oriented polycarbonate/graphene nanocomposites obtained from injection molding. However, they also reported that wrinkling of the graphene in the polymer matrix resulted in only weak reinforcement.²⁷

What we searched to achieve in this study was evidence that the forced assembly imposed by nanolayer coextrusion, by creating a structure with extremely thin layers filled with graphene, has the potential of creating a new type of nanocomposite in which in-plane oriented graphene is the reinforcing element.

Neat poly(methyl methacrylate) was again supplied by *Altuglas International* (PMMA V920T, MFI is 6 g / 10 min at 230 °C / 3.8 kg; GPC using tetrahydrofuran and calibrated with polystyrene standards gives $M_w = 110 \text{ kg}\cdot\text{mol}^{-1}$, $\bar{D}_M = 2.15$). Prior to extrusion the PMMA systems were dried in a SOMOS dry air dryer T 20 eco system at 80 °C for 4 hours. The virgin graphene nanoplatelets came from *ACS Materials* and were used to make PMMA/graphene master batches (20 wt%) in our laboratories. The characteristics of the graphene nanoplatelets as given by the supplier are thickness between 2 and 10 nm, lateral size between 5 and 10 μm , and aspect ratio (A_f) between 1000 and 2000.

The lab-made PMMA / 20 wt% graphene master batch is prepared from the Altuglas PMMA and the *ACS Materials* graphene nanoplatelets following a solution mixing method used by Ramanathan et al³⁴ and adapted here for bigger quantities. 15 g graphene and 60 g PMMA are dissolved in 600 mL THF (*Emparta ACS*) at 40 °C and the mixture mechanically stirred for 2 h to assure good dispersion. The mixture is then precipitated by adding 6 L water and vacuum dried at 80 °C for 24 h. Prior to multilayer coextrusion, the relevant PMMA-graphene formulations (0.5, 1.0 and 2.0 wt%) to be used in extruder 2 (see figure 1) are prepared by diluting the PMMA-20 wt% graphene with the neat PMMA using a Thermo Haake PTW 16-40D co-rotating twin-screw extruder at 600 rpm and 215 °C. SME was around 5000 kJ/ kg and fixed as high as possible as discussed above.

Multilayer coextrusion requires a reasonable viscosity match between the polymer melt streams.³⁵ In the present study, because the films have been prepared with different amounts of graphene nanoplatelets, the viscosity ratio between the two melt streams ($\eta_{\text{graphene filled polymer}} / \eta_{\text{PMMA}}$) could not be maintained constant. The viscosity ratios were obtained from the apparent steady shear viscosities of all polymers and graphene formulations as a function of temperature to choose acceptable operating conditions. The viscosity ratio varied with increasing concentration of graphene. At the shear rate of 4s^{-1} to simulate the flow condition in the extrusion it varied from 1 to 0.53 at 225 °C for the graphene filled PMMA at concentrations from 0.5 to 2.0 wt%.

Using the multilayer coextrusion process (Figure 1), the primary polymer melt A (PMMA) and the secondary polymer melt (PMMA filled with graphene) are extruded from two single-screw extruders (same as those described in the previous study) respectively, combined in a classical three layer coextrusion feed block (ABA). In this study, the percentage of the secondary melt in the film is kept constant at 10 wt%. Exact values for this ratio were calculated after extrusion by measuring the mass flow rate and always found to be between 9.3 and

10.8 %. The final concentration of graphene is then 0.05, 0.1 and 0.2 wt% in the films. 0, 6 and 10 mixing elements have been used, giving films containing respectively 3, 129 and 2049 layers. These are then spread through a flat die (width = 100mm, thickness = 1mm) and onto a chill roll drawn at 1.7 m/min and maintained at 80 °C to allow relaxation of the PMMA. The result is a rectangular film made up of the alternating layers. For the two single-screw extruders, mixing elements and die have been set to 225 °C for the PMMA/PMMA systems and 240 °C for the PMMA/PS systems. The residence time for the melts in the mixing element segment, estimated using the throughput of the extruder, is approximately 2 minutes.

We first used optical microscopy to characterize the morphology of the multilayer films at the micro-scale and to compare the dispersion of graphene nanoplatelets for films with different number of layers. To quantify the dispersion of graphene nanoplatelets, the fraction R of the total aggregates with diameter $> 5 \mu\text{m}$ (area $> 19.6 \mu\text{m}^2$) over the total area of the sample have been determined following the work of Pötschke.³⁶ Although the value obtained cannot be related to the real volume fraction of aggregates in the sample, concerning the thickness of the sample imaged, it is still observed that the large aggregation (particles $> 5 \mu\text{m}$ in diameter) fraction R decreases as the number of layers increases (see figure 5). Although it is clear that some large aggregates remain in the sample, which certainly results in the local perturbation of the nano-scaled layers even when 10 mixing elements are used, the dispersion of the graphene nanoplatelets and the breakage of aggregates appears to increase upon increasing the number of layers. In the process of multilayer coextrusion, the mixing elements slice the melts with the result that the graphene aggregates are broken up to a large extent.

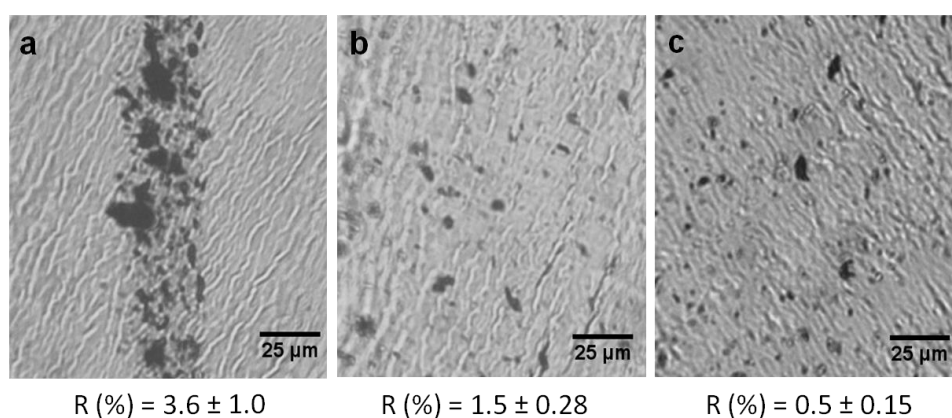


Figure 5: Optical images of PMMA/PMMA filled with 1 wt % graphene. (a: 3-layer, b: 129-layer and c: 2049-layer) and large aggregations fraction R .

STEM and TEM have in consequence been used to study the graphene orientation and aspect ratio, when the layer thickness reaches the nano-scale in the 2049-layer films (see figure 5). With no graphene, as expected (Figure 5a), there is no clear distinction between the thin PMMA and the thick PMMA layers. However, when there is 1 wt% graphene in the thin PMMA layers, the individual graphene nanoplatelets can be observed and appear mostly oriented in the plane of the layers (horizontal direction in figure 5b), with distribution of platelet length ranging from approximately 50 to 150 nm. When there is 2 wt% graphene in the layers, the concentration appears to reach an upper limit which starts to perturb the nanostructure (figures 5c and 5d).

Figure 5c displays some small or wrinkled graphene nanoplatelets which are still expected to be confined within the thin layers (dashed lines), similar to the results reported by Gupta et al.³⁷ for polypropylene/ 10 vol. % phosphate glass particle filled polypropylene multilayer films. On the other hand, Figure 5d shows a large and oriented graphene with a length of approximately 600 nm. Although there are some stacks of graphene nanoplatelets, roughly 60 layers of graphene with a total thickness of 20 nm, the stacks of graphene can still be confined in the thin layers (30-40 nm thick). It is also possible that the thick-looking graphene nanoplatelets are not stacks of graphene, but rather tilted platelets.

It should be noted that the length of the graphene nanoplatelets is, in any case, smaller than the data provided by the suppliers, but the observed particles may not be totally flat (since thickness, on the contrary appears greater than the supplier provided information. Extrusion is also known to result in the shortening and breakage of nanofibers and nanoplatelets so this is not unexpected.³⁶

As seen in figure 5, it is difficult to give an average aspect ratio for the graphene nanoplatelets, due to the variety of shapes, lengths and thicknesses, the precision of the apparatus, and the relatively small scale of the pictures. To obtain more quantitative information concerning the size and orientation of the nanoplatelets, indirect scattering methods could unfortunately not be performed because the graphene concentrations in the samples are too low for simple scattering characterization. In consequence we can approximate the aspect ratio assuming the graphene thickness is 2-10 nm as given by the material provider. Then the aspect ratio $A_f = \text{length} / \text{thickness}$, depending on whether one has a wrinkled or flat shape of the nanoplatelet, can be estimated to range from 5-10 (wrinkled particles) up to 100-300 (flatter ones). In the next section we compare these values of aspect ratio with estimates from mechanical reinforcement data and the Mori-Tanaka model of composite reinforcement.³⁸

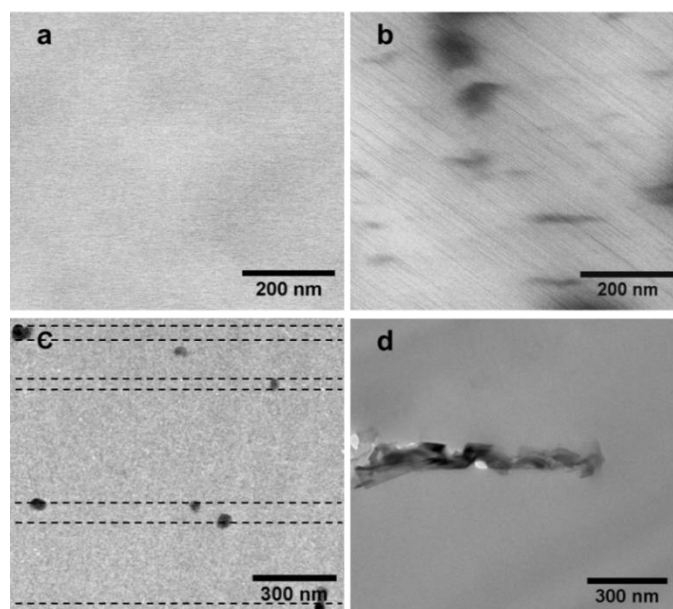


Figure 5: Cross section STEM images of 2049-layer PMMA/ PMMA film filled with (a) 0 wt%; (b) 1.0 wt% graphene; TEM images of 2049-layer PMMA/PMMA film filled with 2.0 wt% graphene (c) showing graphene confinement (dashed lines represent the tentative positions of the thin PMMA layers) (d) showing a single aligned graphene particle.

Polymers are frequently used at ambient temperature or above and this can be a high fraction of the glass transition temperature.³⁹ Because of this a change in T_g can impact the thermoviscoelastic response of the polymer matrix significantly.^{30, 39} Hence it is important to establish that any observed stiffness increase in a nanocomposite relative to the neat resin is not simply the result of an increased T_g . For example, a 16 °C increase in T_g in poly(ethyl methacrylate) (PEMA) with 0.25 wt% graphene oxide gives an apparent 25 % reinforcement at room temperature, and this could be mistaken for a large graphene oxide reinforcement.³⁰ Therefore to quantitatively study the reinforcement of the planar oriented graphene, the glass transition temperatures of samples taken so that they comprised the entire film thickness were studied by DSC and normalized heat capacity was determined to compare T_g variations.⁴⁰ As shown in Figure 6, the T_g is observed to increase by approximately 1.5-2 °C upon the addition of 2 wt% graphene. Hence the shift of the T_g due to the presence of graphene in the present work is small, unlike previous work with the nanocomposites of PEMA/graphene oxide.³⁰ Subsequently, we show that this small change of T_g results in only modest apparent reinforcement and that most of the reinforcement observed in the present work occurs due to the oriented graphene and not to the change in T_g due to confining effects of the nanofillers.

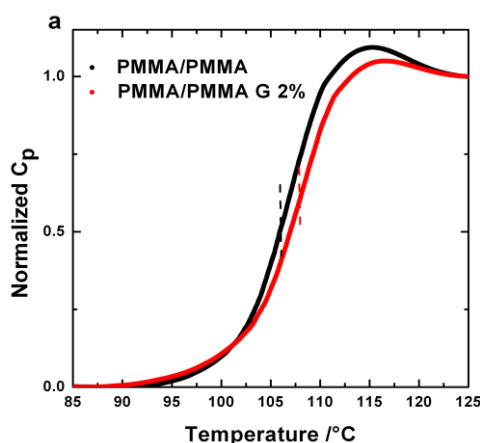


Figure 6: DSC results for the 2049L PMMA/PMMA-graphene. Reinforcing layers contain 2 wt% graphene.

From the microscopy we can see that, as we hypothesized, the forced assembly method succeeds in orienting, to some extent, the graphene in the plane of the layers. Therefore, in the direction of the orientation, nanocomposites with such structures should provide enhanced stiffening of the composites in the plane directions in which the graphene platelets are aligned. To confirm the microscopic observations, we examine the stiffening or reinforcement of the multilayer composites in two ways. We first considered the modulus of the multilayer films, themselves. The results show, in this case, modest reinforcement because the individual reinforcing elements (individual layers filled with graphene) make up only 10 % of the film itself and, so, are effectively diluted. We, therefore, then analyzed the results by estimating properties of the single, graphene-filled, layers. We have also analyzed the experimental results within the framework of the Mori-Tanaka model which gives an additional estimate of the graphene platelet aspect ratio. This was found to be in the same range as the estimates obtained from the microscopy measurements for flatter nanoplatelets.

The relative stiffening of the multilayer films along extrusion flow direction was measured based on the quasi-static tension tests and dynamic mechanical tests, respectively. From the quasi-static tension tests, we see that as the addition of graphene increases to 0.2 wt% for the total film, the reinforcement is 11.0 % for the 2049-layer PMMA/PMMA-graphene film ($E = 3.21$ GPa) compared to 2.89 GPa for the corresponding unfilled multilayer film. As expected, the reinforcement due to the graphene in the 2049-layer film is greater than in 129-layer and 3-layer films, consistent with the idea that increasing the number of layers improves the graphene orientation. From Figure 7b we see that the DMA results give a similar trend, but somewhat weaker than the quasi-static tension test, i.e., approximately 8 % increase in modulus for the 0.2 % graphene in PMMA/PMMA system. The slight difference can possibly be explained because the DMA tests were performed at 1.0 Hz and 40 °C while the static tension tests were performed at a rather low strain rate of 7.6×10^{-4} /s and at room temperature. In addition, in fracture toughness tests (data not shown), up to 0.2 wt% graphene, the brittleness of the films does not change significantly.

From the measurements on the multilayer films, we can estimate the modulus of the actual single, graphene filled layer (see equation 2). Although the microscopy was not conclusive that there are distinct filled/unfilled layers in the PMMA/PMMA-graphene system, it is still reasonable to assume, in a first order approximation, that the graphene nanoplatelets are mainly confined within the thin PMMA layers and aligned in the flow direction. Such an assumption is reasonable because of the short residence time of the melt streams and slow diffusion of the graphene nanoplatelets in the mixing elements (~ 2 minutes). Using the Stokes-Einstein equation and an equivalent spherical diameter⁴¹ for the graphene nanoplatelets, the mean-square diffusion displacement in 2 minutes is estimated to be in the 20-30 nm range for a melt viscosity of 5370 Pa.s at a temperature of 225°C. Considering the concentration of graphene, the system is not a dilute dispersion, and we would, therefore, expect that the particle diffusion should be slower than the Stokes-Einstein estimate because of the particle interactions.⁴² In addition, even if there are stacks of graphene, the larger particles should have even slower diffusion than the simple Stokes-Einstein estimates above.

The examination of the reinforcement of the single PMMA layer containing the graphene, and the comparison with micromechanical predictions assuming alignment of the nanoplatelets, provides us with insight into the advantages of the forced assembly in orienting the graphene. It also provides information about the efficiency of orientation within the single layers. This is particularly relevant if one can eventually make multilayer systems in which all of the layers are of nanometer thickness and reinforced by graphene.

The tensile modulus E_{single} of a single graphene filled PMMA layer can be estimated using equation 2, which corresponds to the results from the Voigt upper bound mixing rule,⁴³ where V_{thick} and V_{single} are the volume fraction of the unfilled thick PMMA layers and single graphene filled PMMA layers, respectively.

$$E_{single} = \frac{E - V_{thick} E_m}{V_{single}} \quad (\text{Eq. 3})$$

In order to obtain further insight into the single layer reinforcement, we used the Mori-Tanaka model³⁸ to analyze the graphene reinforcement in the single filled PMMA layer. Tandon and Weng⁴⁴ have derived an analytical form of the Mori-Tanaka model for the tensile modulus in composites with unidirectionally aligned isotropic platelets:

$$\frac{E}{E_m} = \frac{1}{(1 + V_f(-2V_m A_3 - (1 - V_m A_4 + (1 + V_m) A_5 A)))/2A)} \quad (\text{Eq. 4})$$

where E_m , ν_m , and V_f are tensile modulus of PMMA, Poisson's ratio of PMMA and volume fraction of graphene, respectively. A and A_i are functions of V_f , ν_m and the Eshelby tensors provided by Tandon and Weng.⁴⁴ In the case of the single layer, $E_{single} = E$. We have assumed $E_m = 2.89$ GPa, $\nu_m = 0.35$, and the tensile modulus of the graphene sheet was taken as 1060 GPa (value measured by nanoindentation)⁴⁵. At low volume fraction, the Mori-Tanaka model is insensitive to the Poisson's ratio of the filler and we have assumed that graphene is isotropic with a Poisson's ratio of 0.006.³⁴

In Figure 7, for the case of the 2 wt% graphene in the individual layer, the degree of apparent reinforcement is 118 % (from the quasi-static tension tests) and 86 % (from the DMA results). These results are close to the predictions from the Mori-Tanaka model with $A_f = 225$ or 137, for quasi-static or DMA testing, respectively. This is similar to values from 100 to 300 estimated from the electron microscopy images described previously for the flatter nanoplatelets. The high amount of reinforcement is significantly greater than previously reported for reinforcements in isotropic or random dispersions of graphene in polymer matrices. For example, a 2 wt% graphene dispersed in PMMA by *in situ* polymerization gave a 39 % reinforcement⁴⁶ and a 2 wt% graphene dispersed in polycarbonate by melt mixing gave a 21 % reinforcement.²⁷ Importantly, the single layer analysis shows that we achieve significant reinforcement in the polymer by orientation induced by forced assembly.

With regard to the small increase in T_g , we modified the mechanical results versus temperature to give corrected reinforcement $E(T-T_g)/E_m(T-T_g)$,³⁰ and also compared the results with the Mori-Tanaka model. In that case the fitting parameter A_f gave values of 180 and 102 for quasi-static and DMA experiments respectively, as shown in Figure 7, again in the range of the estimated A_f values for aligned nanoplatelets, obtained from the electron microscopy images. For the 2 wt% graphene in the filled layer, the reinforcement is 101 % (from quasi-static tension test) or 69 % (from DMA), still higher than previously reported reinforcements in isotropic or random dispersions. A point worth making here is that comparison of the corrected reinforcement with the apparent reinforcement shows that there is an extra 15-20 % reinforcement that arises from the relatively small change in T_g .

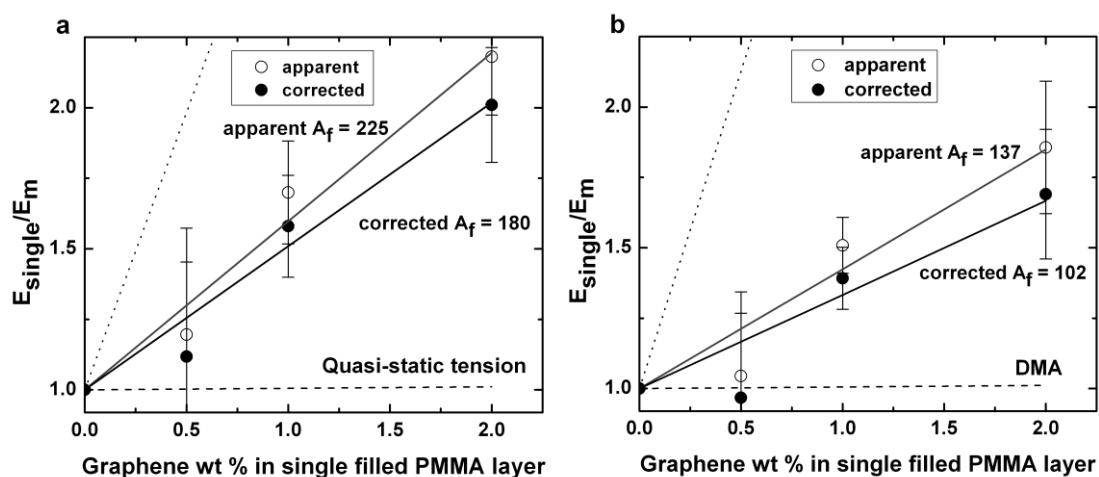


Figure 7: Experimental reinforcement and Mori-Tanaka calculations for the single graphene filled PMMA layers for 2049-layer PMMA/PMMA films. (Open circles: apparent reinforcement; Filled circles: corrected for changing T_g ; Solid line: Mori-Tanaka prediction; Dotted line: Voigt upper bound; Dashed line: Reuss lower bound. Both of these bounds are estimated from the moduli of graphene and neat PMMA).

We have also examined the two-dimensional reinforcement in the single layer from the measurements of modulus perpendicular to the extrusion direction. Indeed, when the film leaves the extruder, its thickness is close to 1mm, whereas the final film thickness obtained after the chill-roll is between 0.3 and 0.5mm, indicating orientation of the polymer chains. A point of importance here is that annealing of the samples above T_g and watching them de-orient, gives the result that the deorientation is approximately the same for the graphene filled and unfilled system. We interpret this to imply that the addition of the graphene does not significantly change the orientation of polymer chains induced by the multilayer extrusion process. Hence, we can compare the reinforcement relative to the neat resin properties using the extruded film estimates and the neat PMMA/PMMA multilayer film properties of the tensile modulus of 2.89 GPa and 2.08 GPa, along flow and transverse directions, respectively. We compare the mechanical properties by considering the tensile modulus of the single graphene filled layer, along both flow and transverse directions and see that the transverse reinforcement is weaker than that of the flow direction.

To conclude, combination of microscopic analysis of the morphology of the multilayer films and mechanical property measurements provides evidence that the reinforced layers contain oriented graphene in the direction of extrusion and partially oriented in the transverse direction. The amount of reinforcement is greater than normally reported for graphene nanocomposites and has been attributed primarily to the graphene orientation and not to the small increase in the glass transition temperature of the reinforced matrix. The lateral degree of reinforcement at the same graphene loading in the PMMA/PMMA-graphene system is approximately 75 % that of the flow direction reinforcement, leaving room for improvement in the properties in the transverse direction. The results suggest that forced assembly by multilayer extrusion offers the opportunity of creating layered structures with high degrees of in-plane reinforcement and further refinements of the method should be developed.¹

3.2. Forced self-assembly

Block copolymers have received much interest in the past decades due to their ability to self-assemble with well-defined phase separation at the nanometer scale that leads to domains of the size of few tens of nanometers, which make them very attractive for many applications (e.g. in the field of nanoelectronics, nanolithography, biosensors, optoelectronics, membranes, holographic gratings, etc.).^{47, 48} These engineering applications demand control over the orientation and the position of the nanodomains. However, during the self-assembling process, nanodomains nucleate randomly and grow as a polygrain texture with a periodical order maintained only over few micrometers. To overcome this lack of order at the macroscale and induce nanodomain orientation and ordering, external stimuli have been successfully used. Several methods, such as solvent or temperature annealing sometimes combined with shearing, are commonly employed efficiently to create long-range ordering in thin films or in the bulk.^{44, 49}

Recently, the “forced assembly” technique that is multilayer coextrusion has been used by Korley et al. to confine spherical and cylindrical ABA triblock copolymer.⁵⁰⁻⁵³ These studies mainly focus on the relationship between the nanostructure and the mechanical properties of the resulting films, while the extrusion was carried out at a temperature below the order-disorder transition temperature (T_{ODT}). Flow orientation and confinement induced by multilayer coextrusion creates long-range ordering of cylinders in the extrusion

direction. The best ordering has been obtained for the thinnest layers after annealing (performed at a temperature above T_g of the major block and below T_{ODT}).

Because of the three chemically different blocks, ABC triblock terpolymers can lead to a larger set of microstructure morphologies and allows the creation of original patterns.⁵⁴ Experimentally, poly(styrene-*b*-butadiene-*b*-methyl methacrylate) (SBM) morphologies were thoroughly studied by Stadler et al.: lamellar, knitting, dotted-cylinders, cylinder-within-cylinders, spheres-on-spheres morphologies peculiar to ABC copolymers have been successfully observed.⁵⁵⁻⁵⁷

Here we describe a direct and scalable method to produce large quantities of a hierarchical material presenting a double organization of the matter at the nano and the microscale, by using the multilayer coextrusion process, without additional thermal annealing, to confine and self-assemble SBM. This contribution helps to demonstrate that processing parameters, especially the draw ratio, are important in the improvement of the ordering process of the SBM copolymer morphology.

Polycarbonate 121R (PC) was purchased from Sabic and used as received (confining polymer). Its melt flow index is 21 g / 10 min (300 °C), as provided by Sabic. Its glass temperature transition is 153 °C, M_w is 40 kg.mol⁻¹ ($\bar{D} = 2.2$). Poly(styrene-*b*-butadiene-*b*-methyl methacrylate) E20 (SBM, PS-PB-PMMA) triblock copolymer was gratefully supplied by Arkema and used as received without further purification. Due to the synthesis method, the product is actually a blend of PS-PB (SB) and SBM. Through gel permeation chromatography and ¹H NMR measurements, the product as provided by Arkema was characterized as following: $M_n = 100$ kg.mol⁻¹ ($\bar{D} = 1.1$) for the triblock and $M_n = 50$ kg.mol⁻¹ ($\bar{D} = 1.05$) for the diblock, with 55 mol % of SBM and 45 mol % of SB in the sample. The composition of the triblock is close to 25 kg.mol⁻¹, 25 kg.mol⁻¹, and 50 kg.mol⁻¹ for the PS, PB and PMMA blocks respectively while the diblock is 25 kg.mol⁻¹ and 25 kg.mol⁻¹ for PS and PB. In consequence, the composition of triblock itself is actually close to 25-25-50 (wt%) though the composition of the whole product is 33-33-33 (wt%).

Prior to extrusion, SBM and PC pellets were dried respectively at 80 °C for 3 h and 120 °C for 4 h. The PC grade was chosen so that the viscosity of the two polymers matches at the processing temperature (240 °C) and shear rate (5-20 s⁻¹). In this range of shear rates, the viscosity ratio lies between 0.5 and 2, as measured by rheology. Films were prepared as described previously, with in this case two 20 mm single screw extruders. The triblock is extruded at 240 °C and the PC at 300 °C, the multiplying elements block being set at 240 °C. At this temperature, the block copolymer is still self-assembled and does not flow as a homopolymer since the elastic contribution (G') of the dynamic modulus is higher than the viscous one (G'') as rheological measurements revealed (i.e. the triblock is extruded below its order-disorder transition temperature T_{ODT}). Depending on the targeted thickness of the confined SBM layer, 7 (257 total layers) or 9 (1025 layers) multiplying elements were used. After the flat die, the films were drawn with a chill roll at 120 °C. Draw ratio (Dr) is varied from 1 to 11.

Figure 8 shows TEM micrographs of the confined SBM layers cross-sections as a function of thickness at Dr = 2, Dr = 8, and Dr = 11. It is interesting to see that continuous layers can be achieved though SBM has a storage modulus higher than its loss modulus during the extrusion. It also shows the transverse direction of films made at Dr = 11. The periodical thickness of the block copolymer morphology appears to be around 50 nm, which is quite similar to what has been previously reported in the literature for such material.⁵⁵⁻⁵⁷ As the confined layer thickness decreases from 200 to 100 nm, the number of block copolymer periods in the confined layer decreases from 4 to 2. At low Dr, the morphology seems to be locally disordered, even though one can guess a

global orientation of the morphology along the interfaces. Qualitatively, a better organization of the nanodomains is seen at high Dr , but also for decreasing layer thicknesses.

The morphology of the triblock copolymer is hard to determine with the TEM micrographs. It seems that both lamellae (PS and PB) and cylinders (or nodules, PMMA) are observed in Figure 3. The presence of SB diblock copolymer in the melt could lead to a mixed and therefore complex morphology. At these compositions, both copolymers (SB and SBM) should have a lamellar morphology. Cylinders-in-lamellae, lamellae with fluctuations or double gyroid can then be observed with slight blend composition variations.⁵⁸ The PC-SBM interfaces influence the alignment of the morphology: parallel lamellae clearly appear at the interface due to a preferential wetting towards the polycarbonate layers (see Figure 8). Besides, at high draw ratio, the lamellar structure at the interface is more pronounced and within the layer, the arrangement of the morphology appears also more regular even for thicker layers. When probing the transverse direction, it appears that fewer nodules are observed in this direction and that the morphology is less ordered. It can also be noticed that the interface is less stable, showing some fluctuations that are not seen in the cross-section image, which can be attributed to flow fluctuations during extrusion.

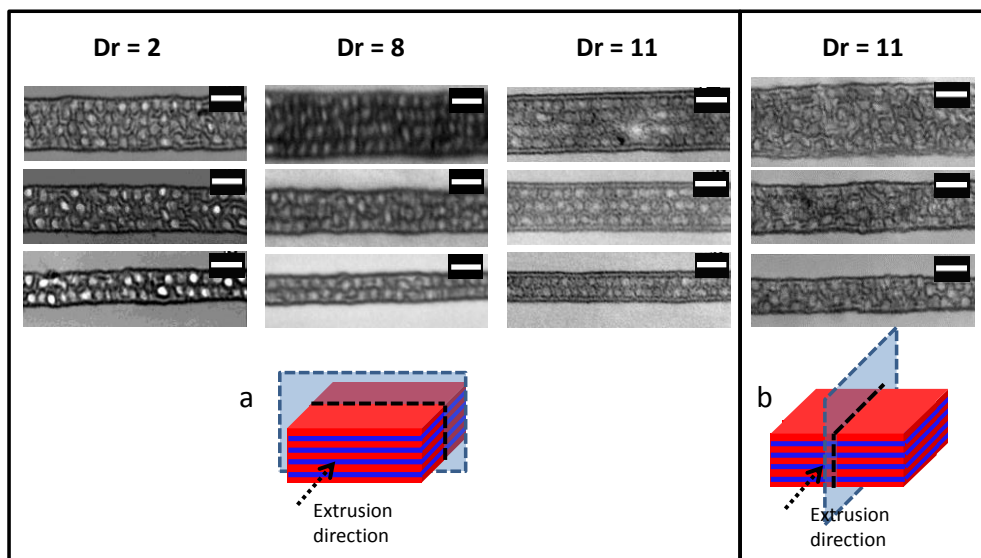


Figure 8: Bright field transmission electron micrographs of SBM confined layers of different thicknesses at a draw ratio (Dr) of 2, 8 (cross-section) and 11 (cross-section, transverse). Scale bars = 100 nm. The schemes illustrate the film section observation: cross-section (a) and transverse (b).

At the interface between the PC layer and the SBM, a black region can be observed and attributed to the PB phase. This black region takes the shape of a well-defined line at high draw ratios, perfectly parallel to the interface. To explain the interface in the case of PC/SBM multilayered films, the solubility parameters were used to calculate the Flory-Huggins parameters χ of each polymer pairs by using the approach based on Hildebrand solubility parameters, due to the lack of experimental data concerning polybutadiene (and despite the fact this method is certainly not well suited for this purpose, as explained in chapter 1).⁵⁹⁻⁶¹

$$\chi = \frac{V_{AB}}{RT} (\delta_A - \delta_B)^2 \quad (\text{Eq. 5})$$

where V_{AB} is the geometric mean of molar volumes of polymer A and polymer B, R is the universal gas constant (8.314 J/K/mol), T is the processing temperature, δ_A and δ_B are the solubility parameters of polymer A and polymer B, respectively.

From this approach, we determined the PB phase has the smallest affinity with PC. In contrast, PMMA is most likely the block in contact with the PC layer. Even though OsO_4 staining for TEM observations does not allow the contrast between PC and PMMA to be seen, it is then reasonable to assume a PC-PMMA interface. The well-aligned PB layer can then be the consequence of the PMMA “adaptive layer”, which accommodate the interface, as observed for block copolymer thin films.⁶²

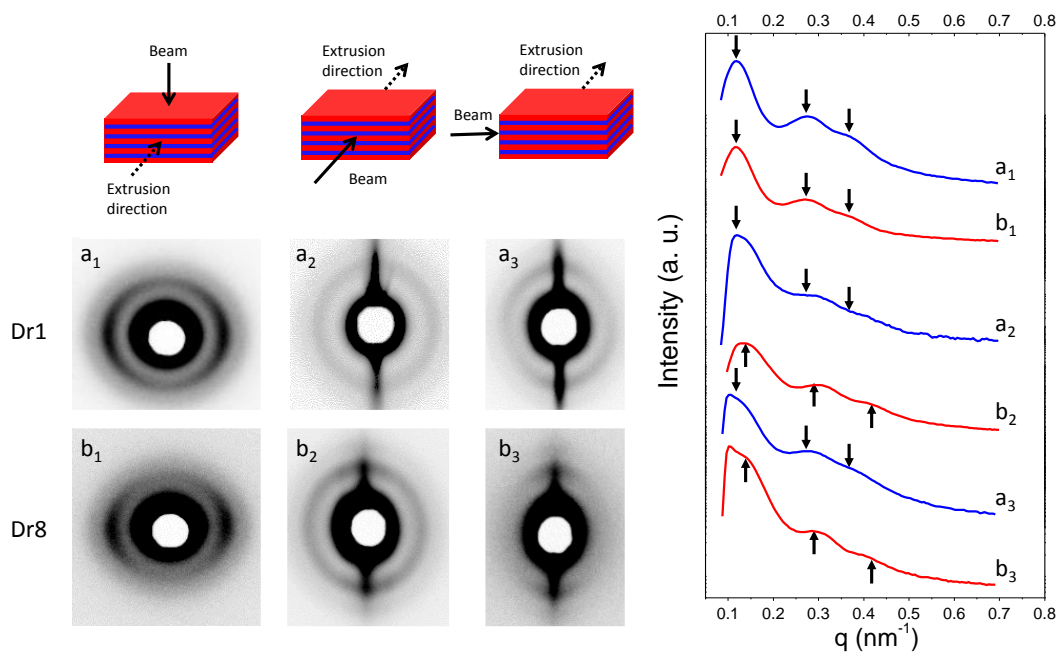


Figure 10: SAXS patterns of PC/SBM films drawn at $Dr = 1$ (a), and $Dr = 8$ (b) performed in the normal (₁), extrusion (₂), and transverse directions (₃). The schemes show the orientation of the multilayered films relative to the X-Ray beam. Integrations of the SAXS patterns along Φ of PC/SBM films with $Dr = 1$ (a) and $Dr = 8$ (b) near the equatorial region (a_1, b_1) and near the meridian region (a_{2-3}, b_{2-3}) are shown on the graph. Arrows indicate relative position of the peaks. Downward and upward arrows indicate the same position.

SAXS experiments have been performed on both the normal and the extrusion directions of the films to evaluate more quantitatively the degree of organization of the triblock copolymer morphology under confinement and, especially, the effect of the draw ratio. Figure 9 compares scattering patterns of films drawn at $Dr = 1$ and $Dr = 8$ to show the influence of the draw ratio on the organization of the morphology. As the draw ratio is increased, in the normal orientation, the ellipsoidal shape becomes even clearer with its longer axis being more intense along the equator. This can be attributed to the orientation of the morphology induced by stretching during drawing. This behavior resembles to what was observed for cylindrical block copolymer being unidirectionally stretched.⁶³

For curve b_1 , the first peak is also at 0.12 nm^{-1} , corresponding to a scattering domain size of 52 nm. This value is very close to the block copolymer period observed by TEM. A slight shift is also observed for the extrusion direction (curves b_2, b_3) and can be attributed to a squeeze or a stretching of the morphology ($q^* = 0.14 \text{ nm}^{-1}$, $d_0 = 44 \text{ nm}$). A scattering pattern along the meridional axis is observed for both the extrusion and the transverse directions and the integration shows q^* , $2q^*$ and $3q^*$ peaks, which is characteristic of a lamellar morphology. At low Dr , the 2nd and 3rd order are not very intense but becomes more intense at higher Dr , which indicates a better alignment of the lamellae in the stretched film and confirms the observations made by TEM. This ordering is then due to a combination of the stretching and the greater influence of the interfaces of the confining layers. For the layered films oriented in the transverse and the extrusion directions, a strong meridional streak can be observed in the scattering patterns. This could arise from the interfaces between the PC and the SBM layers, as it was observed for PP/PS multilayered films.⁶⁴

SBM triblock copolymer has been successfully confined with polycarbonate through multilayer coextrusion. We showed that despite performing extrusion below T_{ODT} of the SBM, continuous self-assembled structures can be achieved without any further post-treatment such as annealing. We also evidenced, for the first time, long-range ordering for these “as extruded” materials, which, though imperfect, can be improved by increasing the draw ratio after extrusion and decreasing the SBM layer thickness.² This industrially scalable and simple technique allows the continuous fabrication of hierarchically organized films that can be of interest for innovative mechanically-reinforced materials or other engineering applications where long-range ordering of the nanodomains is necessary for large quantities of material.

This study has been extended in Juan-Sebastian Montana PhD work to another triblock copolymer, in that case a symmetric one, poly(methylmethacrylate) – b – poly(nbutylacrylate) – b – poly(methylmethacrylate) (MAM) also commercialized by Arkema (Nanostrength®) for impact resistance improvement of brittle amorphous polymers such as PMMA (defense expected in 2017). It is usually dry-blended with PMMA at 20 to 40 wt% so that the rubbery phase (butylacrylate) represents between 10 to 20 wt% of the blend. Methylmethacrylate and butylacrylate phases are immiscible and nanodomains are then created upon processing. Though the final morphology adopted by the block copolymer could impact the toughening, it is impossible to master via conventional processing.

Forced assembly coextrusion has then been used to produce multilayer films of MAM confined by PMMA at 10-90 and 30-70 wt%. Films having from 513 to 2049 layers have been obtained by fixing the number of mixing elements (from 8 to 10). Draw ratios were again varied using a chill roll to tune the thicknesses of the confined layers from 25 to 500 nm. Films containing alternating layers of PMMA and confined self-assembled block copolymers were directly obtained without additional annealing due to an order-disorder transition temperature (T_{ODT}) of the MAM again well above the processing temperature. In this work a cylindrical morphology for the confined nanolayer coextruded MAM has been identified, different from the lamellar morphology obtained at thermodynamic equilibrium when MAM is confined (see figure 11).

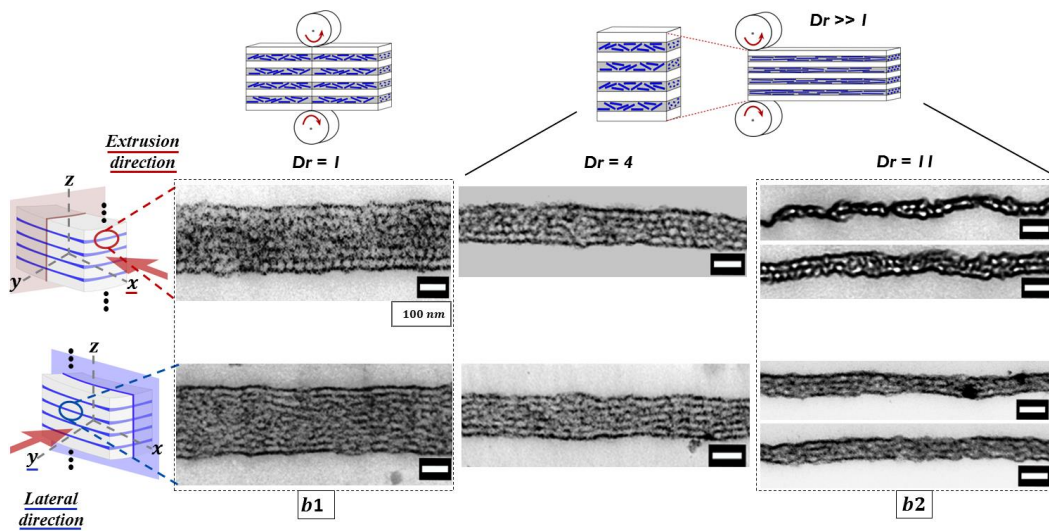


Figure 11: Transmission electron microscopy cross-section images of an extruded film containing confined MAM layers by PMMA at different layer thicknesses (scale bar = 1 μm). The contrast is induced by staining with RuO_4 (the butyl acrylate block appears dark in the micrograph).

Differences between 8 LME and 9 LME films have been observed in the SAXS results. The cylinder-cylinder distance ($d=2\pi/q$) changes for the 9 LME films in two of the three main directions as described in Figure 12b. By scanning the lateral direction, it is observed that q values of the maximum intensity peaks increase at high Dr, which means lower distances d . On the contrary, by scanning the transverse direction, it is observed that q values of the maximum intensity peaks decrease at high Dr, which means higher distances d . However, this is not the case for 8 LME films. These results show that the morphology orientation and order are influenced by the processing parameters. We assume that the way in which the block copolymer is confined plays a predominant role in the final geometry of the nanostructured morphology. Though not explained at the moment, at equivalent BCP layer thickness, it seems that in the 9 LME films the BCP is more sensitive to the confinement.

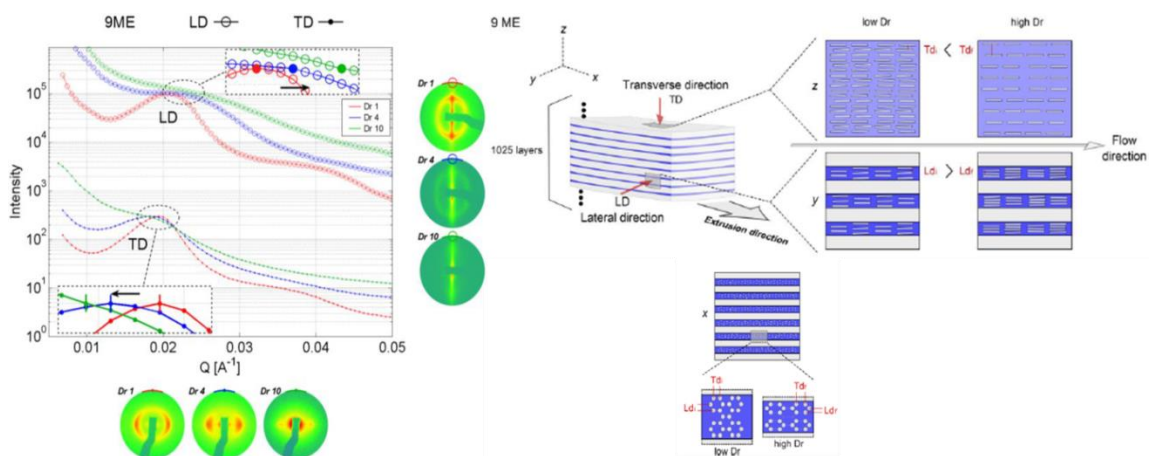


Figure 12: SAXS patterns in lateral direction and transverse direction of MAM confined by PMMA films obtained at different Dr (left). Schematic of d evolution in a 9 ME film (right).

The toughness of the multilayered films with 30 wt% MAM are then compared to dry-blended PMMA/MAM films (pellets of the two materials being simply mixed with each other before extrusion). As a first estimate, the fracture toughness is defined here as the integral of the stress-strain curve. It can be seen in figure 13 that 30 wt% MAM improves the fracture toughness roughly by a factor of 10 in the lateral direction and by a factor of 20 in the extrusion direction when dry-blended with PMMA. This toughness is further increased by a factor of 2 to 3 when comparing multilayered films to blended films. It is believed that the higher degree of organization achieved in multilayered films is responsible for these enhanced mechanical properties. Studies are on the way to confirm this hypothesis.

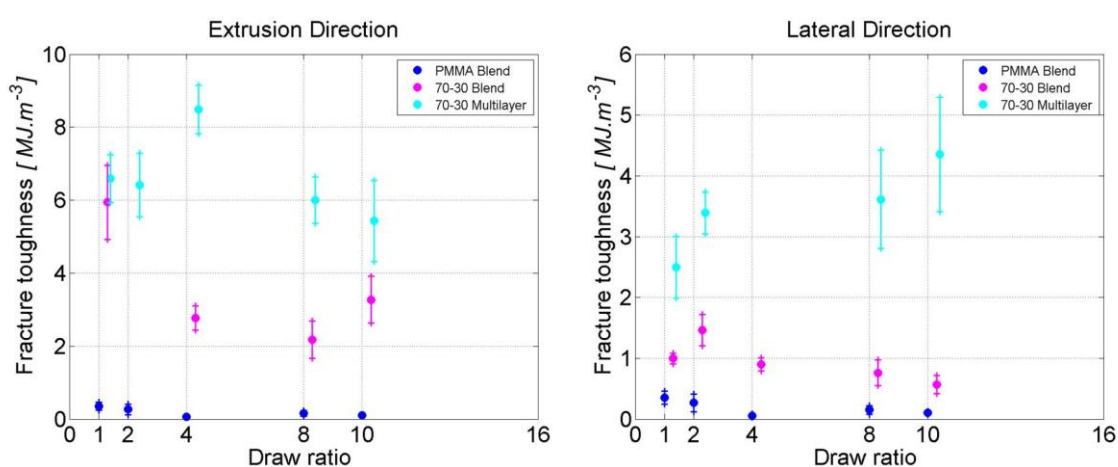


Figure 13: Fracture toughness as a function of the draw ratio for neat PMMA, dry-blended films with 30 wt% MAM and multilayered films with 30 wt% MAM and 9 LME.

3.3. Conclusion and future work

Several collaborative studies presented in this chapter have illustrated the potential of nanolayer coextrusion to design innovative polymeric materials, such as nanocomposites presenting improved mechanical properties due to enhanced dispersion and distribution of the nanofillers, or as an effective way to control the self-assembly of copolymers for impact resistance applications. One field of research that has not been detailed here is the development of hyperbarrier properties. As already observed by Baer (see chapter 1), nanoconfinement can impact the crystalline morphology of specific polymers which can in turn lead to improved barrier properties. Two recent studies in the group have obtained similar conclusions on poly(lactic acid)⁶⁵ and nylon-MXD6⁶. Further studies on hyperbarrier materials will consist in combining these confinement effects on crystallization with the dispersion and distribution of nanoplatelets. Concerning forced self-assembly, as stated above, a better understanding of the link between morphology and resulting mechanical properties is still needed.

3.4. References

1. Li, X.; McKenna, G. B.; Miquelard-Garnier, G.; Guinault, A.; Sollogoub, C.; Regnier, G.; Rozanski, A., Forced assembly by multilayer coextrusion to create oriented graphene reinforced polymer nanocomposites. *Polymer* **2014**, 55, (1), 248-257.
2. Roland, S.; Miquelard-Garnier, G.; Gervais, M.; Guinault, A.; Sollogoub, C., Controlling the order of triblock copolymer via confinement induced by forced self-assembly. *Materials Today Communications* **2016**, 6, 37-43.
3. Miquelard-Garnier, G., Guinault A., Sollogoub C., Delalande S., Fromonteil D. Procédé d'élaboration d'un matériau composite thermoplastique renforcé par des nanotubes de carbone. French Patent FR2995815 (B1) — **2016**
4. Miquelard-Garnier, G.; Guinault, A.; Fromonteil, D.; Delalande, S.; Sollogoub, C., Dispersion of carbon nanotubes in polypropylene via multilayer coextrusion: Influence on the mechanical properties. *Polymer* **2013**, 54, (16), 4290-4297.
5. Boufarguine, M.; Guinault, A.; Miquelard-Garnier, G.; Sollogoub, C., PLA/PHBV Films with Improved Mechanical and Gas Barrier Properties. *Macromolecular Materials and Engineering* **2013**, 298, (10), 1065-1073.
6. Messin, T.; Follain, N. g.; Guinault, A.; Miquelard-Garnier, G.; Sollogoub, C.; Delpouve, N.; Gaucher, V. r.; Marais, S. p., Confinement effect in PC/MXD6 multilayer films: Impact of the microlayered structure on water and gas barrier properties. *Journal of Membrane Science* **2017**, 525, 135-145.
7. Paul, D. R.; Robeson, L. M., Polymer nanotechnology: Nanocomposites. *Polymer* **2008**, 49, (15), 3187-3204.
8. Spitalsky, Z.; Tasis, D.; Papagelis, K.; Galiotis, C., Carbon nanotube-polymer composites: Chemistry, processing, mechanical and electrical properties. *Progress in Polymer Science* **2010**, 35, (3), 357-401.
9. Coleman, J. N.; Khan, U.; Blau, W. J.; Gun'ko, Y. K., Small but strong: A review of the mechanical properties of carbon nanotube-polymer composites. *Carbon* **2006**, 44, (9), 1624-1652.
10. Coleman, J. N.; Khan, U.; Gun'ko, Y. K., Mechanical reinforcement of polymers using carbon nanotubes. *Advanced Materials* **2006**, 18, (6), 689-706.
11. Masuda, J.; Torkelson, J. M., Dispersion and major property enhancements in polymer/multiwall carbon nanotube nanocomposites via solid-state shear pulverization followed by melt mixing. *Macromolecules* **2008**, 41, (16), 5974-5977.
12. Brunner, P. J.; Clark, J. T.; Torkelson, J. M.; Wakabayashi, K., Processing-structure-property relationships in solid-state shear pulverization: Parametric study of specific energy. *Polymer Engineering and Science* **2012**, 52, (7), 1555-1564.
13. Pujari, S.; Ramanathan, T.; Kasimatis, K.; Masuda, J.; Andrews, R.; Torkelson, J. M.; Brinson, L. C.; Burghardt, W. R., Preparation and Characterization of Multiwalled Carbon Nanotube Dispersions in Polypropylene: Melt Mixing Versus Solid-State Shear Pulverization. *Journal of Polymer Science Part B-Polymer Physics* **2009**, 47, (14), 1426-1436.
14. Villmow, T.; Potschke, P.; Pegel, S.; Haussler, L.; Kretzschmar, B., Influence of twin-screw extrusion conditions on the dispersion of multi-walled carbon nanotubes in a poly(lactic acid) matrix. *Polymer* **2008**, 49, (16), 3500-3509.
15. Kasaliwal, G. R.; Pegel, S.; Goldel, A.; Potschke, P.; Heinrich, G., Analysis of agglomerate dispersion mechanisms of multiwalled carbon nanotubes during melt mixing in polycarbonate. *Polymer* **2010**, 51, (12), 2708-2720.
16. Villmow, T.; Kretzschmar, B.; Potschke, P., Influence of screw configuration, residence time, and specific mechanical energy in twin-screw extrusion of polycaprolactone/multi-walled carbon nanotube composites. *Composites Science and Technology* **2010**, 70, (14), 2045-2055.
17. Kasaliwal, G. R.; Goldel, A.; Potschke, P.; Heinrich, G., Influences of polymer matrix melt viscosity and molecular weight on MWCNT agglomerate dispersion. *Polymer* **2011**, 52, (4), 1027-1036.
18. Jimenez, G. A.; Jana, S. C., Electrically conductive polymer nanocomposites of polymethylmethacrylate and carbon nanofibers prepared by chaotic mixing. *Composites Part a-Applied Science and Manufacturing* **2007**, 38, (3), 983-993.
19. Jimenez, G. A.; Jana, S. C., Oxidized carbon nanofiber/polymer composites prepared by chaotic mixing. *Carbon* **2007**, 45, (10), 2079-2091.
20. Shen, J. B.; Li, J.; Guo, S. Y., The distribution and morphological evolution of dispersed phase in laminating-multiplying elements during extrusion. *Polymer Composites* **2012**, 33, (5), 693-699.

21. Wen, M.; Sun, X. J.; Su, L.; Shen, J. B.; Li, J.; Guo, S. Y., The electrical conductivity of carbon nanotube/carbon black/polypropylene composites prepared through multistage stretching extrusion. *Polymer* **2012**, 53, (7), 1602-1610.
22. Micusik, M.; Omastova, M.; Krupa, I.; Prokes, J.; Pissis, P.; Logakis, E.; Pandis, C.; Potschke, P.; Pionteck, J., A Comparative Study on the Electrical and Mechanical Behaviour of Multi-Walled Carbon Nanotube Composites Prepared by Diluting a Masterbatch With Various Types of Polypropylenes. *Journal of Applied Polymer Science* **2009**, 113, (4), 2536-2551.
23. Muller, M. T.; Krause, B.; Potschke, P., A successful approach to disperse MWCNTs in polyethylene by melt mixing using polyethylene glycol as additive. *Polymer* **2012**, 53, (15), 3079-3083.
24. Manchado, M. A. L.; Valentini, L.; Biagiotti, J.; Kenny, J. M., Thermal and mechanical properties of single-walled carbon nano tubes-polypropylene composites prepared by melt processing. *Carbon* **2005**, 43, (7), 1499-1505.
25. Halpin, J. C.; Kardos, J. L., Halpin-Tsai equations: a review. *Polymer Engineering and Science* **1976**, 16, (5), 344-352.
26. Potts, J. R.; Murali, S.; Zhu, Y.; Zhao, X.; Ruoff, R. S., Microwave-Exfoliated Graphite Oxide/Polycarbonate Composites. *Macromolecules* **2011**, 44, (16), 6488-6495.
27. Padawer, G. E.; Beecher, N., On the strength and stiffness of planar reinforced plastic resins. *Polymer Engineering & Science* **1970**, 10, (3), 185-192.
28. Jackson, A. P.; Vincent, J. F. V.; Turner, R. M., A physical model of nacre. *Composites Science and Technology* **1989**, 36, (3), 255-266.
29. Ramanathan T.; Abdala, A. A.; Stankovich S.; Dikin, D. A.; Herrera Alonso, M.; Piner, R. D.; Adamson, D. H.; Schniepp, H. C.; Chen X.; Ruoff, R. S.; Nguyen, S. T.; Aksay, I. A.; Prud'Homme, R. K.; Brinson, L. C., Functionalized graphene sheets for polymer nanocomposites. *Nat Nano* **2008**, 3, (6), 327-331.
30. Li, X.; McKenna, G. B., Considering Viscoelastic Micromechanics for the Reinforcement of Graphene Polymer Nanocomposites. *ACS Macro Letters* **2012**, 1, (3), 388-391.
31. Kim, H.; Macosko, C. W., Processing-property relationships of polycarbonate/graphene composites. *Polymer* **2009**, 50, (15), 3797-3809.
32. Wu, H.; Rook, B.; Drzal, L. T., Dispersion optimization of exfoliated graphene nanoplatelet in polyetherimide nanocomposites: Extrusion, precoating, and solid state ball milling. *Polymer Composites* **2013**, 34, (3), 426-432.
33. Pötschke, P.; Bhattacharyya, A. R.; Janke, A., Carbon nanotube-filled polycarbonate composites produced by melt mixing and their use in blends with polyethylene. *Carbon* **2004**, 42, (5â€“6), 965-969.
34. Cho, J.; Luo, J. J.; Daniel, I. M., Mechanical characterization of graphite/epoxy nanocomposites by multi-scale analysis. *Composites Science and Technology* **2007**, 67, (11â€“12), 2399-2407.
35. Ponting, M.; Hiltner, A.; Baer, E., Polymer nanostructures by forced assembly: Process, structure, and properties. *Macromolecular Symposia* **2010**, 294, (1), 19-32.
36. Alig, I.; Pötschke, P.; Lellinger, D.; Skipa, T.; Pegel, S.; Kasaliwal, G. R.; Villmow, T., Establishment, morphology and properties of carbon nanotube networks in polymer melts. *Polymer* **2012**, 53, (1), 4-28.
37. Gupta, M.; Lin, Y.; Deans, T.; Baer, E.; Hiltner, A.; Schiraldi, D. A., Structure and Gas Barrier Properties of Poly(propylene-graft-maleic anhydride)/Phosphate Glass Composites Prepared by Microlayer Coextrusion. *Macromolecules* **2010**, 43, (9), 4230-4239.
38. Tanaka, K.; Mori, T., The hardening of crystals by non-deforming particles and fibres. *Acta Metallurgica* **1970**, 18, (8), 931-941.
39. McKenna, G. B., Dynamics of Materials at the Nanoscale: Small-Molecule Liquids and Polymer Films. In *Polymer Physics*, John Wiley & Sons, Inc.: **2010**, pp 191-223.
40. Koh, Y. P.; Simon, S. L., Structural relaxation of stacked ultrathin polystyrene films. *Journal of Polymer Science Part B: Polymer Physics* **2008**, 46, (24), 2741-2753.
41. Floquet, S. b.; Brun, S. b.; Lemonnier, J.-F. o.; Henry, M.; Delsuc, M.-A.; Prigent, Y.; Cadot, E.; Taulelle, F., Molecular Weights of Cyclic and Hollow Clusters Measured by DOSY NMR Spectroscopy. *Journal of the American Chemical Society* **2009**, 131, (47), 17254-17259.
42. Banchio, A., J.; Nägele, G.; Bergenholtz, J., Viscoelasticity and generalized Stokesâ€“Einstein relations of colloidal dispersions. *The Journal of Chemical Physics* **1999**, 111, (18), 8721-8740.
43. Liu, B.; Feng, X.; Zhang, S.-M., The effective Young's modulus of composites beyond the Voigt estimation due to the Poisson effect. *Composites Science and Technology* **2009**, 69, (13), 2198-2204.
44. Tandon, G. P.; Weng, G. J., The effect of aspect ratio of inclusions on the elastic properties of unidirectionally aligned composites. *Polymer Composites* **1984**, 5, (4), 327-333.

45. Lee, C.; Wei, X.; Kysar, J. W.; Hone, J., Measurement of the Elastic Properties and Intrinsic Strength of Monolayer Graphene. *Science* **2008**, 321, (5887), 385-388.
46. Potts, J. R.; Lee, S. H.; Alam, T. M.; An, J.; Stoller, M. D.; Piner, R. D.; Ruoff, R. S., Thermomechanical properties of chemically modified graphene/poly(methyl methacrylate) composites made by in situ polymerization. *Carbon* **2011**, 49, (8), 2615-2623.
47. Hamley, I. W., Ordering in thin films of block copolymers: Fundamentals to potential applications. *Progress in Polymer Science* **2009**, 34, (11), 1161-1210.
48. Kim, J. K.; Yang, S. Y.; Lee, Y.; Kim, Y., Functional nanomaterials based on block copolymer self-assembly. *Progress in Polymer Science* **2010**, 35, (11), 1325-1349.
49. Bang, J.; Jeong, U.; Ryu, D. Y.; Russell, T. P.; Hawker, C. J., Block Copolymer Nanolithography: Translation of Molecular Level Control to Nanoscale Patterns. *Advanced Materials* **2009**, 21, (47), 4769-4792.
50. Burt, T. M.; Jordan, A. M.; Korley, L. T. J., Toward Anisotropic Materials via Forced Assembly Coextrusion. *ACS Applied Materials & Interfaces* **2012**, 4, (10), 5155-5161.
51. Burt, T. M.; Jordan, A. M.; Korley, L. T. J., Investigating Interfacial Contributions on the Layer-Thickness-Dependent Mechanical Response of Confined Self-Assembly via Forced Assembly. *Macromolecular Chemistry and Physics* **2013**, 214, (8), 873-881.
52. Burt, T. M.; Keum, J.; Hiltner, A.; Baer, E.; Korley, L. T. J., Confinement of Elastomeric Block Copolymers via Forced Assembly Coextrusion. *ACS Applied Materials & Interfaces* **2011**, 3, (12), 4804-4811.
53. Burt, T. M.; Monemian, S.; Jordan, A. M.; Korley, L. T. J., Thin film confinement of a spherical block copolymer via forced assembly co-extrusion. *Soft Matter* **2013**, 9, (17), 4381-4385.
54. Hadjichristidis, N.; Iatrou, H.; Pitsikalis, M.; Pispas, S.; Avgeropoulos, A., Linear and non-linear triblock terpolymers. Synthesis, self-assembly in selective solvents and in bulk. *Progress in Polymer Science* **2005**, 30, (7), 725-782.
55. Breiner, U.; Krappe, U.; Thomas, E. L.; Stadler, R., Structural Characterization of the "Knitting Pattern" in Polystyrene-block-poly(ethylene-co-butylene)-block-poly(methyl methacrylate) Triblock Copolymers. *Macromolecules* **1998**, 31, (1), 135-141.
56. Stadler, R.; Auschra, C.; Beckmann, J.; Krappe, U.; Voight-Martin, I.; Leibler, L., Morphology and Thermodynamics of Symmetric Poly(A-block-B-block-C) Triblock Copolymers. *Macromolecules* **1995**, 28, (9), 3080-3097.
57. Stocker, W.; Beckmann, J.; Stadler, R.; Rabe, J. P., Surface Reconstruction of the Lamellar Morphology in a Symmetric Poly(styrene-block-butadiene-block-methyl methacrylate) Triblock Copolymer: A Tapping Mode Scanning Force Microscope Study. *Macromolecules* **1996**, 29, (23), 7502-7507.
58. Abetz, V.; Goldacker, T., Formation of superlattices via blending of block copolymers. *Macromolecular Rapid Communications* **2000**, 21, (1), 16-34.
59. Miquelard-Garnier, G.; Roland, S. b., Beware of the Flory parameter to characterize polymer-polymer interactions: A critical reexamination of the experimental literature. *European Polymer Journal* **84**, 111-124.
60. Van Krevelen, D. W.; Te Nijenhuis, K., Chapter 7 - Cohesive Properties and Solubility. In *Properties of Polymers (Fourth Edition)*, Elsevier: Amsterdam, **2009**; pp 189-227.
61. Brandrup, J.; Immergut, E. H.; Grulke, E. A., *Polymer Handbook, 4th Edition*. Wiley: **2003**.
62. Roland, S. b.; Gaspard, D.; Prud'homme, R. E.; Bazuin, C. G., Morphology Evolution in Slowly Dip-Coated Supramolecular PS-b-P4VP Thin Films. *Macromolecules* **2012**, 45, (13), 5463-5476.
63. McCready, E. M.; Burghardt, W. R., In Situ SAXS Studies of Structural Relaxation of an Ordered Block Copolymer Melt Following Cessation of Uniaxial Extensional Flow. *Macromolecules* **2015**, 48, (1), 264-271.
64. Jin, Y.; Rogunova, M.; Hiltner, A.; Baer, E.; Nowacki, R.; Galeski, A.; Piorkowska, E., Structure of polypropylene crystallized in confined nanolayers. *Journal of Polymer Science Part B-Polymer Physics* **2004**, 42, (18), 3380-3396.
65. Fernandes Nassar, S.; Guinault, A.; Delpouve, N.; Divry, V. r.; Ducruet, V.; Sollogoub, C.; Domenek, S., Multi-scale analysis of the impact of polylactide morphology on gas barrier properties. *Polymer* **2017**, 108, 163-172.

Chapter 4

Control of elastomeric interfaces

(this chapter describes results that were obtained during my post-doctorate with Prof. Alfred J. Crosby at University of Massachusetts and related work done during the WAFPI project - wetting, adhesion and friction of patterned interfaces- that was coordinated by Christophe Poulard at the Laboratoire de Physique des Solides. It is based mainly on two articles^{1,2}, the first one from my post-doctorate research, the second one from the WAFPI project)

Here we will switch from thermoplastic interfaces, in the melt and in the glassy (or semi-crystalline) state to rubbery interfaces (which can be seen as a crosslinked melt). We will deal with the role of surface roughness, bulk viscoelasticity, and surface chemistry on interfacial properties such as wetting, adhesion, or friction, and how we can tune and/or control these parameters to design model elastomeric materials for studying these properties.

4.1. Contact-line mechanics for pattern control

In this first study, we show how a contact line can dominate a system's behavior when a thin, solid capping layer adheres to a soft substrate, ultimately providing a unique tool for creating localized patterns across laterally extensive lengths. In particular, the narrow deformation of the substrate caused by the contact line is sufficient to buckle the thin plate and locally wrinkle the system.

When a sufficient compressive strain is applied to a bilayer consisting of a thin, stiff film bound to a softer and thicker substrate, a mechanical instability takes place.³ The instability is due to the balance between the energetic cost of bending the film and of stretching the substrate which results in a sinusoidal surface deformation known as wrinkling.⁴⁻¹⁰ Because of their cost-effectiveness and simplicity, wrinkled surfaces can be used for a large range of applications, for example optical surfaces, enhanced adhesives,¹¹ soft-lithographic structures,¹² microfluidic devices or cell culture surfaces.¹³ Several methods have been developed to control the applied strain (thermal expansion mismatch,¹⁰ traction,^{5, 8} or solvent swelling of the substrate¹¹); however, they are all inherently non-local processes and therefore difficult to use in the fabrication of complex devices.

In this experiment, an elastomeric substrate (crosslinked polydimethylsiloxane (PDMS)) is immersed in a water bath and brought into contact with a thin floating glassy PS film.

PDMS is prepared by mixing Dow Corning Sylgard 184 (a liquid silicon rubber) with its curing agent, and degassing for 30 min. The ratio catalyst/prepolymer has been varied between 1 : 20 to 1 : 40. The mixture is spun coated at 200 rpm on a glass slide for 2 minutes to ensure a homogeneous sample thickness (~250 μm) and prevents the PDMS from bending. The samples are then cured for 2 h in a 70 °C oven. The moduli of the substrates are $E_{\text{PDMS } 1:20} = 750 \pm 80 \text{ kPa}$, $E_{\text{PDMS } 1:30} = 400 \pm 50 \text{ kPa}$, $E_{\text{PDMS } 1:40} = 120 \pm 20 \text{ kPa}$. Complementary experiments were performed using a well characterized triblock gel with similar structure than the MAM discussed in the previous chapter (but presumably with longer butylacrylate block), obtained from Kuraray Co, Ltd.. The modulus of the gel substrates is measured using the same setup at 4.5 kPa. PS thin films have been

prepared and characterized using the same spin-coating procedure described in the previous chapters, and thicknesses from 50 nm to 600 nm have been studied. Gradient films have been prepared using a custom-built programmable flow-coater.¹⁴

The substrate slide is fixed on an automated stage (Newport) allowing the control of the angle with a 0.1° precision (fixed at 45° in the study) and the pulling speed in the 0.01–5 mm.s⁻¹ range using a Labview interface, with additional experiments performed by evaporation (roughly 5 × 10⁻⁵ mm.s⁻¹). The substrate is then partly immersed in a container of deionized water. A PS film is subsequently floated on the water and attached to the substrate at the water contact line.

The substrate is then pushed in (or pulled out of) the water at a constant chosen speed, allowing the PS to slowly attach to the elastomer or gel. The locally stretched substrate adheres to the inextensible film at the contact line, and as the contact line passes, the stretched region of the substrate relaxes, thus imposing a compressive stress in the film. If the stress is great enough, well aligned wrinkles for over large length scales following the contact line (see figure 1).

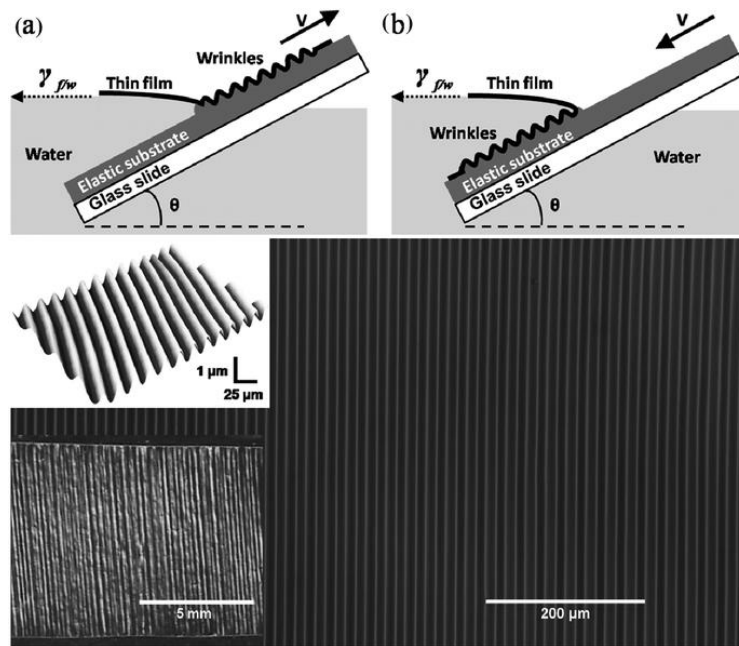


Figure 1: Schematic of the experiment. (a) describes the pulling-out case, (b) the pushed-in scenario. Bottom images show well aligned wrinkles having micrometric amplitude and wavelength on the order of 10 microns over large (centimetric) samples.

The wavelength of the wrinkles λ (obtained from Fourier analysis of optical microscopy or AFM images) is under the assumption of small strain given by:⁴

$$\lambda = 2\pi t \left(\frac{\overline{E}_f}{3\overline{E}_s} \right)^{1/3} \quad (\text{Eq. 1})$$

where t is the thickness of the capping film, $\bar{E} = E/(1 - \nu^2)$ is the plane-strain modulus with Young's modulus given by E , and Poisson's ratio ν . The subscripts f and s refer to the capping film and substrate, respectively.

This equation is valid for both uniaxial and biaxial compressions and has been used extensively.⁴⁻¹⁰ Under the same framework, the amplitude of the wrinkles, A , is given by:⁴

$$A = t \left(\frac{\varepsilon}{\varepsilon_c} - 1 \right)^{1/2} \quad (\text{Eq. 2})$$

where ε is the applied compressive strain and ε_c the critical buckling strain, the maximum strain that can be applied to a plate before it wrinkles. For uniaxial strain:

$$\varepsilon_c = \frac{1}{4} \left(\frac{3\bar{E}_s}{\bar{E}_f} \right)^{2/3} \quad (\text{Eq. 3})$$

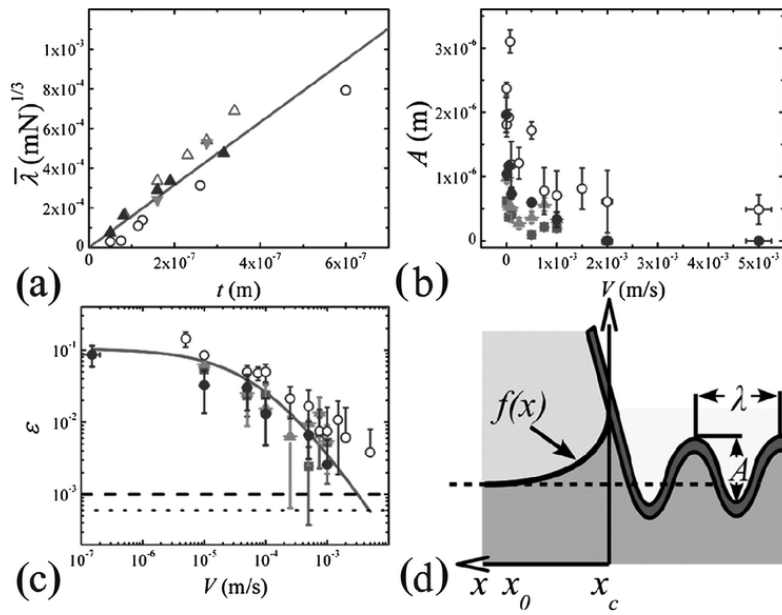


Figure 2: Detailed measurements of the wrinkles created by contact line motion. (a) Scaled wrinkle wavelength, defined as $\bar{\lambda} = \lambda (3\bar{E}_s)^{1/3} / 2\pi$, of polystyrene on several different substrates as a function of film thickness (substrates: 40 : 1 PDMS—filled upward pointing triangles, 30 : 1—open upward pointing triangles, 20 : 1—filled downward pointing triangles, triblock gel—open circles). Solid line is the predicted fit using equation 1. (b) Amplitude of wrinkles as a function of stage velocity (squares—30 : 1 PDMS with 82 nm PS film, triangles—40 : 1 PDMS with 82 nm PS film, closed circles—40 : 1 PDMS with 160 nm PS film, open circles—dipping into fluid 40 : 1 PDMS with 225 nm PS film). (c) Strain as a function of stage velocity for the data shown in (b). Solid curve denotes a fit to equation 3, with $(P/G_0)^2 = 0.106 \text{ m}^2$, $n = 0.642$ and $V^* = 9.73 \times 10^{-5} \text{ m s}^{-1}$. The dashed line denotes the critical strain in 30 : 1 PDMS samples and the dotted line denotes the critical strain in 40 : 1 PDMS. While the 30 : 1 samples may be near the critical strain at $V \approx 1 \text{ mm s}^{-1}$, the 40 : 1 samples remain significantly above the cut off indicating that another mechanism is causing the amplitude to drop to zero. The sample created by dipping into the water (rather than pulling out) shows no cut-off at $V \approx 1 \text{ mm s}^{-1}$ suggesting the hydrodynamics of the coating process plays a role. (d) Schematic showing the details of the contact line as a thin film is attached to a soft substrate (dark grey). The fluid between the substrate and the film is in light grey, the dashed line represents the undeformed surface of the substrate before attachment.

Equation 1 is markedly independent of strain and is ideal for comparison to our experiments where adhesion imparts an unknown strain. Thus, at a given speed of withdrawal (0.1 mm s^{-1}) and angle (45°) with respect to the water surface, we measured the wavelength on samples with different types of elastomeric substrates (chemical structure and moduli) and polystyrene films with different film thicknesses and molecular weights (see figure 2a).

Assuming typical values for Poisson's ratio $\nu_s = 0.5$ for the elastomer, $\nu_f = 0.33$ ¹⁵ for the PS films, the modulus of the PS films $E_f = 3.5 \text{ GPa}$ ⁸ and using independently measured values of E_s , equation 1 is seen to fall on the data with no fitting parameters (see figure 2a). Moreover, both changes in angle and speed do not have significant impact on the wavelength of the wrinkles. We are therefore confident that this technique in no way alters the underlying physics; it simply creates a local compressive strain.

Notably, the amplitude of the wrinkles is observed to be a monotonically decreasing function of substrate velocity. We also observe that no wrinkles form (amplitude falls to zero) in the “pull out” geometry when the substrate speed exceeds a critical value close to 1 mm.s^{-1} , whereas the “push in” scenario always gives rise to wrinkles up to the limiting speed of our motorized stage (see figure 2b). Because the main difference between the two experiments is the fluid between the film and substrate, the hydrodynamics of the coating process must play some role in the wrinkling mechanism, which we address below.

According to equation 2, the variation in amplitude must be related to a change in the applied strain as film thickness and moduli (*e.g.* critical strain) are fixed in a given sample. Therefore, we plot strain calculated directly from $\varepsilon = (\pi t/\lambda)^2(A^2/t^2 + 1)$, as a function of velocity in figure 2c. The amount of strain that is applied to the sample is due to the difference in contour length of the deformed surface compared to the inextensible film. The true surface deformation can be approximated by assuming an adhesive force is applied to a line on the substrate surface.¹⁶ The elastomer surface as a function of distance from the contact point is given by $f(x) \approx (P/\bar{E})\ln(x_0/x)$ where P is the normal component of the tension in the film, and x_0 is the distance at which the perturbation becomes negligible (see figure 2d). The differential strain at the contact line is then evaluated by comparing the difference between an undeformed element and an element along $f(x)$. The differential strain is calculated at the smallest length scale available before the breakdown of the continuum approximation which yields the scaling relation $\varepsilon \approx P^2/G^2$, G being the strain energy release rate. In this particular experiment, the applied force P is due to the unbalanced surface tension at the floating free edge of the polymer film (*i.e.* $\sim \gamma_{\text{film/water}}$). Such deformations of soft elastomers due to surface tension forces have already been observed experimentally¹⁷ and it can be easily verified in our case by the addition of surfactant to the water surface (samples fail to wrinkle). This force will not strongly depend on the speed of the contact line (ignoring hydrodynamic losses). The relationship between applied strain and speed is mainly due to the strong velocity (V) dependence of G . For the polydimethylsiloxane [PDMS] elastomer used here it is known that $G(V) \approx G_0(1 + (V/V^*)^n)$, where n is close to 0.6 and V^* is related to the relaxation of the substrate. Therefore the applied strain scales as:

$$\varepsilon \approx \frac{P^2}{G_0^2(1+(V/V^*)^n)^2} \quad (\text{Eq. 4})$$

The clear agreement between equation 4 and the data (figure 2c) verifies the dominance of the elastomeric losses.

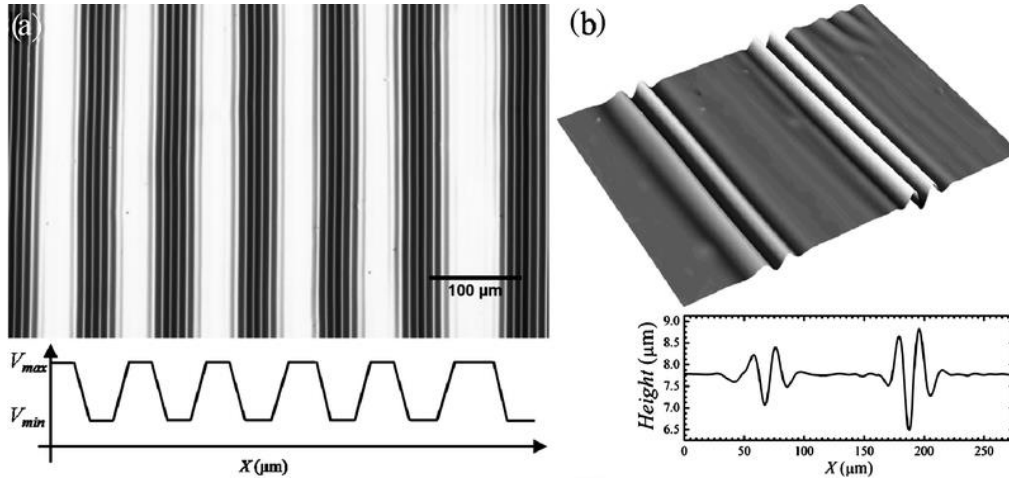


Figure 3: Use of the critical speed to design localized patterning on thin films. (a) Series of regularly spaced aligned wrinkles by setting V_{\max} above the critical value ($V_{\min} = 0.01 \text{ mm s}^{-1}$ here). The brighter wrinkles have smaller amplitude, due to the acceleration of the motor before reaching the experimental speed. Using the same technique with V_{\max} below the critical speed, a continuous pattern with localized differences in amplitude can be obtained (data not shown). (b) Single features (ridges) were obtained using this technique. Note that the control of the amplitude is illustrated in the height profile below ($V_{\min} = 0.1 \text{ mm s}^{-1}$ for the left ridge, $V_{\min} = 0.01 \text{ mm s}^{-1}$ for the right ridge).

As already mentioned, the amplitude is also shown to drop to zero above a withdrawal speed of $1 \text{ mm} \cdot \text{s}^{-1}$ in the “pulling out” experiment (figure 2b). One might expect that this is simply a result of ε falling below ε_c ; however, figure 2c shows clearly that this is not the case. The coating of a substrate by withdrawal from a fluid bath is a classic example of capillarity and predicts a dramatic shift in behaviour of the contact line motion.¹⁸ If the fluid wets the surface ($S > 0$) a coating will always be formed when the substrate is pulled from the bath as there is no energy gained by uncovering the substrate. In contrast, if the fluid does not completely wet the substrate ($S < 0$) the answer is found to depend on the velocity of the plate (V), with the fluid covering the substrate only above some critical speed (V_c).¹⁹ If a non-viscous fluid coating forms between the polymer plate and the substrate the strain will not be “locked in” at the contact line and wrinkles will not form. Although the exact details of the hydrodynamic processes occurring at the contact line remain controversial,^{18,19} the simplest scaling description¹⁸ is sufficient to estimate the critical velocity: $V_c \approx \gamma_w(1 - \cos \theta_e)^3/750\eta$, with θ_e the contact angle of the fluid on the moving substrate, and η is viscosity.

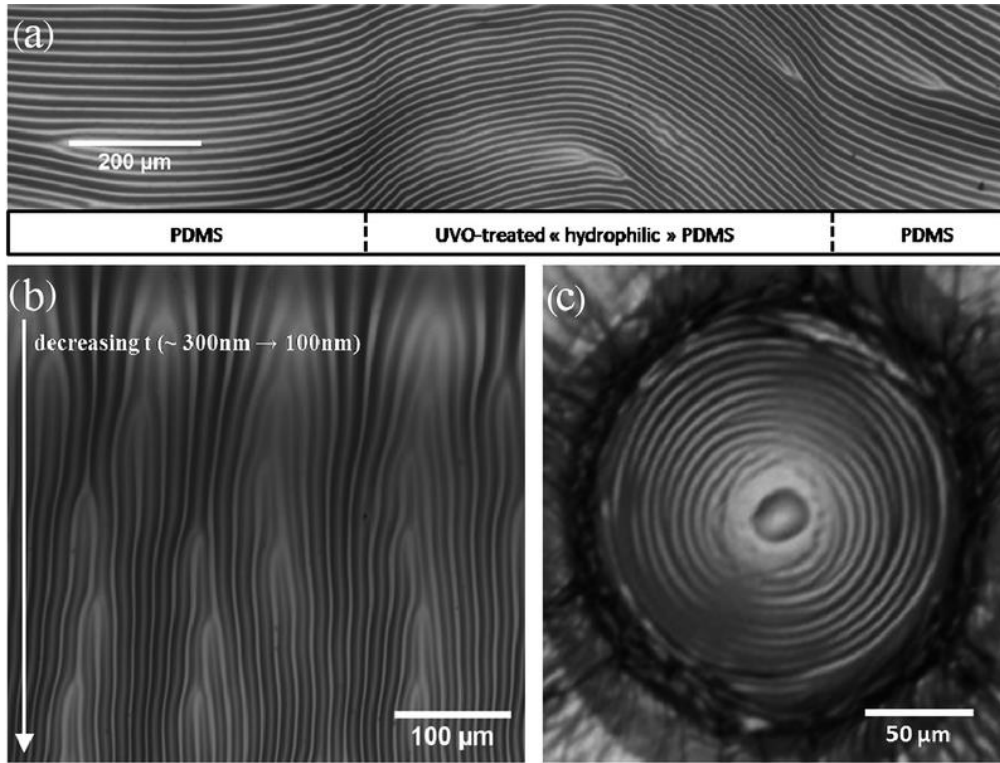


Figure 4: Demonstration of the ability to dictate the shape of the wrinkles by controlling the three point contact line. (a) “Curly” wrinkles obtained using partially UVO-treated PDMS, creating zones with different wettability (hydrophobicity). (b) Creation of connected microchannels with different wavelengths using a gradient thickness film coated perpendicularly to the flow. Note the branching structures revealing strain localization. (c) Formation of circular wrinkles obtained by coating a PS film on a topographically modified triblock gel.

Note that though the equilibrium static contact angle of water on PDMS is usually measured around 100° (see below) the situation here is different and we can assume that even on a hydrophobic surface, the local contact angle between fluid and moving substrate is small. Hence, here $\gamma_v \approx 0.07 \text{ N}\cdot\text{m}^{-1}$, $1 - \cos \theta_e \approx 0.2$, and $\eta \approx 10^{-3} \text{ Pa}\cdot\text{s}$ gives $V_c \approx 1 \text{ mm s}^{-1}$, in good agreement with our measurements. Importantly, this critical velocity can be manipulated by changing the properties of the fluid phase. For example if the geometry is reversed and the substrate is driven into the fluid bath, the fluid being expelled from between the plate and substrate is air and V_c increases dramatically (see figures 2b and 2c).

The control of the magnitude and direction of the strain using the motion of the triple line and the existence of a “critical speed” are unique properties that can be exploited to achieve pattern control that would be extremely difficult or impossible to attain using conventional techniques. We illustrate this versatility by developing a “stop and go” method as shown in figure 3a (*i.e.* coating the substrate at varying speeds above and below V_c in the “pulling out” case) which results in the creation of localized wrinkles. Pushing this methodology allows the creation of isolated single ridges or “micro-channels” (figure 3b).

The capacities to use this simple phenomenon to design well-controlled patterned surfaces were then illustrated. As the wrinkles form parallel to the contact line it is also possible to introduce a curvature in the

pattern by using substrates displaying spatially controlled differences in hydrophobicity (figure 4a), which shifts the local curvature of the contact line. We are able to connect small features (channels) to bigger ones (*i.e.* interconnects) using a thin film presenting a gradient thickness perpendicular to the coating direction (figure 4b). Finally, circular wrinkle patterns can be achieved by introducing topographic curvature in the elastomeric substrate (figure 4c).

4.2. Chemical modification of a rubbery surface without impacting the viscoelasticity

As stated briefly in the first chapter, frictional and adhesive behaviors of elastomers depend on the viscoelastic properties but also on interfacial parameters such as the surface chemistry and the surface topography of the two materials in contact.²⁰⁻²² The role of chemical interactions at the interface²³ and surface patterning²⁴⁻²⁷ as well as viscoelasticity effects^{28, 29} on adhesion, friction, and also on other surface properties such as wetting, has thus started to be investigated extensively over the last years, but mostly independently from each other. However a real deep understanding of the coupling between these properties remains a challenge, and in consequence there is still a lack of prediction of the global effect of such properties.

To identify the incidence of patterning on wetting, adhesion, and friction mechanisms, commercial polydimethylsiloxane (PDMS)-based elastomers have often been chosen as candidates as they have good mechanical properties, good thermal and chemical stability, transparency, and can be easily fabricated and patterned with good reproducibility. These features make these materials perfectly suited for applications in microfluidic or transfer printing. However, PDMS is rather chemically stable and has a low surface free energy (measured between 21-25 mJ/m²).³⁰ Moreover, these materials lack reactive surface groups, and may present low-molecular-weight mobile components having a high tendency to migrate to the PDMS surface from the bulk. This results in relatively poor intrinsic adhesive properties for these materials.

On the other hand, chemical modification of PDMS interface can drastically alter its frictional, adhesive and wetting properties but will also, in general, affect its mechanical properties. Indeed, developing a simple route to change the chemical properties of PDMS surfaces only, without impacting the bulk modulus (or creating, from a mechanical point of view, a bilayer system), is a challenging task which would prove useful to design model systems for a better understanding of the exact contribution of the surface chemistry on surface properties (adhesion, friction and wetting) of elastomers.

To modify the properties of PDMS surfaces and confer hydrophilicity to PDMS surfaces, various surface modification methods have been explored. One of the easiest means for generating the hydrophilic PDMS surface is its exposure to an air or oxygen plasma treatment.³¹ However, this treatment leads to the formation of a stiff SiOH layer at the surface, which will then make the physical analysis of surface properties difficult and can lead to uncontrolled wrinkling and associated phenomena like surface cracks and grooves.³² Furthermore, the result of this kind of treatment is temporary, and the surface will usually recover its hydrophobicity within a few hours due to low molecular weight chains diffusing to the surface and rearrangement of polymer chains

near the interface.³³ Several other PDMS surface modification strategies have been explored,³⁴⁻³⁷ but all of them are long, complicated and dramatically alter the bulk and mechanical PDMS properties (often by a factor of 2 or more on the modulus when compared to unmodified PDMS).

An easier path consists in coating PDMS surface with hydrophilic polymers such as poly(ethylene glycol) (PEG) and its derivatives. Several techniques have been proposed to achieve this grafting. Star shaped PEG was grafted on PDMS functionalized using ammonia plasma treatment.³⁸ Simpler, Brook *et al.* developed a route using poly(ethylene glycol) monoallylether.³⁹ This method is a two-step surface modification process. Since PDMS does not have appropriate functional groups on the surface available to react with PEG, modification is necessary to introduce first active sites for subsequent functionalization. PDMS is initially functionalized with SiH groups under acid catalysis to give PDMS-SiH, followed by a platinum catalyzed hydrosilylation reaction with PEG. This is an addition reaction between SiH and allyl groups of PEG to create SiC bonds, and it is a method to replace the methyl groups on PDMS with PEG.

Inspired by this two-step strategy, we chose poly(ethylene glycol) methyl ether acrylate (PEG-acrylate) to modify PDMS surfaces (Sylgard 184) through covalent bonding of PEG-acrylate chains on PDMS surfaces. We chose poly(ethylene glycol) acrylate (PEG-acrylate) because of three reasons: (1) this molecule has a terminating acrylic group (2) it is inexpensive and commercially available from common chemical companies with various molar masses and (3) the lower molar masses are liquid at room temperature, making it easy to react with PDMS disks of relatively large proportions. Moreover, the layer formed, being only a few monomers long, could be added on flat or patterned surfaces, and has the potential to be “invisible” in terms of mechanical properties.

PDMS samples used in this study for the surface modifications experiments are prepared by mixing the Sylgard 184 elastomer base (vinyl-terminated PDMS linear chains) with the curing reagent (short chains presenting Si-H functions to react with the vinyl groups) in a 10:1 (w / w) ratio (unless otherwise specified) followed by degassing in vacuum for about 15 min to remove the bubbles formed during mixing. The mixture was poured into a Petri dish and cured at 70 °C for 17 hours in an oven. The resulting film, about 1 mm thick (1.5 mm for rheological measurements), was cut into 2 cm (2.6 cm for rheological measurements) diameter discs for chemical modification and further analysis.

Figure 5 illustrates the reaction scheme of the surface modification of PDMS. The incorporation of SiH groups on the PDMS surfaces involves exchanging Me₂SiO of PDMS with HMeSiO of PHMS using acid catalysis (trifluoromethanesulfonic acid). This leads to PDMS with a high concentration of SiH groups on its surface. After rinsing and drying, samples were stored under anhydrous conditions in a desiccator to prevent loss of SiH groups. During the surface functionalization, two competing reactions occur: the first involves surface monomer exchange and the second degradation (breaking of the covalent network due to the presence of the acid) of PDMS. The efficiency of each reaction depends on various factors such acid catalyst concentration and reaction times. Increased reaction times lead to increase SiH groups at the surface of PDMS for about 30 minutes of reaction time. Longer reaction times and higher concentrations in acid catalyst lead to

depolymerization process of the PDMS.⁴⁰ The details of the experimental procedure can be found in reference 2.

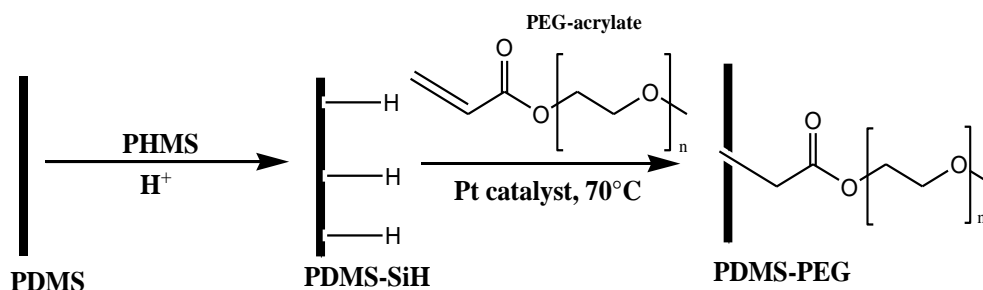


Figure 5: Schematic of surface modification of PDMS.

In order to prepare the PEG modified surfaces, PDMS-SiH disks were introduced into a mixture of PEG-acrylate and diethylene-glycol dimethyl ether in proportions such as PEG-acrylate is in large excess compared to SiH, with a Karstedt's catalyst and the mixture was stirred for different reaction times (between 4 h and 72 h) at 70 °C. It is worth noting that the choice of solvent in particular is critical in the two steps of the process. It is necessary to use a solvent that does not react with the highly reactive hydrosilane groups. Solvents that swell the silicone, such as hexane, toluene, would also lead to Si-H incorporation throughout the elastomer and internal hydrosilylation.

To characterize the bonding between the PEG-acrylate and PDMS after modification, any free PEG-acrylate unreacted with PDMS needs to be removed from the PDMS discs. Acetone is a good solvent for PEG-acrylate while being a poor solvent for PDMS. Washing PDMS discs with acetone can completely extract unreacted PEG-acrylate from the bulk PDMS. PDMS pieces were characterized after this extraction process and drying under vacuum at room temperature overnight.

Fourier transform infrared spectroscopy in attenuated total reflectance (ATR-FTIR) mode was used to analyze the effects of PEGylation on the surface chemistry of PDMS. The depth of penetration, d_p is given by:

$$d_p = \frac{\lambda}{2\pi(n_1^2 (\sin \theta)^2 - n_2^2)^{1/2}} \quad (\text{Eq. 5})$$

where λ is the wavelength of light, θ is the angle of incidence of the IR beam relative to the perpendicular of the crystal surface, n_1 is the refractive index of the diamond (2.4 in this range of wavelengths) and n_2 is the refractive index of the PDMS (1.4 as given by Dow-Corning). The depth of penetration is then $\sim 1 \mu\text{m}$ at 2000 cm^{-1} .

The unmodified PDMS spectrum displays the typical bands revealing the backbone structure of the network - Si(CH₃)₂-O-. All these peaks can also be identified for both modified PDMS (see Figure 6a). A worth noting

point is that a small peak at 1598 cm^{-1} (figure 6b) can clearly be seen in the spectrum for the unmodified PDMS, and is also present with a small shift for the modified samples (1612 cm^{-1} for the PDMS-SiH and 1642 cm^{-1} for the PEG-modified PDMS), which could be assigned to the stretching vibration of C=C bonds and indicate that some terminal vinyl groups did not react during the crosslinking reaction (this can be confirmed by $^1\text{H-NMR}$ of a Sylgard 184 mixture of base and curing agent in a 10:1 ratio, showing an excess of vinyl groups over Si-H functions, data not shown).

Figure 6b zooms in the region of interest concerning the peaks concerning the modifications induced by the two-step procedure. In particular, the major difference among these spectra is the appearance of a strong new band of Si-H at 2166 cm^{-1} on the PDMS-SiH surface, which is not present on either the unmodified PDMS surface or the PEG-modified PDMS surface, making it an easy way to follow PEG modification. Following hydrosilylation, the appearance of a new broader CH_2 stretching vibration around 2870 cm^{-1} corresponds to the $\text{CH}_2\text{-O}$ repeat group in the PEG-modified surface. This peak is not present on either the unmodified surface or on the PDMS-SiH surface. In addition, another peak appears at 1742 cm^{-1} on the PEG-modified surface. This peak is assigned to the PEG-acrylate carbonyl group (at one end of PEG-acrylate). Considering that free PEG-acrylate has been removed to form PDMS-PEG, the ATR-FTIR results clearly demonstrate that PEG chains have been covalently linked to the PDMS network by 1,2-addition hydrosilylation reaction. One should also note the presence of a small broad peak at 3500 cm^{-1} in the PEG-modified PDMS sample. This could reveal the presence of Si-OH resulting from the hydrolysis of some SiH groups. However, the high frequency of the peak (typical value for Si-OH is $3400\text{-}3200\text{ cm}^{-1}$) probably rather reveals the presence of water, due to the hydrophilicity of the PEG-surface.

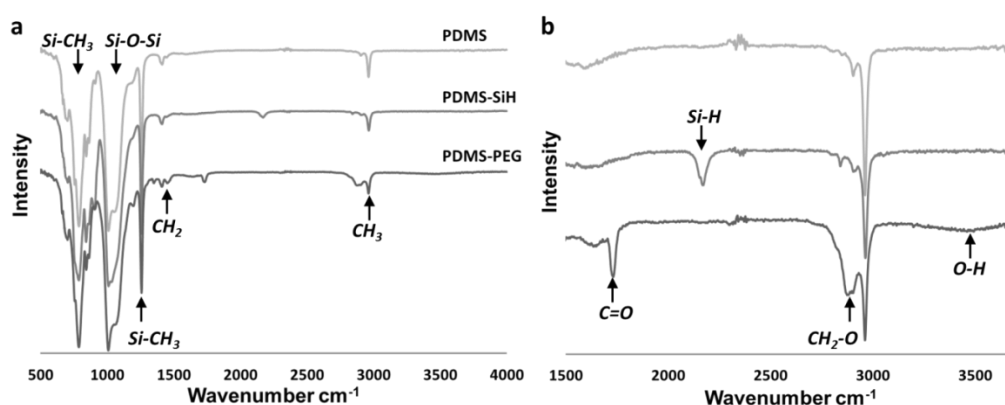


Figure 6: ATR-FTIR spectra for control PDMS (light grey), PDMS-SiH (grey) and PDMS-PEG (dark grey) (a), with assignment of chemical functions present in the 3 samples. Zoom in the $1500\text{-}3700\text{ cm}^{-1}$ region (same color code) (b), with assignment of specific chemical functions due to the chemical modifications.

Finally, let us point out that the depth of penetration of the ATR-FTIR, on the order of $1\text{ }\mu\text{m}$, and the intensity of the characteristic peaks for the modifications, suggest that the chemical reactions may occur not only on the

surface but also within some depth of the sample. This can be explained by the fact that though methanol and diethylene-glycol dimethyl ether are poor solvent for PDMS, they can still swell the network by a small amount and thus lead to chemical reaction within the network near the surface.⁴¹

Figure 7 shows pictures of whole samples deposited on top of a grid, and AFM images of the PDMS and PEG-modified PDMS surfaces under different modification times. It is clear from the top pictures that the samples lose some transparency when modified (the grid below becomes less and less visible), with a more pronounced effect when the modification time is increased, even though they all remain translucent. The Root-Mean Square Roughness R_q (standard deviations of the height value within a given image) was determined through the AFM software. AFM image of the surface shows an almost perfectly flat surface for the unmodified PDMS ($R_q \sim 1$ nm). Similar to the unmodified PDMS, the roughness of the PDMS-SiH is found to be 2 nm (image not shown). This result indicates that the incorporation of SiH groups on the PDMS surfaces using acid catalysis does not affect the surface roughness and that, for these reaction times (30 mn for this first step), the acid does not significantly depolymerizes the PDMS (or, if so, in a uniform manner at the lateral resolution of the AFM).

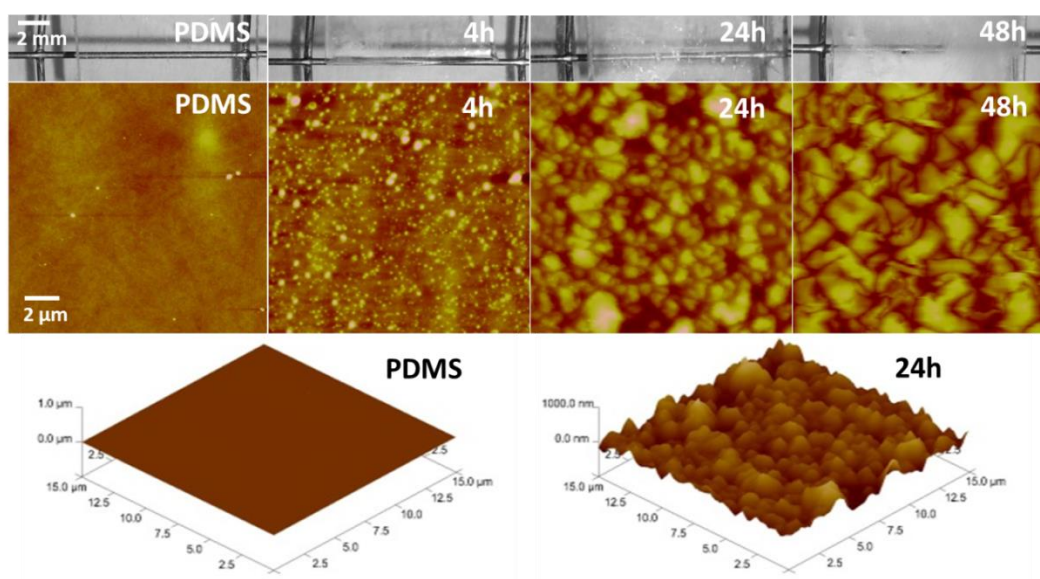


Figure 7: Top row: Pictures of unmodified PDMS and PEG-modified PDMS samples with different modification times. Middle row: AFM surface topographies of unmodified and PEG-modified PDMS with different modification times. Bottom row: 3D images of the unmodified PDMS and PEG-modified PDMS with 24h of modification time.

However, the morphology of the PEG-modified PDMS surface is clearly impacted by the PEG grafting step. After 4 hours of modification, the PEG-modified PDMS displays a rougher surface than the unmodified PDMS ($R_q \approx 10$ nm). Actually, the surface is mostly flat with aggregates having diameters (or lateral sizes) of few hundreds of nm and height around 50 nm. After 15h of modification, the roughness remains similar ($R_q \approx 15$ nm, image not

shown). However, for 24 and 48 hours of modification, the roughness increases sharply (around 100 nm for 24h and up to 200 nm for 48 hours). The aggregates increase both in heights and lateral dimensions (up to a few microns). The appearance and growth of these regions as modification time increases can explain the loss in transparency.

Similar morphologies on PEG-modified PDMS have been observed⁴⁰ and explained by a phenomenon of phase separation between PEG and PDMS due to the incompatibility between the two polymers. However, in these systems, PEG was added in default and not in excess, and the resulting height of the patterns was only a few nm. The height of the patterns measured here is much higher than the size of the very short PEG chains, and so the aggregation mechanism remains unclear since the samples are thoroughly washed before testing using a good solvent for short PEG chains (acetone). The increase in roughness could also be the result of the migration to the surface, due to the chemical modifications, of some of the thin polymer layers covering silica and other reinforcing fillers present in the Sylgard 184, as suggested by Genzer et al.⁴²

Rheological measurements performed on different PDMS samples show the influence of the chemical modification on the viscoelastic properties of the materials. In Figure 8, deformation sweep measurements are presented (G' , left, G'' , right). First, one can notice that all the materials shown here are very elastic ($G' \sim 10 G''$) in all the deformation range. It is also noticeable that the results are fairly reproducible: concerning the unmodified 1:10 PDMS cured 17 h at 70 °C, 7 samples were tested using the same procedure. The standard deviation was below 8 % for every data point for the G' .

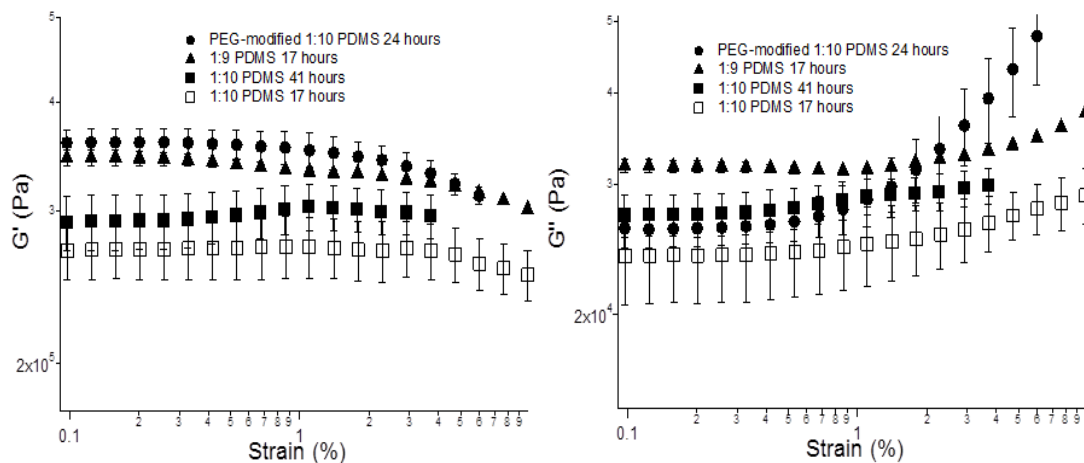


Figure 8: Storage modulus G' (left) and loss modulus G'' (right) as a function of strain at constant frequency (1Hz) for modified and unmodified PDMS at different curing times and curing agent ratio. The data points are the average over all the samples tests (see materials section), the error bars represent the standard deviation from this average values calculated for each point.

Then, using a Poisson's ratio of 0.5 for PDMS,¹⁵ one can estimate the Young's modulus for the unmodified 1:10 PDMS as measured by this technique. This leads to a value close to 0.85 MPa in all the deformation range ($G' \sim$

0.275 MPa). This value is quite substantially lower than what is usually reported for PDMS prepared under similar conditions and measured with different techniques. For example, using rheological experiments with samples crosslinked in situ, Nase et al.²⁹ obtained a value of 2.4 MPa for a 1:9 PDMS cured at 80°C for 5h under vacuum, and 0.87 MPa for a 1:15 sample prepared under the same conditions. Using JKR, Poulard et al.²⁷ obtain a value of 1.8 MPa for a 10:1 sample cured at 50 °C during 24 h, while using the same technique, Davis et al. obtain a value of 2 MPa for a sample cured at 70 °C for 24 h.⁴³

However, such discrepancies between different techniques (nanoindentation, DMA, JKR and rheological measurements) have already been reported concerning measurements of PDMS moduli (between 1 and 3 MPa depending on the measurement for a given sample, though the reasons for these discrepancies are not discussed).⁴⁴

Since reproducibility of the experiment remain satisfactory, if we compare G' of the unmodified PDMS to the value of the PEG-modified 1:10 PDMS (24 h modification), G' for these samples is 0.35 MPa, a 25 % increase. One could assume that this increase in the shear modulus is due to the extra-curing time induced by the modification if unreacted species remain in the sample, because the reaction is performed also at 70 °C for 24h right after the 17 h curing. Indeed, the 41 hours (eg 17 + 24 h) cured PDMS has a G' value of 0.3 MPa slightly above the 17 hours cured PDMS (which demonstrates that little crosslinking occurs spontaneously in the sample after the first 17 hours of curing). However, G' is still roughly 15% below G' of the PEG-modified PDMS. This small difference between the 41 hours cured PDMS and the PEG-modified one may then be explained by the chemical reaction adding new SiH functions in the material which will react on the surface with the PEG, but can also react with the remaining double bonds and cause a small extra-crosslinking over some depth within the sample.

However, if one wants, for example, to compare modified samples with unmodified ones having same viscoelastic properties in terms of adhesive or wetting properties, this rather slight increase can be easily addressed: a 1:9 PDMS cured for 17 hours or 41 hours (data not shown) has a G' of 0.335 MPa, remarkably close to the one measured for the PEG-modified 1:10 PDMS.

Values for G'' are all comparable for every samples tested (between 25 kPa and 32 kPa below 2 % deformation). The slight increase at higher strains may reveal slippage during the test or an increase in the viscoelasticity at higher deformations.

Water contact angle measurements were then performed to assess the hydrophobicity of the surfaces before and after modification with PEG-acrylate. The contact angle values measured immediately after the chemical treatment for the various samples are presented in Figure 9.

As expected, the unmodified PDMS is found to be strongly hydrophobic, with a static angle of about 110 °, consistent with many results presented in the literature. However, modification of PDMS with PEG-acrylate has

a significant impact on the measured water contact angle. Its value decreases at first with modification time. After 24 hours of reaction, static contact angle reaches a value of 67°. For higher modification times (48 and 72 hours), the value of the contact angle modified PDMS then reaches a plateau value (65°). The sharp decrease in the contact angle from 80° to 67° when modification time increases from 15 hours to 24 hours may be correlated to the increase in surface roughness induced by the density of PEG grafting as discussed above. This contact angle shift with the PDMS-PEG confirms again the existence of PEG on the surface. These values are greater than that of pure PEG films (20-25°)⁴⁵ and indicate either that the surface is not fully covered by PEG chains or that the water still partially “feels” the PDMS underneath the PEG layer, due to its thinness. The observed trends reflects the increase in chain density of PEG at the surface of the PDMS and probably indicates that for reaction times higher than 24 hours, the concentration of grafted PEG at the surface is maximal. It is also worth noting that a synthesis conducted for 24 h with a doubled concentration of PEG-acrylate during the reaction step also leads to a value of 67° for the static contact angle. This confirms the excess of PEG-acrylate in the step 2 of the reaction and that there is a limit in terms of grafting density of PEG on the PDMS surface.

In order to use these samples for example for adhesion tests, hydrophobic recovery in air of the chemically treated surface is also estimated by measuring the contact angle at regular intervals of time after the surface treatment. For example, the initial contact angle achieved immediately after the treatment of 72 hours is 65° but subsequently increases to about 90° after about 4 weeks in air. This relatively slow increase in contact angle over time is in agreement with other reports⁴⁶ indicating that there is gradual hydrophobic recovery of the treated surface due to migration of low molecular weight species, from the bulk to the surface, or due to reorientation of the PEG hydrophilic groups away from the surface.

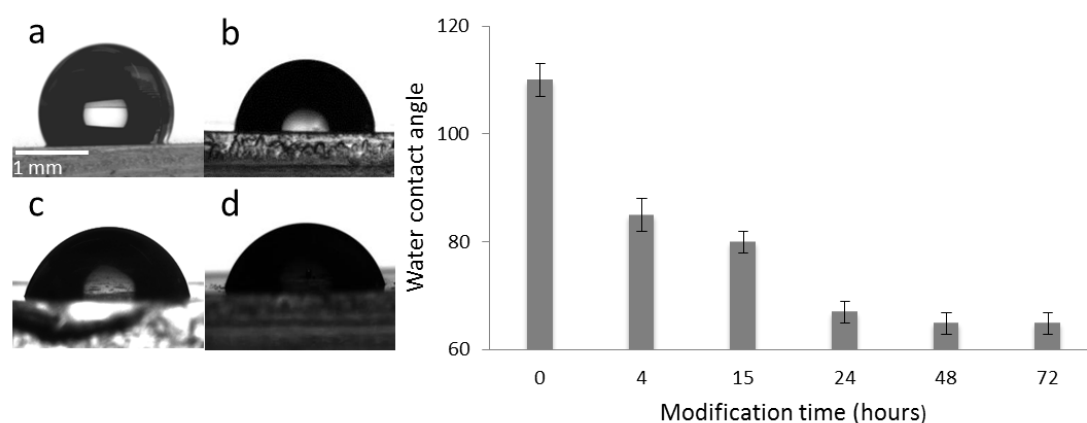


Figure 9: Left: Water contact angle for a: native PDMS; b: PEG-modified PDMS after 4 hours; c: PEG-modified PDMS after 24 hours and d: PEG-modified PDMS after 72 hours. Right: water contact angles for modified PDMS with different reaction times.

To obtain further insights on the properties of PEG coated PDMS surface, dynamic contact angle measurements have been obtained by continuously enlarging and subsequently reducing the size of water drop through an embedded needle and recording the evolution of the contact angle over the radius of the droplet. Figure 10 shows typical optical images of advancing, and receding water drops dynamic contact angle measurements on PDMS surface before and after 24 hours of chemical modification. In the case of unmodified PDMS, the results of the contact angle measurements show that their mean advancing and receding contact angles are $\theta_a = 114^\circ$ and $\theta_r = 89^\circ$, respectively. The associated contact angle hysteresis is about 25° . Chemical modification with PEG has a significant effect on the advancing and receding contact angles which are about 83° and 40° respectively for PEG-modified PDMS for 24 hours. The contact angle hysteresis is then 43° . It is seen that the PEG-modified PDMS showed a significant decrease in both advancing and receding contact angles for modification times below 24 hours, but also a significant increase in the contact angle hysteresis. Though changes in crosslink densities (or Young's moduli) of elastomers can affect both contact angles and hysteresis,⁴⁷ it is a fairly small effect when comparing samples with only a 25 % difference in the modulus, and so it could not account for the significant differences measured in this study between unmodified and modified PDMS. However, this may indicate PEG chains local movements towards the water during the experiment or confirms the effects due to chemical heterogeneity or surface roughness appearing after the chemical treatment.⁴⁸ The observed difference in the two angles could also be due to the surface penetration of water during contact angle determination. After 24 hours of modification, PDMS surfaces show a constant advancing and receding contact angle with time which is consistent with the previous hypothesis that all silicone hydride bonds (Si-H) created on the surface have already reacted. It is worth noting that these values are similar reported values from the literature for PEG-modified PDMS surfaces.³⁹

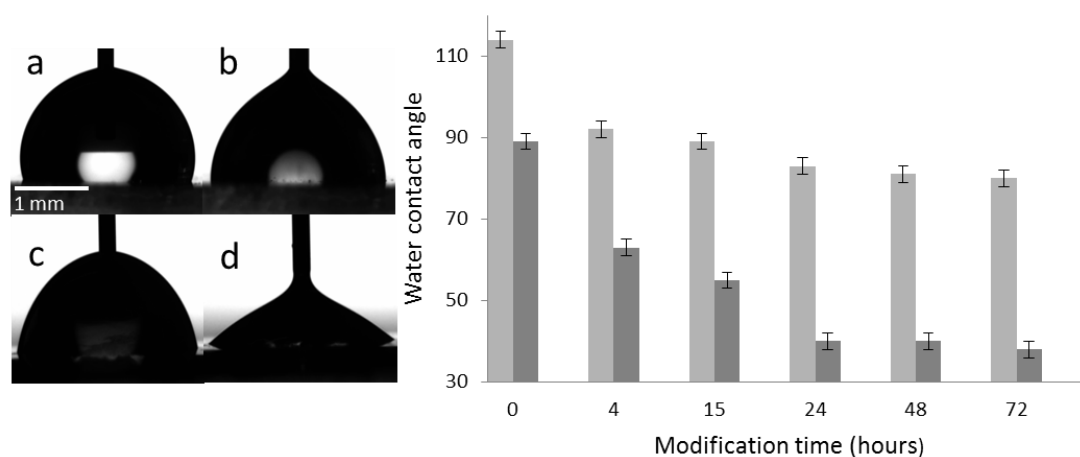


Figure 10: Left: Typical optical images for advancing (a) and receding contact angle (b) of water for unmodified PDMS. (c) and (d) are respectively the advancing and the receding contact angle contact angle of PEG-modified PDMS after 24 hours of treatment. Right: Advancing (light grey bars) and receding (dark grey bars) water contact angles for modified PDMS with different reaction times.

Finally, JKR experiments were performed to obtain the work of adhesion (W) and the elastic modulus (E) of the modified and unmodified PDMS.

In order to compare elastic modulus values obtained via the rheological experiments with those obtained using the JKR technique and gain information about the adhesive behavior of the samples, loading measurements using the JKR technique were performed, and are shown in Figure 10 $F/\sqrt{6\pi a^3}$ (with F the force applied and a the radius of contact) being plotted as a function of $a^{3/2}/\sqrt{6\pi R}$ (with R the radius of the probe). The experimental data are fitted with Equation 3, then allowing measurements of W and E .

By fitting the measured curve for two identical surfaces of 1:10 PDMS cured during 17 hours, the work of adhesion was found to be $W = 50 \text{ mJ/m}^2 \pm 3.6$. The corresponding measured surface energy is then $\gamma_1 = \gamma_2 = 25 \text{ mJ/m}^2$ (since in this case of PDMS in contact with PDMS $\gamma_{12} = 0$ and reversible thermodynamic work of adhesion is $W = \gamma_1 + \gamma_2$), in agreement with previous studies.³⁰ The elastic modulus obtained from the fit is 1.45 MPa. For 1:10 PDMS samples cured during 41 hours, the fit between the experimental loading data and yielded values: $W = 50 \text{ mJ/m}^2 \pm 1.6$ (hence same surface energy) and $E = 1.65 \text{ MPa}$, showing a small increase in Young modulus as already observed with the rheological measurements. Using the same unmodified PDMS lens for the measurements but now in contact with a 24h PEG-modified 1:10 PDMS substrate, we obtain $W = 52 \text{ mJ/m}^2 \pm 2.7$ and $E = 1.74 \text{ MPa}$.

First, it is worth noting that there is a difference between the elastic modulus measured by JKR and by rheology, similar to what other researcher groups⁴⁴ have observed for similar material systems using different measurements techniques, as discussed above. Still, the differences observed for unmodified and modified PDMS are consistent for the two techniques. Furthermore, the values obtained from the JKR test are in agreement with the ones reported by other studies.²⁵

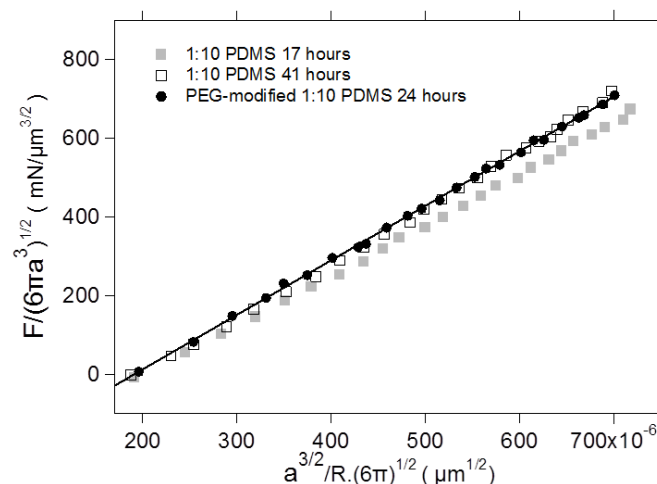


Figure 11: Curves showing the behavior of PDMS samples (semispherical unmodified PDMS lens on flat sheet) of 1:10 PDMS cured 17 hours at 70°C (full gray square), 1:10 PDMS cured 41 hours (open square) and PEG-modified PDMS with 24 hours of reaction time (black circle) during loading cycle.

Second, a small change in work of adhesion is observed between identical and modified substrates. This may appear surprising, as the surface free energy of the modified substrate should be larger than that of unmodified PDMS, as suggested by the contact angle measurements. However the analysis of the JKR result has to be done carefully due to the asymmetric nature of the contact, which thus implies a non-zero interfacial energy γ_{12} . To try to estimate the surface energy of the PEG-modified PDMS (γ_2), we use $\gamma_1 = \gamma_{\text{PDMS}} = 25 \text{ mJ/m}^2$ and roughly estimate γ_{12} (PDMS surface and PEG-modified PDMS surface) by $\gamma_{\text{PEG-PDMS}}$.

The latter can be measured by using Young equation for a drop of PEG resting on an unmodified PDMS substrate. The advancing contact angle between PDMS and PEG-acrylate has been measured at 61.6° and the receding contact angle at 45° . The equilibrium contact angle in Young equation has been defined as $\frac{1}{2}(\theta_a + \theta_r)$ by Brochard-Wyart et al.,⁴⁹ which gives 53.3° here. A more complicated analytical expression has been proposed by Tadmor⁵⁰ and leads to 55° with our measurements. The surface energy of PEG γ_{PEG} is reported to be $42\text{-}45 \text{ mJ/m}^2$ for high molecular weights.¹⁵ However, molecular-weight dependence has been predicted for surface tension of polymers and observed experimentally for many polymers, such as PEG with various end groups, in the low molecular weight (oligomeric) range.⁵¹ For $M_n = 480 \text{ g/mol}$, the surface energy for PEG can be estimated at $\gamma_{\text{PEG}} \sim 37\text{-}39 \text{ mJ/m}^2$ (using both experimental data for similar molar masses listed in reference¹⁵ and empirical equations in reference⁵¹).

This finally leads to an estimated value of $\gamma_{\text{PEG-PDMS}} \sim 2\text{-}3 \text{ mJ/m}^2$. Then, coming back to the thermodynamic work of adhesion, the corresponding surface energy of PEG modified 1:10 PDMS is $29\text{-}30 \text{ mJ/m}^2$. This value represents an increase of 20 % relative to that of unmodified PDMS, even if still below the surface energy of PEG. This may reflect the fact that the grafted PEG chains are short (the PEG molecule used is about 9 or 10 monomeric units), which means PDMS is still “seen” macroscopically when surfaces are in contact, but could also mean that the surface is not fully covered by PEG chains.

One could state that the adhesion energy can also be affected by the roughness of the surfaces. Unfortunately only little is known of the exact role of roughness on the adhesion energy extracted from a JKR test since it is always difficult to guarantee that the surface topography and not the chemistry have been changed. Nevertheless, an article by Verneuil et al.⁵² showed that when the roughness is small (typically smaller than 200 nm) as is the case in this study, its effect on the thermodynamical work of adhesion is small. Moreover, this roughness effect leads to a decrease in the work of adhesion, which would mean an underestimated value for the surface energy of the PEG-modified PDMS.

Anyhow, one should not over-interpret the values presented above. Indeed, we would like to point out that this estimate, which is in agreement with the contact angle experimental results, remains semi-quantitative due to the fact that the effect is quite small, and to cumulative uncertainties on both the JKR experiments and fits, the definition of an equilibrium contact angle when hysteresis is present, the effect of roughness, and the available reported values of surface tensions.

In summary, the surface modification of PDMS surfaces with PEG-acrylate has been successfully achieved using a two-step technique and leads to a significant increase in surface hydrophilicity. Compared to unmodified PDMS, PEG-modified exhibited lower water contact angle (down to 65 ° for the static contact angle) and a significant increase in the hysteresis. It is shown that this reaction can be made without impacting significantly the viscoelastic properties (slight increase – around 15 %- in G' and no significant change in G'') of the PDMS but with a slight effect on the surface roughness (~100 nm). The surface energy of PEG-modified PDMS has been measured close to 30 mJ/m² compared with 25 mJ/m² for the unmodified PDMS, which is in semi-quantitative agreement with the contact angle results.

4.3. Conclusion and future work

The contact-line method to produce wrinkled surfaces has been used extensively in Crosby's group and its capacities increased over the past years. High aspect ratio wrinkles ($\lambda / A > 0.5$ while typical wrinkles have aspect ratio ~ 0.1) can be achieved through the use of pre-stretched substrates.⁵³ It was also derived to a plate-to-roll geometry to laminate a thin film on a soft substrate.⁵⁴ The setup was successfully implemented in the PIMM lab and used in the WAFPI project. It was shown that wrinkled PDMS surfaces can be easily obtained through molding and subsequently chemically modified using the previously described method.

To clarify the role of chemical interactions at the interface and surface patterning as well as viscoelasticity effects on adhesion, friction and wetting, further work will deal with the transfer of the described two-step technique for the modification of PDMS surfaces presenting controlled micron-sized patterns (such as wrinkles, lines or posts) to tune independently both surface patterning and surface chemistry of the PDMS, while the viscoelastic properties of the PDMS can simply be changed by varying the amount of crosslinker. The combination of fabricating a patterned structure and a tailored chemistry surfaces without changing its original structure and rheological properties would non-only increase our understanding in the coupling between topography and surface chemistry in the surface properties of materials, but also open up opportunities for new adhesive materials with well-designed surfaces.

4.4. References

1. Miquelard-Garnier, G.; Croll, A. B.; Davis, C. S.; Crosby, A. J., Contact-line mechanics for pattern control. *Soft Matter* **2010**, 6, (22), 5789-5794.
2. Dirany, M.; Dies, L. t.; Restagno, F. d. r.; Léger, L.; Poulard, C.; Miquelard-Garnier, G., Chemical modification of PDMS surface without impacting the viscoelasticity: Model systems for a better understanding of elastomer/elastomer adhesion and friction. *Colloids and Surfaces A: Physicochemical and Engineering Aspects* **2016**, 468, 174-183.
3. Timoshenko, S.; Woinowsky-Krieger, S., *Theory of plates and shells*. McGraw-Hill: **1959**.
4. Genzer, J.; Groenewold, J., Soft matter with hard skin: From skin wrinkles to templating and material characterization. *Soft Matter* **2006**, 2, (4), 310-323.
5. Efimenko, K.; Rackaitis, M.; Manias, E.; Vaziri, A.; Mahadevan, L.; Genzer, J., Nested self-similar wrinkling patterns in skins. *Nature Materials* **2005**, 4, (4), 293-297.
6. Groenewold, J., Wrinkling of plates coupled with soft elastic media. *Physica A* **2001**, 298, (1-2), 32-45.
7. Howarter, J. A.; Stafford, C. M., Instabilities as a measurement tool for soft materials. *Soft Matter* **2010**, 6, (22), 5661-5666.
8. Stafford, C. M.; Harrison, C.; Beers, K. L.; Karim, A.; Amis, E. J.; Vanlandingham, M. R.; Kim, H. C.; Volksen, W.; Miller, R. D.; Simonyi, E. E., A buckling-based metrology for measuring the elastic moduli of polymeric thin films. *Nature Materials* **2004**, 3, (8), 545-550.
9. Vandeparre, H.; Damman, P., Wrinkling of stimuloresponsive surfaces: Mechanical instability coupled to diffusion. *Physical Review Letters* **2008**, 101, (12).
10. Bowden, N.; Brittain, S.; Evans, A. G.; Hutchinson, J. W.; Whitesides, G. M., Spontaneous formation of ordered structures in thin films of metals supported on an elastomeric polymer. *Nature* **1998**, 393, (6681), 146-149.
11. Chan, E. P.; Crosby, A. J., Fabricating microlens arrays by surface wrinkling. *Advanced Materials* **2006**, 18, (24), 3238-+.
12. Xia, Y.; Whitesides, G. M., Soft Lithography. *Angewandte Chemie International Edition* **1998**, 37, (5), 550-575.
13. Ito, Y., Surface micropatterning to regulate cell functions. *Biomaterials* **1999**, 20, (23-24), 2333-2342.
14. Meredith, J. C.; Smith, A. P.; Karim, A.; Amis, E. J., Combinatorial Materials Science for Polymer Thin-Film Dewetting. *Macromolecules* **2000**, 33, (26), 9747-9756.
15. Mark, J. E., *Physical Properties of Polymers Handbook*. Springer: **2006**.
16. Johnson, K. L., Line loading of an elastic half-space. In *Contact Mechanics* Cambridge University Press: Cambridge, **1985**; pp 11-44.
17. Pericet-Camara, R.; Auernhammer, G. K.; Koynov, K.; Lorenzoni, S.; Raiteri, R.; Bonaccorso, E., Solid-supported thin elastomer films deformed by microdrops. *Soft Matter* **2009**, 5, (19), 3611-3617.
18. de Gennes, P. G., Deposition of Langmuir-Blodgett layers. *Colloid and Polymer Science* **1986**, 264, (5), 463-465.
19. Eggers, J., Existence of receding and advancing contact lines. *Physics of Fluids* **2005**, 17, (8), 082106.
20. Shull, K. R., Contact mechanics and the adhesion of soft solids. *Materials Science & Engineering R-Reports* **2002**, 36, (1), 1-45.
21. Crosby, A. J.; Hageman, M.; Duncan, A., Controlling polymer adhesion with "pancakes". *Langmuir* **2005**, 21, (25), 11738-11743.
22. Chan, E. P.; Greiner, C.; Arzt, E.; Crosby, A. J., Designing model systems for enhanced adhesion. *Mrs Bulletin* **2007**, 32, (6), 496-503.
23. Thanawala, S. K.; Chaudhury, M. K., Surface Modification of Silicone Elastomer Using Perfluorinated Ether. *Langmuir* **2000**, 16, (3), 1256-1260.
24. Barquins, M.; Shanahan, M. E. R., Effect of surface cavities on static and dynamic adhesion to an elastomer. *International Journal of Adhesion and Adhesives* **1997**, 17, (4), 313-317.
25. Degrandi-Contraires, E.; Beaumont, A.; Restagno, F.; Weil, R.; Poulard, C.; Leger, L., Cassie-Wenzel-like transition in patterned soft elastomer adhesive contacts. *Epl* **2013**, 101, (1).
26. Degrandi-Contraires, E.; Poulard, C.; Restagno, F.; Leger, L., Sliding friction at soft micropatterned elastomer interfaces. *Faraday Discussions* **2012**, 156, 255-265.
27. Poulard, C.; Restagno, F.; Weil, R.; Leger, L., Mechanical tuning of adhesion through micro-patterning of elastic surfaces. *Soft Matter* **2011**, 7, (6), 2543-2551.

28. Shanahan, M. E. R.; Michel, F., Physical adhesion of rubber to glass: cross-link density effects near equilibrium. *International Journal of Adhesion and Adhesives* **1991**, 11, (3), 170-176.
29. Nase, J.; Lindner, A.; Creton, C., Pattern formation during deformation of a confined viscoelastic layer: From a viscous liquid to a soft elastic solid. *Physical Review Letters* **2008**, 101, (7).
30. Chaudhury, M. K.; Whitesides, G. M., Direct measurement of interfacial interactions between semispherical lenses and flat sheets of poly(dimethylsiloxane) and their chemical derivatives. *Langmuir* **1991**, 7, (5), 1013-1025.
31. Ren, X.; Bachman, M.; Sims, C.; Li, G. P.; Allbritton, N., Electroosmotic properties of microfluidic channels composed of poly(dimethylsiloxane). *Journal of Chromatography B: Biomedical Sciences and Applications* **2001**, 762, (2), 117-125.
32. Hillborg, H.; Ankner, J. F.; Gedde, U. W.; Smith, G. D.; Yasuda, H. K.; Wikström, K., Crosslinked polydimethylsiloxane exposed to oxygen plasma studied by neutron reflectometry and other surface specific techniques. *Polymer* **2000**, 41, (18), 6851-6863.
33. Hillborg, H.; Tomczak, N.; Oláh, A.; Schönherr, H.; Vancso, G. J., Nanoscale Hydrophobic Recovery: A Chemical Force Microscopy Study of UV/Ozone-Treated Cross-Linked Poly(dimethylsiloxane). *Langmuir* **2004**, 20, (3), 785-794.
34. Makamba, H.; Hsieh, Y.-Y.; Sung, W.-C.; Chen, S.-H., Stable Permanently Hydrophilic Protein-Resistant Thin-Film Coatings on Poly(dimethylsiloxane) Substrates by Electrostatic Self-Assembly and Chemical Cross-Linking. *Analytical Chemistry* **2005**, 77, (13), 3971-3978.
35. Seo, J.; Lee, L. P., Effects on wettability by surfactant accumulation/depletion in bulk polydimethylsiloxane (PDMS). *Sensors and Actuators B: Chemical* **2006**, 119, (1), 192-198.
36. Wu, Z.; Tong, W.; Jiang, W.; Liu, X.; Wang, Y.; Chen, H., Poly(N-vinylpyrrolidone)-modified poly(dimethylsiloxane) elastomers as anti-biofouling materials. *Colloids and Surfaces B: Biointerfaces* **2012**, 96, 37-43.
37. Yu, K.; Han, Y., A stable PEO-tethered PDMS surface having controllable wetting property by a swelling-deswelling process. *Soft Matter* **2006**, 2, (8), 705-709.
38. Gasteier, P.; Reska, A.; Schulte, P.; Salber, J.; Offenhäusser, A.; Moeller, M.; Groll, J., Surface Grafting of PEO-Based Star-Shaped Molecules for Bioanalytical and Biomedical Applications. *Macromolecular Bioscience* **2007**, 7, (8), 1010-1023.
39. Chen, H.; Brook, M. A.; Sheardown, H. D.; Chen, Y.; Klenkler, B., Generic Bioaffinity Silicone Surfaces. *Bioconjugate Chemistry* **2006**, 17, (1), 21-28.
40. Chen, H.; Brook, M. A.; Sheardown, H., Silicone elastomers for reduced protein adsorption. *Biomaterials* **2004**, 25, (12), 2273-2282.
41. Lee, J. N.; Park, C.; Whitesides, G. M., Solvent Compatibility of Poly(dimethylsiloxane)-Based Microfluidic Devices. *Analytical Chemistry* **2003**, 75, (23), 6544-6554.
42. Efimenko, K.; Crowe, J. A.; Manias, E.; Schwark, D. W.; Fischer, D. A.; Genzer, J., Rapid formation of soft hydrophilic silicone elastomer surfaces. *Polymer* **2005**, 46, (22), 9329-9341.
43. Davis, C. S.; Crosby, A. J., Mechanics of wrinkled surface adhesion. *Soft Matter* **2011**, 7, (11), 5373-5381.
44. White, C. C.; VanLandingham, M. R.; Drzal, P. L.; Chang, N. K.; Chang, S. H., Viscoelastic characterization of polymers using instrumented indentation. II. Dynamic testing*. *Journal of Polymer Science Part B: Polymer Physics* **2005**, 43, (14), 1812-1824.
45. Kim, P.; Kim, D. H.; Kim, B.; Choi, S. K.; Lee, S. H.; Khademhosseini, A.; Langer, R.; Suh, K. Y., Fabrication of nanostructures of polyethylene glycol for applications to protein adsorption and cell adhesion. *Nanotechnology* **2005**, 16, (10), 2420.
46. Eddington, D. T.; Puccinelli, J. P.; Beebe, D. J., Thermal aging and reduced hydrophobic recovery of polydimethylsiloxane. *Sensors and Actuators B: Chemical* **2006**, 114, (1), 170-172.
47. Carré, A.; Shanahan, M. E. R., Effect of Cross-Linking on the Dewetting of an Elastomeric Surface. *Journal of Colloid and Interface Science* **1997**, 191, (1), 141-145.
48. Chen, Y. L.; Helm, C. A.; Israelachvili, J. N., Molecular mechanisms associated with adhesion and contact angle hysteresis of monolayer surfaces. *The Journal of Physical Chemistry* **1991**, 95, (26), 10736-10747.
49. Redon, C.; Brochard-Wyart, F.; Rondelez, F., Dynamics of dewetting. *Physical Review Letters* **1991**, 66, (6), 715-718.
50. Tadmor, R., Line Energy and the Relation between Advancing, Receding, and Young Contact Angles. *Langmuir* **2004**, 20, (18), 7659-7664.
51. Wu, S., Interfacial and Surface Tensions of Polymers. *Journal of Macromolecular Science, Part C* **1974**, 10, (1), 1-73.

52. Verneuil, E.; Ladoux, B. t.; Buguin, A.; Silberzan, P., Adhesion on Microstructured Surfaces. *The Journal of Adhesion* **2007**, 83, (5), 449-472.
53. Chen, Y.-C.; Crosby, A. J., High Aspect Ratio Wrinkles via Substrate Prestretch. *Advanced Materials* **2014**, 26, (32), 5626-5631.
54. Imburgia, M. J.; Crosby, A. J., Rolling wrinkles on elastic substrates. *Extreme Mechanics Letters* **2016**, 6, 23-30.

Chapter 5: Conclusion and Research proposal

In the previous chapters, we described a first attempt of a comprehensive study concerning the nature of interfacial instabilities in nanolayer coextrusion. We also presented some potentialities of this processing tool for the design of nanostructured materials with enhanced properties (mainly mechanical, but work on barrier properties has also been conducted and not presented in this manuscript). Means to control patterning through interfacial tension and to tune surface chemistry of elastomers without affecting their viscoelastic properties were described.

In this final chapter ongoing and future studies will be briefly presented, mostly focused on pursuing the work presented in chapter 2. I will not describe more applied projects here (the reader can refer to the end of chapter 3 for a brief introduction on some of these). The goal of what will be presented in the following is to develop model experiments to gain a better understanding on the physical phenomena responsible for instabilities and breakups in nanolayer coextrusion, but also, more generally to gain insight on the physics of confined polymer melts, especially when submitted to flow, through these model experiments or through the use of well-designed nanolayered films.

5.1. Ongoing studies and preliminary results

5.1.1. Nanolayer coextrusion

It has been pointed out in chapter 2 that, according to our hypothesis concerning layer breakup, all amorphous polymer pairs should lead to similar critical thicknesses, due to comparable values of both interfacial tensions and Hamaker constants in every such system. However, troubling results obtained by Baer on PC/PMMA compared to what we obtained for PS/PMMA have also been discussed previously (see chapter 2). In consequence, we started to investigate this polymer pair in more details.

PMMA 825T (Altuglas) and PC 121 R (Sabic) were chosen for this study. Their chemical structure is presented in figure 1. Their weight average molar mass and dispersities are 140000 and 43000 g/mol and 1.9 and 2.4 respectively. Their T_g s are 116 and 146 °C respectively, and the viscosity ratio η_{PC} / η_{PMMA} lies in the range 0.95-1.2 for shear rates between 1 and 10 s⁻¹. The extrusion temperature is set at 240 °C, the number of LME has been varied from 10 to 12, and the temperature of the chill roll was set at 95 °C in case PMMA was the outer layer and 130 °C in case PC was the outer layer.

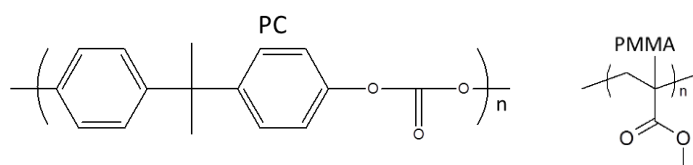


Figure 1: chemical structures of PC (bisphenol A) and PMMA

In this first study, two proportions were chosen for the PC/PMMA films: 90/10 and 10/90 wt%. The analysis procedure detailed previously was applied.

On the small amount of films studied and following the same approach as in chapter 2, master curves of the experimental thickness and amount of broken layers as a function of the nominal thickness were obtained and are shown in figure 2.

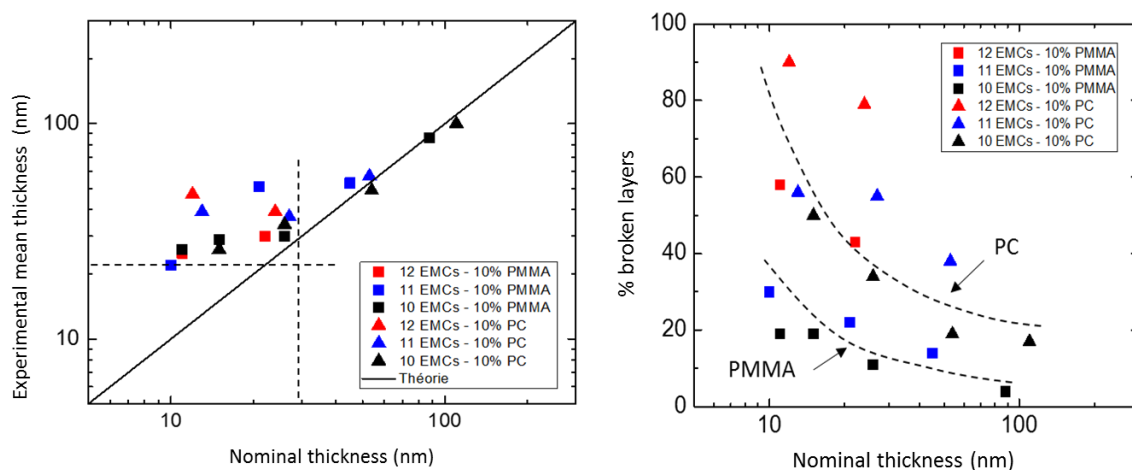


Figure 2: experimental mean thickness (left) and percentage of broken layers (right) as a function of the nominal thickness for PC/PMMA nanolayered films.

First, it can be seen that for this polymer pair and assuming the film sampling is representative (note that no 50/50 wt% films were studied, for example), the critical thickness appears close to 20 nm. Second, it can be noted that PC and PMMA appears to behave differently as far as layer breakups are concerned (PMMA being more “stable” than PC), which was not observed for PS/PMMA films.

Let us then come back to the AFM observations and compare them to Baer work on this system. As can be seen in figure 3, if contrast is reasonably good on the phase images for relatively thick layers (≥ 50 nm) (left image), it becomes mediocre for thinner layers, especially in the sub-20 nm range. Due to this lack of contrast, the capacity of determining a mean thickness for the layers, and whether these layers are continuous or broken, becomes poor compared to what could be achieved for PS/PMMA. Though this lack of contrast cannot be easily explained, it was also noticed by Baer¹ for similar thicknesses and attributed to the creation of an “interphase material” (the interphase being estimated through solubility parameters at 10 nm for this system). As discussed earlier, this explanation, associated to a higher degree of “compatibility” for PC/PMMA is not entirely convincing when compared to the PS/PMMA system. However, it has been noted that PC/PMMA interphase may be more pronounced due to transesterification reactions between PC and PMMA occurring at high temperatures.¹

In consequence, Baer did not use AFM images to characterize sub-20 nm thicknesses in PC/PMMA blends but indirect permeability measurements extrapolated with a 3-phase model involving the permeability and

thickness values of PC, PMMA and interphase. The obtained results indicate that 12 nm continuous layers can be obtained but that below this value an interphase material is obtained.^{2,3}

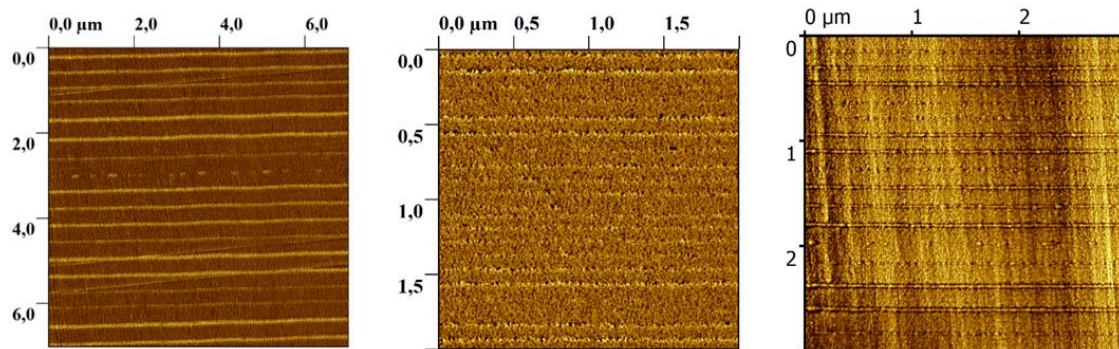


Figure 3: AFM phase images of PC/PMMA nanolayered films, with from left to right PMMA nominal thicknesses of 45 nm and 10 nm and PC nominal thickness of 15 nm.

Thus, many open questions remain concerning PC/PMMA nanolayered films (which will also be discussed below), from their characterization to the determination of an unquestioned critical thickness. Especially, AFM measurements will require an optimization step for PC/PMMA, and may need coupling with another measurement technique for the layer thicknesses (contrary to Baer, we believe direct measurements, such as TEM with selective staining or AFM using viscoelastic mapping mode would be more efficient). It may also become necessary to gain access to physical parameters which are difficult to measure experimentally, such as the interfacial thickness (or size) of the interphase. Small angle neutron scattering experiments shall be considered in order to stop relying on imprecise values extracted from solubility parameters.

Another way to look at the effect of the interfacial tension and of the surface dynamic properties should be through the addition of a diblock copolymer as an inter-layer (via the addition of a third extruder, already available in the lab), depending on the availability of such copolymers in extrudable quantities (i.e., kg). Because of the extensive study that was performed on PS/PMMA films and because of the relative simplicity of the synthesis of a PS-*b*-PMMA diblock copolymer, such experiments will be considered in the near future, in partnership with Arkema to provide the diblocks.

On the short term, we believe an extensive study on PC/PMMA should answer part of these questions and help comforting our van der Waals driven rupture in nanolayers and the impact of a diffuse interface on this model (based on a neat one).

5.1.2. Dewetting experiments

Some questions concerning the “static” dewetting of a thin film within an immiscible polymer matrix are still being investigated.

First, a deeper analysis of the simple model presented for the dewetting is under way. Notably, we are trying to monitor more quantitatively the role of the interfacial tension in the dewetting kinetics. To do that, diblock PS-*b*-PMMA copolymers have been added in the PS thin film. Representative results can be seen in figure 3. A

sharp decrease in the dewetting speed can be observed (around 40% with 10 wt% of diblock) and have been observed for different film thicknesses and at different temperatures. According to the model developed in chapter 2, the influence of the diblock on the thin film viscosity should not play a role in the dewetting kinetics since it is driven by the matrix viscosity. However, the potential effect of diblock at the interface in the matrix viscosity should be studied carefully. Finally, the quantitative relation between block concentration and interfacial tension has not been established yet (measurements of interfacial tensions in blends are, as stated previously, not simple experiments⁴), even though it is reasonable to assume that interfacial tension will in a certain range of concentrations decrease with increasing quantity of block copolymers.⁵ A robust experimental set-up to measure interfacial tension of polymer blends in the molten state is currently developed in the lab.

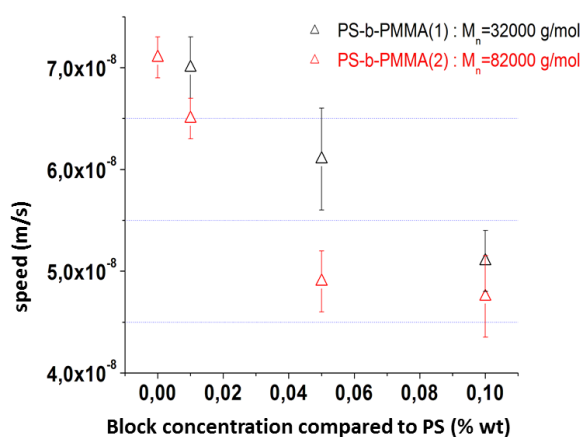


Figure 3: average dewetting speed as a function of the amount of block copolymer in a 120 nm PS film.

Until now, no clear trend has been observed on the effect of the block the nucleation time, i.e. the typical time at which holes appear in the film and start to grow (see figure 4), which suggests the nucleation mechanism is not impacted by the presence of diblock.

Coming back to these experiments, it may be possible that the block copolymers used have too high molar masses, leading to “stable” micellization within the film instead of diffusion to the interface. A third block copolymer, having molar masses below the molar masses between entanglements for each block shall be tested. Another option would be to add the block in the PMMA thick layers and anneal them for a long time to cover the surface with PS chains with no risks of dewetting (though a great quantity of block would be needed).

Another related ongoing work on this dewetting experiment is the characterization the initial rupture stage, spinodal and/or nucleation as a function of the film thickness. Notably, we would like to see if, in this trilayer configuration, we can switch from one mechanism to another as in a “classical” bilayer system.^{6, 7} If spinodal dewetting can be observed for thinner films (typically below 50 nm), it is then reasonable to study whether the initial nucleation time is strongly modified, and if the dewetting kinetics is influenced by the initial mechanism (contrary to what is predicted and observed in a bilayer system^{8, 9}).

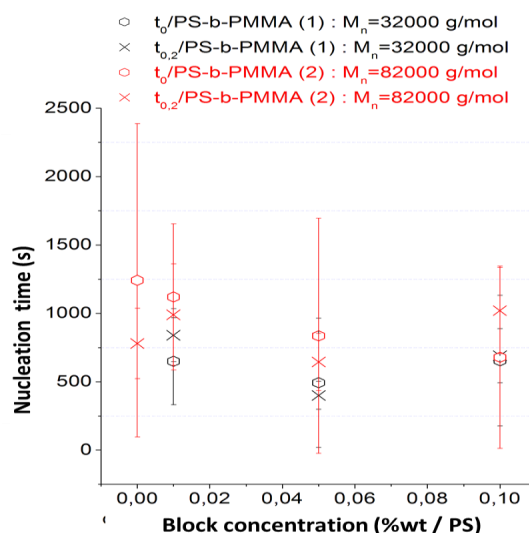


Figure 4: average nucleation time determined by two methods (fitting parameter and direct imaging) as a function of the block concentration within the thin PS film (260 nm) at 180 °C

The last strong topic of current investigation is the development of an experimental set-up that will allow taking into account the role of shear forces in the dewetting of thin films. In a first approach, we tried to use a commercial optical shearing stage (Linkam) which can heat and shear a sample while observing it under a microscope. The setup is not perfectly well-suited to this complicated and never conducted (to the best of our knowledge) experiment. Contrast is poor under shear, and makes it complicated to follow the growth of a moving hole.

Nucleation time		
	Static mode	Dynamic mode
180 °C	5-6 min	7-8 min
200 °C	< 30 secs	40 secs

Table 1: typical nucleation time for dewetting of a PS thin film (260 nm) embedded in a PMMA matrix at 180 °C and 200 °C in static and dynamic mode. Nucleation time was here determined through direct imaging.

This stabilizing effect of shear against rupture or dewetting has already been discussed theoretically^{10, 11} but further experiments with a more appropriately designed set-up need to be conducted to confirm these results. This will be discussed in the next section.

Nonetheless, a few preliminary results were obtained at low shear rates (0.03 s^{-1}) (figure 5 and table 1). Figure 5 compares the dewetting kinetics of similar PS thin films within a PMMA matrix in static and dynamic modes. It appears that holes grow faster when sheared than in static conditions. However, table 1 seems to indicate that shearing may increase the nucleation time or in other words stabilize the films against dewetting and apparition of holes.

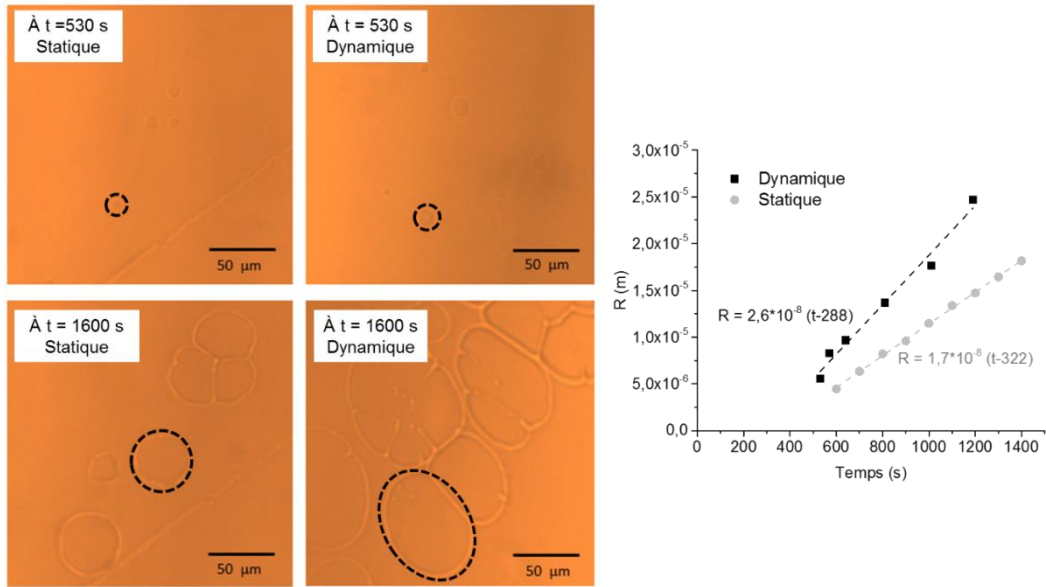


Figure 5: Dewetting kinetics of a 260 nm PS film embedded in a PMMA matrix at 180 °C in static and dynamic (0.03 s^{-1}) mode

5.1.3. Decoupling the effects of shear and elongation forces on the rupture of thin films

During nanolayer coextrusion, shear and elongation forces are applied to the melt flows. From a simplified point of view, shear forces are mainly applied when the melt is passing through the LME and in the flat die, while elongation forces are applied at the exit of the flat die and in the chill rolls. Note that drawing occurring in the chill rolls happens simultaneously with anisothermal cooling of the melt.

In chapter 2, we did not discuss possible differences in the instabilities origins during the process. However, it seemed that ruptures occurred below targeted thicknesses of $\sim 30 \text{ nm}$ whatever the processing route chosen (low concentration, high number of LME or high Dr) (see figure 3 in chapter 2).

To gain further insight on this question, and study more specifically the effects of the chill roll step on the thinning of the nanolayers, we adapted in collaboration with F. Restagno and L. Léger a lab-built “fast stretcher” they developed to study the in-situ formation of block copolymers at polypropylene (PP) – polyamide (PA) interfaces during coextrusion.¹² This setup was used to heat above T_g and subsequently draw at a chosen elongation a coextruded film initially prepared at $Dr = 1$. Draw ratios up to 60 were tested with the fast stretcher. First results comparing nanolayered films obtained directly via coextrusion with nanolayered unstretched films drawn afterwards via the fast stretcher tend to confirm the previous observations (see figure 6): a critical thickness around 15 nm is reached whatever the processing conditions chosen. Below targeted thicknesses of 20 nm, the mean experimental thickness deviates from the nominal one along with an increase in the percentage of broken layers. Still, it appears that drawing may be less “brutal” than shearing to achieve thicknesses close to the critical one. This needs to be confirmed by further studies using this fast stretcher.

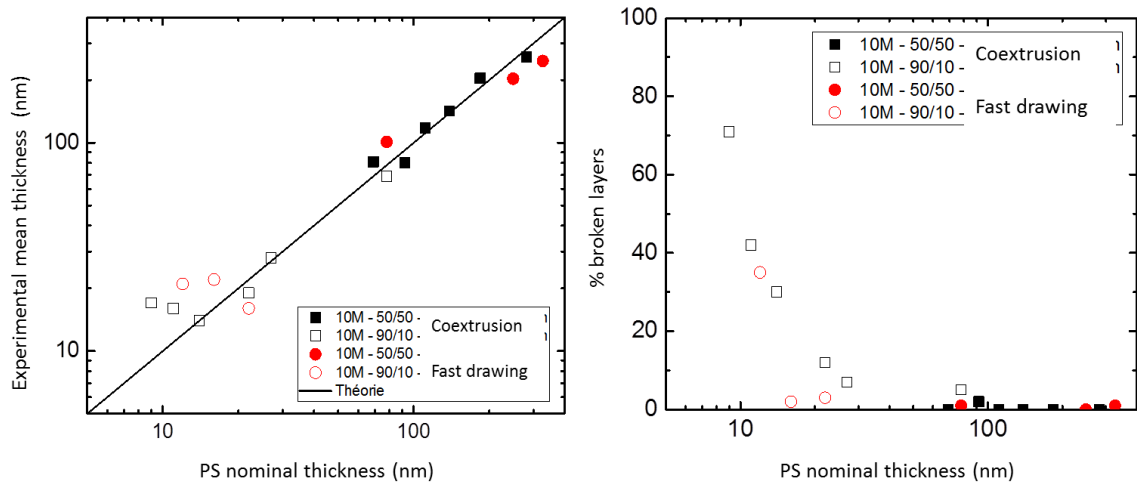


Figure 6: experimental mean thickness (left) and percentage of broken layers (right) as a function of the nominal thickness for coextruded films (in black) and post-stretched films (in red).

5.2. Research project

Building on ongoing new experiments described in the previous section and on results described in chapters 2 and 3, I will conclude by briefly describing the main project I intend on working on over the next few years.

The aim of a PhD work (grant from the Ministry of Research, “contrat doctoral”) that should begin in September 2017 and which will be co-supervised with Cyrille Sollogoub will consist in designing a rheo-optic experimental set-up in collaboration with F. Restagno (LPS lab, Paris-Saclay University) adapted to the observation of dewetting in shear-controlled conditions. A prototype is now almost finished and will be tested as soon as possible. The experimental goal is to achieve better contrast and sync between image acquisition and growing holes moving due to shear than with the Linkam apparatus. Then we will study the effect of shear flow on the kinetics of dewetting of ultra-thin polymer flows from an experimental viewpoint, which has, as already pointed out, never been studied until now. The effect of the layer thickness, shear intensity, interfacial tension (through similar diblock experiments conducted in static mode) and long-range forces on the kinetics of dewetting and on the initial mechanism for rupture (either spinodal or nucleation) will be quantified.

This experimental study will be coupled with a theoretical approach on hydrodynamics of ultra-thin viscous films in collaboration with T. Salez (Gulliver lab, ESPCI). This theoretical approach will allow understanding the flow induced effect on the thermal fluctuations amplitude, on the kinetics of instabilities growth and on the stability of thin layers in nanolayer coextrusion. This model will take into account the effects of shear and elongational stresses specific to the coextrusion and model geometries, as well as thermal fluctuations, and will allow reproducing and analyzing the destabilization kinetics of multilayer structures due to disjoining forces. More precisely, in the lubrication approximation valid for thin films, a so-called “thin-film equation” describing the profile evolution in time will be derived from the Stokes and continuity equations. Moreover, a steady flow (including external stresses), a stabilizing Laplace-pressure term and a destabilizing disjoining-pressure term will be added to the model. Finally, to trigger thermally-driven destabilization processes, a white noise may be added to the governing thin-film equation, thus making it a stochastic partial differential equation. Therefore, from a thermally-induced surface perturbation, one could study the competition between flow-induced or

capillary stabilizations and disjoining destabilization, and by this mean model the dynamics of the rupture mechanism.

Another tentative project is also to study more closely the roles of interface and interphase on the changes of polymer properties under confinement. Since nanolayer coextrusion produces “macroscopic” samples with multiplied confined phases and interfaces, such samples can then be studied with classical characterization tools that are difficult to use when dealing with, for example, spin-coated nanofilms.

In particular, the effects and mechanisms of the confinement (and of the interfaces) on the T_g of amorphous polymers have been the subject of many controversies.^{13, 14} Briefly, PS films have shown significant T_g -depletion for thicknesses below 50 nm when supported on a silicon substrate, independently on parameters such as molecular weight or details of the spin-coating procedure, and on the measurement technique (ellipsometry, X-ray reflectivity, dielectric techniques¹⁵).¹³ However, the role of the substrate in these observations has been pointed out, by using substrates with different interactions^{16, 17} or by studying free-standing films.¹⁸ The role of the chemical nature of the polymer has also been questioned.¹⁹ A recent study tends to confirm a free-surface intrinsic effect (over other possible explanations) to explain the T_g -reduction.²⁰ In a series of recent studies, both the effects of the nature and the thickness of a confining polymeric medium have been investigated recently on model “multilayers” (≤ 5 layers) by Torkelson via relatively complicated tracking of the temperature dependence of fluorescence dyes incorporated to thin spin-coated films or self-assembled diblocks.²¹ These studies reopened the debate on the role of the substrate interactions by in this case, looking at what happens when an interphase (between the film and the immiscible polymer substrate or capping layer) exists.²² The nature and size of the interphase appears to influence the chain dynamics for layers having similar thicknesses.²² The chain density in the interphase may also be an important parameter.²³

Such effects may be easier to characterize with multilayer coextruded films. Some studies concerning T_g in nanolayered films have been conducted. The PC/PMMA “interphase material”¹ displayed a shift in the T_g s of PC and PMMA below nominal thicknesses on the order of 100 nm, leading to a single T_g around 120 °C for nominal thicknesses below 12 nm. However, this result does not seem to be confirmed by further studies on similar films, which reported only very small shifts of T_g for layers down to 12 nm.^{24, 25} If more work is needed to understand these seemingly contradictory results (very preliminary results in our group on PS/PMMA films did not show any noticeable shift in T_g as measured by DMTA, but may indicate a shift for the PS layers by ellipsometry), these studies indicate that segmental dynamics or fragilities may be easier to obtain on such nanolayered films through “conventional” techniques for macroscopic samples (modulated DSC and/or dielectric measurements) than on spin-coated thin films^{26, 27} and so may enrich the still existing debates on the physics of thin glassy films.

Concerning nanolayer coextrusion, once the mechanisms responsible for breakups in amorphous polymer pairs are more clearly identified through the PC/PMMA study, it will be interesting to take into account possible extra-effects due to crystallization. As suggested by table 1 in chapter 2, and by some of the work conducted in our group^{28, 29} it appears harder to achieve nanometric thicknesses when semi-crystalline polymers are considered than for amorphous polymers. Whether it is due to stronger interactions (hydrogen bonds for example in the case of polyamide) favoring rupture or to crystallization of the semi-crystalline polymers

remains an open question. Crystallization kinetics, volume changes and confinement effects may play a role in the critical thickness one can expect from polymer pairs involving at least one semi-crystalline polymer. A more quantitative and fundamental study on such systems shall be of interest (as of now, semi-crystalline polymers were only used in our more “applied” research projects). These effects may be studied using various polyamides (amorphous ones, or with low crystallization kinetics) existing in Arkema’s catalogue.

This ambitious work program has been submitted to the French National Agency of Research (ANR) during the generic call for funding of 2017. If funded, this work would be done in collaboration with Gulliver (J. D. McGraw, T. Salez, E. Raphaël), LPS (F. Restagno, L. Léger) and Arkema.

To conclude, future work will focus on three connected axes:

- comfort and expand our results on the existence and nature of a critical thickness in nanolayered films through the study of other well-chosen polymer pairs.
- develop model experiments to gain insight in the nature of the instabilities in nanolayers submitted to shear or elongational flows.
- use the nanolayered films to address fundamental questions concerning polymer dynamics under confinement.

5.3. References

1. Liu, R. Y. F.; Jin, Y.; Hiltner, A.; Baer, E., Probing Nanoscale Polymer Interactions by Forced-Assembly. *Macromolecular Rapid Communications* **2003**, *24*, (16), 943-948.
2. Liu, R. Y. F.; Ranade, A. P.; Wang, H. P.; Bernal-Lara, T. E.; Hiltner, A.; Baer, E., Forced assembly of polymer nanolayers thinner than the interphase. *Macromolecules* **2005**, *38*, (26), 10721-10727.
3. Arabeche, K.; Delbreilh, L.; Adhikari, R.; Michler, G. H.; Hiltner, A.; Baer, E.; Saiter, J.-M., Study of the cooperativity at the glass transition temperature in PC/PMMA multilayered films: Influence of thickness reduction from macro- to nanoscale. *Polymer* **2012**, *53*, (6), 1355-1361.
4. Xing, P.; Bousmina, M.; Rodrigue, D.; Kamal, M. R., Critical Experimental Comparison between Five Techniques for the Determination of Interfacial Tension in Polymer Blends: Model System of Polystyrene/Polyamide-6. *Macromolecules* **2000**, *33*, (21), 8020-8034.
5. Chang, K.; Macosko, C. W.; Morse, D. C., Interfacial Tension Measurement and Micellization in a Polymer Blend with Copolymer Surfactant: A False Critical Micelle Concentration. *Macromolecules* **2015**, *48*, (22), 8154-8168.
6. Seemann, R.; Herminghaus, S.; Jacobs, K., Gaining control of pattern formation of dewetting liquid films. *Journal of Physics: Condensed Matter* **2001**, *13*, (21), 4925.
7. Meredith, J. C.; Smith, A. P.; Karim, A.; Amis, E. J., Combinatorial Materials Science for Polymer Thin-Film Dewetting. *Macromolecules* **2000**, *33*, (26), 9747-9756.
8. Qu, S.; Clarke, C. J.; Liu, Y.; Rafailovich, M. H.; Sokolov, J.; Phelan, K. C.; Krausch, G., Dewetting dynamics at a polymer-polymer interface. *Macromolecules* **1997**, *30*, (12), 3640-3645.
9. Wyart, F. B.; Martin, P.; Redon, C., Liquid-liquid dewetting. *Langmuir* **1993**, *9*, (12), 3682-3690.
10. Davis, M. J.; Gratton, M. B.; Davis, S. H., Suppressing van der Waals driven rupture through shear. *Journal of Fluid Mechanics* **2010**, *661*, 522-539.
11. Thiébaud, M.; Bickel, T., Nonequilibrium fluctuations of an interface under shear. *Physical Review E* **2010**, *81*, (3), 031602.
12. Barraud, T.; Restagno, F.; Devisme, S.; Creton, C.; Léger, L., Formation of diblock copolymers at PP/PA6 interfaces and their role in local crystalline organization under fast heating and cooling conditions. *Polymer* **2012**, *53*, (22), 5138-5145.
13. Forrest, J. A.; Dalnoki-Veress, K., The glass transition in thin polymer films. *Advances in Colloid and Interface Science* **2001**, *94*, (1-3), 167-196.
14. Alcoutlabi, M.; McKenna, G. B., Effects of confinement on material behaviour at the nanometre size scale. *Journal of Physics-Condensed Matter* **2005**, *17*, (15), R461-R524.
15. Tress, M.; Erber, M.; Mapesa, E. U.; Huth, H.; Müller, J.; Serghei, A.; Schick, C.; Eichhorn, K.-J.; Voit, B.; Kremer, F., Glassy Dynamics and Glass Transition in Nanometric Thin Layers of Polystyrene. *Macromolecules* **2010**, *43*, (23), 9937-9944.
16. Keddie, J. L.; Jones, R. A. L.; Cory, R. A., Interface and surface effects on the glass-transition temperature in thin polymer films. *Faraday Discussions* **1994**, *98*, (0), 219-230.
17. van Zanten, J. H.; Wallace, W. E.; Wu, W.-I., Effect of strongly favorable substrate interactions on the thermal properties of ultrathin polymer films. *Physical Review E* **1996**, *53*, (3), R2053-R2056.
18. Dalnoki-Veress, K.; Forrest, J. A.; Murray, C.; Gigault, C.; Dutcher, J. R., Molecular weight dependence of reductions in the glass transition temperature of thin, freely standing polymer films. *Physical Review E* **2001**, *63*, (3), 10.
19. Ellison, C. J.; Mundra, M. K.; Torkelson, J. M., Impacts of polystyrene molecular weight and modification to the repeat unit structure on the glass transition-nanoconfinement effect and the cooperativity length scale. *Macromolecules* **2005**, *38*, (5), 1767-1778.
20. Baumchen, O.; McGraw, J. D.; Forrest, J. A.; Dalnoki-Veress, K., Reduced Glass Transition Temperatures in Thin Polymer Films: Surface Effect or Artifact? *Physical Review Letters* **2012**, *109*, (5), 5.
21. Roth, C. B.; Torkelson, J. M., Selectively probing the glass transition temperature in multilayer polymer films: Equivalence of block copolymers and multilayer films of different homopolymers. *Macromolecules* **2007**, *40*, (9), 3328-3336.
22. Roth, C. B.; McNerny, K. L.; Jager, W. F.; Torkelson, J. M., Eliminating the enhanced mobility at the free surface of polystyrene: Fluorescence studies of the glass transition temperature in thin bilayer films of immiscible polymers. *Macromolecules* **2007**, *40*, (7), 2568-2574.
23. Hénot, M.; Chennevière, A.; Drockenmüller, E.; Shull, K.; Léger, L.; Restagno, F. d. r., Influence of grafting on the glass transition temperature of PS thin films. *The European Physical Journal E* **2017**, *40*, (1), 11.

24. Arabeche, K.; Delbreilh, L.; Saiter, J. M.; Michler, G. H.; Adhikari, R.; Baer, E., Fragility and molecular mobility in micro-and nano-layered PC/PMMA films. *Polymer* **2012**, 55, (6), 1546-1551.
25. Casalini, R.; Zhu, L.; Baer, E.; Roland, C. M., Segmental dynamics and the correlation length in nanoconfined PMMA. *Polymer* **2016**, 88, 133-136.
26. Evans, C. M.; Deng, H.; Jager, W. F.; Torkelson, J. M., Fragility is a Key Parameter in Determining the Magnitude of Tg-Confinement Effects in Polymer Films. *Macromolecules* **2013**, 46, (15), 6091-6103.
27. Ellison, C. J.; Torkelson, J. M., The distribution of glass-transition temperatures in nanoscopically confined glass formers. *Nature Materials* **2003**, 2, (10), 695-700.
28. Boufarguine, M.; Guinault, A.; Miquelard-Garnier, G.; Sollogoub, C., PLA/PHBV Films with Improved Mechanical and Gas Barrier Properties. *Macromolecular Materials and Engineering* **2013**, 298, (10), 1065-1073.
29. Messin, T.; Follain, N. g.; Guinault, A.; Miquelard-Garnier, G.; Sollogoub, C.; Delpouve, N.; Gaucher, V. r.; Marais, S. p., Confinement effect in PC/MXD6 multilayer films: Impact of the microlayered structure on water and gas barrier properties. *Journal of Membrane Science* **2017**, 525, 135-145.

Guillaume MIQUELARD-GARNIER, PhD

CNAM, Matériaux Industriels Polymères, Accès 35
2 rue Conté, 75003 Paris, France
PIMM, Arts et Métiers ParisTech, 151 boulevard de l'Hôpital
75013 Paris, France
(+33) (0)1 40 27 24 57
(+33) (0)1 71 93 65 72
guillaume.miquelardgarnier@lecnam.net
Date of Birth: 13 May, 1980

Maître de Conférences (Assistant Professor) **« Polymer Science and Engineering »**

Since September 1st, 2010

Formation

- 2004-2007:
PhD from University Paris 6, specialized in Polymer Science, SIMM lab, ESPCI.
Magna cum laude.
PhD thesis: Synthesis and mechanical properties of hydrophobically modified polyelectrolyte hydrogels.
PhD advisors: Dr C. Creton et Prof. D. Hourdet.
costantino.creton@espci.fr dominique.hourdet@espci.fr
PhD jury: C. Creton, D. Hourdet, H. R. Brown, D. Teyssié, T. Baumberger, J.F. Joanny
- 2003-2004:
MSc « Condensed Matter » from University Paris 6. Graduated with honors.
- 2000-2004:
ESPCI graduate (French engineering degree www.espci.fr, www.paristech.org). Specialty: “Physics”

Research

- Polymer-polymer interfaces: from molecular control to new materials.

PIMM lab, joint lab (UMR) ENSAM/CNAM/CNRS, « Polymères & Composites » team

(Director : Prof. G. Régner, gilles.regnier@ensam.eu, <http://pimm.paris.ensam.fr>).

Publications (peer-reviewed):

1. Bironeau A., Salez T., Miquelard-Garnier G.*, Sollogoub C.*, “Existence of a critical layer thickness in PS/PMMA nanolayered films”, submitted to *Macromolecules*, **2017**, *50* (10), 4064–4073. DOI: 10.1021/acs.macromol.7b00176
2. Messin T., Follain N., Guinault A., Miquelard-Garnier G., Sollogoub C., Delpouve N., V. Gaucher, Marais S.*, “Confinement effect in PC/MXD6 multilayer films: Impact of the microlayered structure on water and gas barrier properties”, *Journal of Membrane Science*, **2017**, *525*, 135-145. DOI: 10.1016/j.memsci.2016.10.039
3. Miquelard-Garnier G.*, Roland S., “Beware of the Flory parameter to characterize polymer-polymer interactions: A critical reexamination of the experimental literature”, *European Polymer Journal*, **2016**, *84*, 111-124. DOI: 10.1016/j.eurpolymj.2016.09.009
4. Bironeau A., Dirrenberger J.*, Sollogoub C., Miquelard-Garnier G., Roland S., “Evaluation of morphological representative sample sizes for nanolayered polymer blends”, *Journal of Microscopy*, **2016**, *264* (1), 48–58. DOI: 10.1111/jmi.12415
5. Zhu Y., Bironeau A., Restagno F., Sollogoub C., Miquelard-Garnier G.*, “Kinetics of thin polymer film rupture: model experiments for a better understanding of layer breakups in the multilayer coextrusion process”, *Polymer*, **2016**, *90*, 156-164. DOI: 10.1016/j.polymer.2016.03.005

6. Roland S.*, Miquelard-Garnier G., Gervais M., Guinault A., Sollogoub C.*, "Controlling the order of triblock copolymer via confinement induced by forced self-assembly", *Materials Today Communication*, **2016**, *6*, 37-43. DOI: 10.1016/j.mtcomm.2015.11.003
7. Dirany M., Dies L., Restagno F., Léger L., Poulard C., Miquelard-Garnier G.*, "Chemical modification of PDMS surface without impacting the viscoelasticity: Model systems for a better understanding of elastomer/elastomer adhesion and friction", *Colloids and Surfaces A: Physicochem. Eng. Aspects*, **2015**, *468*, 174-183. DOI : 10.1016/j.colsurfa.2014.12.036
8. Li X., McKenna G.B.*, Miquelard-Garnier G.*, Guinault A., Régnier G., Rozanski A., "Graphene-based Multilayered Poly (methyl methacrylate) Nanocomposites via Forced Assembly Coextrusion", *ANTEC 2014 - Proceedings of the Technical Conference & Exhibition*, **2014**, 609-613. ISBN 978-0-9850112-4-6 [Proceeding]
9. Li X., McKenna G.B.*, Miquelard-Garnier G.*, Guinault A., Sollogoub C., Régnier G., Rozanski A., "Forced assembly by multilayer coextrusion to create oriented graphene reinforced polymer nanocomposites", *Polymer*, **2014**, *55*, 248-257. DOI: 10.1002/mame.201200285
10. Rasselet D., Ruellan A., Guinault A., Miquelard-Garnier G., Sollogoub C., Fayolle B.*, "Oxidative degradation of polylactide (PLA) and its effects on physical and mechanical properties", *European Polymer Journal*, **2014**, *50*, 109-116. DOI: 10.1016/j.eurpolymj.2013.10.011
11. Miquelard-Garnier G.*, Guinault A., Fromonteil D., Delalande S., Sollogoub C.*, "Dispersion of carbon nanotubes in polypropylene via multilayer coextrusion: Influence on the mechanical properties", *Polymer*, **2013**, *54(16)*, 4290-4297. DOI: 10.1002/masy.200751021
12. Boufarguine M., Guinault A., Miquelard-Garnier G.*, Sollogoub C.*, "PLA/PHBV films with improved mechanical and gas barrier properties", *Macromolecular Materials and Engineering*, **2013**, *298 (10)*, 1065-1073. DOI: 10.1002/mame.201200285
13. Guinault A.*, Dutarte G., Boufarguine M., Miquelard-Garnier G., Sollogoub C., "Morphology-crystallinity relationship in PLA-PHBV blends prepared via extrusion", *Key Engineering Materials*, **2013**, *554-557*, 1707-1714. DOI: 10.4028/www.scientific.net/KEM.554-557.1707 [Proceeding]
14. Guinault A.*, Nguyen A.S., Miquelard-Garnier G., Jouannet D., Grandmontagne A., Sollogoub C., "The effect of thermoforming of PLA-PHBV films on the morphology and gas barrier properties", *Key Engineering Materials*, **2012**, *504-506*, 1135-1138. DOI: 10.4028/www.scientific.net/KEM.504-506.1135 [Proceeding]
15. Miquelard-Garnier G., Croll A.B., Davis C.S., Crosby A.J.*, "Contact-line mechanics for pattern control", *Soft Matter*, **2010**, *6*, 5789-5794. DOI: 10.1039/C0SM00165A
16. Miquelard-Garnier G., Zimmerlin J., Sikora C.B., Wadsworth P., Crosby A.J.*, "Polymer microlenses for quantifying cell sheet mechanics", *Soft Matter*, **2010**, *6 (2)*, 398. DOI: 10.1039/B916385A
17. Miquelard-Garnier G., Creton C.*, Hourdet D.*, "Large strain behaviour of nanostructured polyelectrolyte hydrogels", *Polymer*, **2009**, *50 (2)*, 481. DOI: 10.1016/j.polymer.2008.11.045
18. Miquelard-Garnier G., Creton C.*, Hourdet D.*, "Strain induced clustering in polyelectrolyte hydrogels", *Soft Matter*, **2008**, *4*, 1011. DOI: 10.1039/B717460H
19. Miquelard-Garnier G., Creton C.*, Hourdet D.*, "Synthesis and viscoelastic properties of hydrophobically modified hydrogels", *Macromolecular Symposia*, **2007**, *257*, 189. DOI: 10.1002/masy.200751021 [Proceeding]
20. Miquelard-Garnier G., Demoures S., Creton C.*, Hourdet D.*, "Synthesis and rheological behavior of new hydrophobically modified hydrogels with tunable properties", *Macromolecules*, **2006**, *39*, 8128. DOI: 10.1021/ma061361n

* : corresponding author

Patent:

21. Delalande S., Fromonteil D., Guinault A., Miquelard-Garnier G., Sollogoub C., WO2014048755, Process For Producing A Thermoplastic Composite Material Reinforced With Carbon Nanotubes, (priority **09/2012**, publication **03/2014**, **FR2995815 (B1) 11/2016**)

Submitted Articles:

1. Amor A., Okhay N., Guinault A., Miquelard-Garnier G., Sollogoub C., Gervais M.*, submitted to *Express Polymer Letters* (**07/2017**). Under revision.

2. Montana J-S., Roland S., Miquelard-Garnier G., Richaud E.*, submitted to *Polymer Degradation and Stability* (09/2017)
3. Montana J-S., Roland S.*, Richaud E., Miquelard-Garnier G.*, submitted to *Polymer* (09/2017)

Supervision:

Supervision or co-supervision since 2010: 2 post-doctorate associates, 4 ATER (temporary teaching and research associates), 4 PhD students, 5 MSc students, 5 undergraduate students

- 2017-2020: K. Kadri, PhD student ENSAM (50%, co-supervision Dr C. Sollogoub 50%)
- 2017-2020: E. Mofakhami, PhD student ENSAM/MINES ParisTech (40%, co-supervision Prof. B. Fayolle 30%, Prof. L. Laiarinandrasana 30%)
- 2016-2017: Dr M. Chebil, ATER CNAM (co-supervision with the pedagogical team)
- 2015-2016: J. Huang, MSc UPMC (now a PhD student with Prof. E. Richaud, PIMM)
- 2014-2017: J-S. Montana, PhD student at the ENSAM (60%, co-supervision Prof. E. Richaud 40%)
- 2014-2016: Dr A. Amor, ATER at the CNAM (co-supervision pedagogical team) (now a high-school teacher)
- 2014-2015: Y. Zhu, MSc UPMC (now an engineer, CRRC Corporation Limited, China)
- 2013-2016: A. Bironeau, PhD ENSAM (30%, co-supervision Dr C. Sollogoub 40%, Prof. G. Régnier 30%). PhD obtained in December 2016.
- 2013-2014: Dr S. Roland, post-doctorate associate CNAM (co-supervision Dr C. Sollogoub)
- 2013-2014: J. André, MSc UTT (50%, co-supervision Dr A. Guinault 50%) (engineer in the PIMM lab until January 2016)
- 2012-2014: Dr N. Okhay, ATER CNAM (co-supervision pedagogical team) (situation unknown)
- 2012-2014: Dr M. Dirany, post-doctorate associate CNAM (post-doctorate associate, Sherbrooke University until may 2016)
- 2011-2015: X. Li, PhD Texas Tech University/ENSAM (30%, co-supervision Prof. G.B. McKenna 40%, Prof. G. Régnier 30%). PhD obtained in January 2015 (now working as an engineer at Polyglass USA, Mapre)
- 2011-2012: Dr M. Boufarguine, ATER CNAM (co-supervision pedagogical team) (now a high-school teacher)
- 2011-2012: D. Jalocha, M2 MAGIS ENSAM (50%, co-supervision Prof. G. Régnier) (now an engineer at Safran)
- 2010-2011: R. Glénat, MSc CNAM (50%, co-supervision Dr A. Guinault 50%) (current situation unknown)

Collective responsibilities:

- 2017-2020: Thesis committee member, L. Feige, PhD student SIMM lab, thesis supervisor C. Creton
- 2016-2019: Elected member of the PIMM lab board
- 2016-2017: Organizing committee member for [JADH 2017](#)
- 2016-2017: Organizing committee member for the GFP annual conference
- 01/2016: Thesis jury member, S. Vuong (LPS, Université Paris-Saclay, thesis supervisors L. Léger and F. Restagno)
- 2015-2017: Nominated member of the [scientific committee](#), French section of Adhesion (SFA)
- 09/2014-01/2017: Organizer of the lab seminars (2/month)
- 2012-2013: Member of 2 recruitment juries for Assistant Professors in le Cnam

Fundings:

- 2017-2020: ENSAM doctoral fellowship (~100k€) for K. Kadri PhD thesis.
- 2017-2020: CIFRE Renault funding for E. Mofakhami PhD thesis (~200k€)
- 2016-2020: partner of collaborative project ANR Immune. CNAM funding: 100k€.
- 2014-2017: ENSAM doctoral fellowship for J-S. Montana PhD thesis (~100k€)
- 2012-2016: partner of collaborative project ANR WAFPI. CNAM funding: 151k€
- 2012-2013: Chateaubriand fellowship (~30k€) for X. Li PhD
- 2011-2014: collaborative project with PSA (~45k€)

Peer-review and expertise:

- **Editor**, *Materials Today Communications*, [Elsevier](#) (09/15-12/18): responsible for editing articles on polymer science, roughly managing 40 articles a year. Since September 2014, *Materials Today Communications* has been mainly publishing articles primarily rejected by *Polymer*, *European Polymer Journal*, *Polymer Degradation and Stability*, etc that were deemed correct scientifically by peer-review but considered unsuitable for publication in these journals (“sound science”).
- **Expert MESR (French Ministry of Research) Crédit Impôt Recherche** (since 08/15).
- Referee (5-10 articles/year) for *Soft Matter*, *Journal of Materials Chemistry* (since 2010), *Macromolecules*, *EPJ E*, *RSC Advances* (2012), *Materials Chemistry and Physics* (2013), *Industrial & Engineering Chemistry Research* (2014), *Colloids and Surfaces A: Physicochemical and Engineering Aspects*, *New Journal of Chemistry* (2015), *Polymer*, *Materials*, *ACS Applied Materials & Interfaces* (2016).
- **Expert** for **Systema**: private company helping companies solving precise industrial problems (consulting).
- Expert for Languedoc-Roussillon (Chercheur d’Avenir 2013 program).
- Referee for Wiley (project for a book entitled “Nanocomposites based on carbon nanotubes”) (2012).

Main collaborations:

- F. Restagno, L. Léger, C. Poulard (LPS, Paris-Saclay)
- G.B. McKenna (Chemical Engineering, Texas Tech University)
- T. Salez (Gulliver, ESPCI)
- S. Marais, N. Follain (PBS, Rouen University)

Learned Society Fellowships:

- Section Française de l’Adhésion (SFA) (elected member of the Scientific Committee, 2015-2017)
- IUPAC
- Groupe Français des Polymères (GFP)
- Société Chimique de France (SCF)
- Société Française de Physique (SFP)
- Fondation Universitaire de Belgique

Invited International Conferences:

1. **Gordon Research Conference Macromolecular Materials** (Ventura, CA, USA, 01/13): *Invited Discussion Leader*, Biopolymer Mechanics

Invited National Conferences:

2. **Journée Axe Elastopôle sur le Graphène** (06/16), « Nanocomposites obtenus par coextrusion multinanocouches »
3. **Workshop GDR Polynano 3661** (Marne-la-Vallée, MMS lab, 06/15), “Graphene reinforced polymer nanocomposites obtained by nanoscopic multi-nano-layer coextrusion”
4. **Journée Technique CRITT Picardie**, « les nanomatériaux en plasturgie » (Verneuil-en-Halatte, 06/14)
5. **Atelier Prospective du GFP** « Graphène et nanocomposites polymères » (Paris, 04/13) : oral presentation on “graphene nanocomposites via melt blending”

Invited Seminars:

6. **Laboratoire Gulliver, équipe PCT**, ESPCI (Paris, 03/16)
7. **Laboratoire LTDS**, Ecole Centrale de Lyon (Ecully, 03/15)
8. **Chemical Engineering Department**, Texas Tech University (TX, USA, 01/15)
9. **Essilor Centre de Recherche** (Labège, France, 02/10)
10. **Laboratoire Physique de la Matière Condensée et Nanostructures**, Université Lyon Claude Bernard 1 (Lyon, 03/10)
11. **Laboratoire de Physique des Solides**, Université d’Orsay (Orsay, 04/09)
12. **Laboratoire PMMH**, ESPCI, (Paris, 03/09)
13. **Laboratoire MMC**, ESPCI, (Paris, 03/09)
14. **Materials Science and Engineering Department**, K. Shull’s group, Northwestern University (IL, USA, 03/07)

15. **Polymer Science and Engineering Department**, A.J. Crosby's group, University of Massachusetts (MA, USA, 03/07)
16. **Materials Department**, Kramer-Fredrickson-Hawker Lab, UCSB (CA, USA, 03/07)

Oral presentations in International Conferences:

17. **15th European Mechanics of Materials Conference** (Brussels, Belgium, 09/16): "Evaluation of morphologically representative sample sizes for nanolayered polymer blends", A. Bironeau, J. Dirrenberger, C. Sollogoub, G. Miquelard-Garnier, S. Roland.
18. **Macro 2016** (Istanbul, Turkey, 07/16): "Kinetics of thin polymer film rupture: model experiments for a better understanding of layer breakups in the multilayer coextrusion process", G. Miquelard-Garnier, Y. Zhu, J. Huang, A. Bironeau, F. Restagno, C. Sollogoub
19. **PPS 2016** (Lyon, France, 07/16): "Existence of a critical thickness in coextruded multilayer films", A. Bironeau, A. Guinault, G. Régnier, G. Miquelard-Garnier, C. Sollogoub
20. **EUPOC 2016** (Lago di Garda, Italy, 05/16), "Self-assembly of triblock copolymers confined via multilayer coextrusion", J-S. Montana, S. Roland, M. Gervais, C. Sollogoub, E. Richaud, G. Miquelard-Garnier
21. **JIP-JEPO 2015** (Donostia San Sebastian, Spain, 09/15), "Self-assembly of triblock copolymers confined via multilayer coextrusion", J-S. Montana, S. Roland, M. Gervais, C. Sollogoub, E. Richaud, G. Miquelard-Garnier
22. **EPF 2015** (Dresden, Germany, 06/15): "Chemical modification of PDMS surface without impacting the viscoelasticity: model systems for a better understanding of elastomer surface properties", M. Dirany, L. Dies, F. Restagno, L. Léger, C. Poulard, G. Miquelard-Garnier
23. **EPF 2015** (Dresden, Germany, 06/15): "Instabilities in Multilayer Coextrusion", A. Bironeau, G. Régnier, G. Miquelard-Garnier, C. Sollogoub
24. **EPF 2015** (Dresden, Germany, 06/15): "Confinement of Triblock Copolymer Morphology via Forced Assembly Induced by Multilayer Coextrusion", S. Roland, A. Guinault, A. Grandmontagne, M. Gervais, G. Miquelard-Garnier, C. Sollogoub
25. **Eurofillers Polymer Blends** (Montpellier, France, 04/15): "Confinement of ABC copolymer morphology via forced assembly induced by multilayer coextrusion", S. Roland, A. Guinault, A. Grandmontagne, M. Gervais, G. Miquelard-Garnier, C. Sollogoub
26. **ANTEC 2014** (Las Vegas, USA, 04/14): "Graphene-based Multilayered Poly(methyl methacrylate) Nanocomposites via Forced Assembly Coextrusion", X. Li, G.B. McKenna, G. Miquelard-Garnier, A. Guinault, G. Régnier, A. Rozanski
27. **16th Annual ESAFORM Conference on Material Forming** (Aveiro, Portugal, 04/13): "Morphology-Crystallinity Relationship in PLA-PHBV Blends Prepared via Extrusion", A. Guinault, G. Dutarte, M. Boufarguine, G. Miquelard-Garnier, C. Sollogoub
28. **15th Annual ESAFORM Conference on Material Forming** (Erlangen, Germany, 03/12): "The Effect of Thermoforming of PLA-PHBV Films on the Morphology and Gas Barrier Properties", A. Guinault, A.S. Nguyen, G. Miquelard-Garnier, D. Jouannet, A. Grandmontagne, C. Sollogoub
29. **11th European Symposium on Polymer Blends** (Donostia-San Sebastian, Spain, 03/12): "The effect of microstructure on gas barrier and mechanical properties in PLA-PHBV films", M. Boufarguine, A.S. Nguyen, A. Guinault, G. Miquelard-Garnier, C. Sollogoub
30. **WCARP IV 2010** (Arcachon, France, 09/10) "Adhesion Induced Wrinkles", G. Miquelard-Garnier, A.B. Croll, A.J. Crosby
31. **APS March Meeting 2010** (Portland, OR, USA, 03/10): "Self-wrinkling of a thin polymer film on a soft elastic substrate", G. Miquelard-Garnier, A.B. Croll, A.J. Crosby
32. **APS March Meeting 2007** (Denver, CO, USA, 03/07): "Structure and mechanical properties of hydrophobically modified hydrogels", G. Miquelard-Garnier, C. Creton, D. Hourdet

Oral presentations in National Conferences:

33. **JADH 2017** (Sainte-Maxime, 10/17) : « Instabilités interfaciales de systèmes polymères nanocouches », G. Miquelard-Garnier, C. Sollogoub, A. Bironeau, Y. Zhu, M. Chebil, T. Salez, F. Restagno
34. **JADH 2015** (Najac, 10/15) : « Fonctionnalisation de surface de PDMS sans modification de viscoélasticité. Surfaces modèles pour l'étude de l'adhésion » M. Dirany, L. Dies, L. Léger, F. Restagno, C. Poulard, G. Miquelard-Garnier

35. **Matériaux 2014** (Montpellier, 11/14) : « Les mélanges PLA-PHBV : effet de la morphologie et de la compatibilisation sur leurs propriétés », N. Okhay, A. Guinault, M. Gervais, G. Miquelard-Garnier, C. Sollogoub
36. **43^{ème} Colloque du GFP** (Saint-Malo, 11/14) : « Nanocomposites polymères préparés par extrusion multianocouches », G. Miquelard-Garnier, A. Guinault, C. Sollogoub
37. **42^{ème} Journée d'études des polymères JEPO** (Obernai, 10/14) : « Étude des instabilités dans le procédé de coextrusion multianocouches », A. Bironeau, G. Régnier, G. Miquelard-Garnier, C. Sollogoub
38. **41^{ème} Colloque du GFP** (Grenoble, 11/12) : « Films à base de mélange PLA/PHBV à propriétés barrières et mécaniques améliorées », M. Boufarguine, A. Guinault, G. Miquelard-Garnier, C. Sollogoub
39. **37^{ème} Colloque du GFP** (Lyon, 11/08) : « Polymères nanofonctionnalisés comme substrats pour étudier la mécanique intercellulaire », G. Miquelard-Garnier, J. Zimmerlin, A.J. Crosby, P. Wadsworth

Poster in International Conferences:

40. **3^d Functional Polymer Materials Conference** (Rome, Italie, 07/17): "Self-Assembly of Triblock Copolymers Confined Via Nanolayer Coextrusion", J-S. Montana, S. Roland, E. Richaud, G. Miquelard-Garnier (awarded the best *Molecular Engineering and Design* Poster Prize of the Royal Society of Chemistry)
41. **ECNP 2016** (Rome, Italy, 09/16): "Impact Of The Multilayer Morphology Of A PC/MXD6 Assembly On Barrier Performances", T. Messin, N. Follain, A. Guinault, G. Miquelard-Garnier, C. Sollogoub, S. Marais
42. **Trilateral Symposium Architected biomaterials, Medical and Tissue Engineering** (Berlin, Germany, 11/14): "From nano- to macroscale applications: multiple processing routes for architected materials", J. Dirrenberger, C. Sollogoub, G. Miquelard-Garnier, S. Roland, A. Guinault, P. Peyre, O. Castelneau, T. Gu, G. Régnier
43. **4th International Conference on Biodegradable and Biobased Polymers** (Rome, Italy, 10/13): "PHBV as a functional component for improving ductility of PLA", M. Boufarguine, A. Ruellan, S. Domenek, V. Ducruet, A. Guinault, G. Miquelard-Garnier, C. Sollogoub
44. **EPF 2013** (Pisa, Italy, 06/13): "Dispersion of carbon nanotubes in polypropylene via multilayer coextrusion: influence on the mechanical properties", G. Miquelard-Garnier, A. Guinault, C. Sollogoub, S. Delalande, D. Fromonteil
45. **EPF 2013** (Pisa, Italy, 06/13): "Mechanical and gas barrier properties of PLA/PHBV films", M. Boufarguine, A. Guinault, G. Miquelard-Garnier, C. Sollogoub
46. **World Polymer Congress, 41st International Symposium on Macromolecules** (Rio de Janeiro, Brasil, 07/06): "Synthesis and rheological behaviour of new hydrophobically modified hydrogels", G. Miquelard-Garnier, C. Creton, D. Hourdet

Poster in National Conferences:

47. **42^{ème} Colloque du GFP** (Roubaix, 11/13) : « Microstructure of PLA/PHBV blends: role of the interfacial tension », N. Okhay, M. Boufarguine, A. Guinault, M. Gervais, G. Miquelard-Garnier, C. Sollogoub
48. **37^{ème} Colloque du GFP** (Lyon, 11/08) : « Effets non-linéaires aux grandes déformations induits par nanostructuration dans des hydrogels polyélectrolytes », G. Miquelard-Garnier, C. Creton, D. Hourdet

Non peer-reviewed publications:

- Guinault A., Miquelard-Garnier G., Grandmontagne A., Sollogoub C., *Revue IAA dossier emballage et conditionnement*, **2013**
- Croll A.B., Miquelard-Garnier G., Davis C.S., Crosby A.J., *Proceedings from the 33rd Adhesion Society's Annual Meeting*, **2010**
- Miquelard-Garnier G., Croll A.B., Crosby A.J., *Bulletin of the American Physical Society* 55 (APS March Meeting), **2010**
- Crosby A.J., Zimmerlin J., Miquelard-Garnier G., Wadsworth P., *Proceedings from the 32nd Adhesion Society's Annual Meeting*, **2009**

- Miquelard-Garnier G., Creton C., Hourdet D., *Bulletin of the American Physical Society* 53 (APS March Meeting), **2008**
- Miquelard-Garnier G., Creton C., Houdet D., *Proceedings of the 41st International Symposium on Macromolecules*, **2006**

Teaching

Member of the CNAM « équipe pédagogique nationale » (national pedagogical team) Materials Science and Mechanical Engineering. Website: <http://materiau.cnam.fr/>

Lectures, tutorials, practical works on Polymer Science and Engineering, for undergraduate and graduate students (BSc, MSc, diplôme d'ingénieurs). 192 hours/year. Mostly continuing education (which is the core activity of the CNAM).

Teaching responsibilities:

- **Co-head of the MSc Matériaux Avancés et Management Industriel.** In charge of the relations with industry (students internships).
- **Creation of a series of practical works for the CNAM “French diplôme d’ingénieurs”, options Chemistry and Materials** (2015-2016). **65k€** obtained to enhance the experimental park.
- **In charge of 2 « stages » Cacemi:** small courses (1 week) for industrials on various topics related to Polymer Science.
- **Jurys:** continuing education (VAE, VES), memoirs diplôme ingénieur CNAM, memoirs MSc Materials Science (CNAM, ENSAM).
- **Mentoring** for CNAM undergraduate and graduate students (DUT, Ecole d’Ingénieurs) (~ 3 students/year).

Outreach

- Invited blogger EducPros.fr, an online media dedicated to higher education. Blog [« un petit monde »](#).
- Co-founder of l’Alambic in 2013, a *think tank* focusing on research, higher education, innovation, and related public policies.
4 op-ed have been published in the French reference newspaper *le Monde* ([l’administration de la recherche publique](#), 02/2013, [enjeux de l’enseignement en ligne](#), 10/2013, [sur l’avenir de la recherche publique en France](#), [sur les débouchés des doctorats](#), 06/2015) and other medias.
Interviewed by [la Tribune](#), [le Monde](#), and other journals.
Invited as an expert at the **Ethical Forum 2014** to discuss on “[Will the universities survive the e-learning revolution? And how?](#)”, Brussels, 11/2014
Creation of a conference cycle for the Master in “Public Administration” of IEP Paris (12*2h). « *Société de la connaissance et innovation : état des lieux et futurs souhaitables* ». (2013-2014).

Formation

- 2004-2007:
PhD from University Paris 6, specialized in Polymer Science, SIMM lab, ESPCI.
Magna cum laude.
PhD thesis: Synthesis and mechanical properties of hydrophobically modified polyelectrolyte hydrogels.
PhD advisors: Dr C. Creton et Prof. D. Hourdet.
costantino.creton@espci.fr dominique.hourdet@espci.fr
PhD jury: C. Creton, D. Hourdet, H. R. Brown, D. Teyssié, T. Baumberger, J.F. Joanny
- 2000-2004:
ESPCI graduate (French engineering degree www.espci.fr, www.paristech.org). MSc « Condensed Matter » from University Paris 6.

Language

- English:

Fluent (I have lived in the USA between 2008 and 2010). 575 (/620) TOEFL in 1996, 925 (/990) TOEIC in 2003.

- German: basic.

Other experiences in teaching and research

- March 2010 - August 2010:

CNRS post-doctorate research fellow. LPS lab, University of Paris-Sud, with Prof. L. Léger leger@lps.u-psud.fr. Collaboration with ESSILOR Int.

- February 2008 - January 2010:

Post-doctorate research fellow. Polymer Science and Engineering department, University of Massachusetts, Prof. A.J. Crosby's group.

(www.pse.umass.edu/acrosby/index.html, crosby@mail.pse.umass.edu).

- 2004-2007 :

Teaching Assistant in Chemistry, University Paris 6 (64h/year).

- 2003- 2004 :

MSc internship in the Physics of Organized Fluids lab (Collège de France), with Prof. Liliane Léger.